Department of Precision and Microsystems Engineering

Controlled formation of 2D DNA origami arrays on hexagonal boron nitride surfaces

Wouter Theodoor Oosterhoff

Report no : 2025.035
Coach : Daria Orekhova
Professor : Sabina Caneva
Specialisation : Dynamics of micro and nano systems
Type of report : Experimental
Date : 15-07-2025

Delft University of Technology

High Tech Engineering thesis

Controlled formation of 2D DNA origami arrays on hexagonal boron nitride surfaces

Authors:
Wouter Oosterhoff (6105661)

Supervisors:
Dr. S. Caneva
D. Orekhova, MSc

In partial fulfillment of the requirements of the decree of

Master of science

in mechanical engineering

To be defended publicly on Tuesday July 15, 2025 at 09:30 AM.

TU Delft Delft University of Technology

Abstract

This research focuses on the utility of using DNA origami nanoactuator arrays. The goal of this research is to control the formation of DNA origami nanoactuator arrays, and their immobilization on hBN. By controlling the formation of DNA origami arrays, large site-specific templates can be produced and used as single-molecule sensing platforms for preliminary cancer diagnostics. By inserting sticky end staples at the edges of the origamis, arrays were realized. Moreover, two fluorescent docking probes for ATTO647N and 12 immobilization 'docking staples' were implemented in the origami design. The docking staples consist of 30 Adenine bases, and were placed on the largest deflection sites of the origamis. The origami with docking staples showed better results on pristine hBN than origamis without. In both cases, an interference layer between origami and hBN was observed, no origamis were immobilized directly on the surface. By creating two different samples, both with different sticky end staples at the edges, large arrays were created. With this method, 7-8 binding sites were utilized per origami interface. When placing them on pristine hBN, no arrays were visible, only a background mesh. When placing single origami structures with docking staples on defective hBN, they appeared stable without an interference layer. Also, when placing the arrays on hBN, they appeared stable and visible, but the length was reduced. By inserting an excess of the full set of edge staples, 17 binding sites were created per origami interface. When placing these arrays on hBN, larger arrays with better visibility were observed, but resulted in a significant reduction in yield per flake. Subsequently, fluorescent measurements were made by using the red channel, the ATTO647N dye attached to the origami could be imaged. By comparing the ATTO647n results to the arrays on hBN, a difference in intensity was detected. This could indicate multiple fluorescent dyes in one spot, and could thus indicate the fluorescent detection of arrays.

Contents

1 Introduction

The development of cancer detection has progressed significantly in recent decades [1]. However, despite the development of diagnostics and techniques, it still remains one of the main causes of death in the 21st century [2]. To be able to treat this disease it is more effective to develop new cancer detection methods that are able to reveal the presence of cancer at the onset, or at an early stage. To enable early detection, scientists now focus on developing sensors for circulating tumor DNA (ctDNA). ctDNAs are the 150-200 base-pair fragments of DNA that are characteristic of the tumor or cancer cell and can be found in the patients bloodstream even at the early stage of the disease [3]. Thus their early detection may contribute to timely treatment and higher chances of recovery. However, the detection of ctDNA is challenging because these molecules are incredibly rare and their concentration ranges between 10 fm and 0.1 am [4]. Current biosensors such as electrochemical, optical, and fiber optical sensors lack the specificity and selectivity for the detection of such molecules [5].

A novel approach to overcome these challenges is the implementation of 2D materials, in particular hexagonal boron nitride (hBN), in combination with DNA origami arrays of nanoactuators for ctDNA detection. hBN is a 2D material that is used for its optical, chemical and mechanical properties [6, 7], it has recently gained a lot of attention in the fields of biophysics and biosensing due to its interesting optical, chemical and mechanical properties [8, 9]. It is transparent and unlike graphene, which has a similar hexagonal structure, it does not quench fluorescence of labeled molecules near the surface [10] and thus it can be used for investigation of single-molecule detection, diffusion, and dynamics [11]. Another interesting property of hBN is the high affinity to single-stranded DNA (ssDNA) due to pi-pi stacking interactions [12], which can be used for designing DNA origami-based nanoactuators sensitive to the strands hybridization with single base specificity.

DNA origami is a highly precise nucleotides assembly technique that relies on the interaction between DNA complementary bases [13]. The implementation of long scaffold strands with shorter staple strands helps to create user-defined 2D or 3D stable structures with known geometry [14]and motion paths which can serve as sensors for the ctDNA. However, one sensor is insufficient for rare molecule detection. The challenge of high throughput can be addressed by making high-density ordered arrays of DNA origami-based biosensors on hBN, were hBN is used to aid the actuation mechanism. There are several approaches to construct DNA biosensor arrays that rely either on the properties of the substrate like ZWM or lithographic patterning or on DNA binding interactions [15, 16]. However, little is known about the assembly of DNA origami on hBN regarding depth and coverage. This research will start with outlining the ways to position and make DNA origami arrays on hBN for sensing purposes. Followed by the experimental results regarding the immobilization of DNA origami arrays on hBN.

2 Theoretical knowledge and state of the art

2.1 DNA and DNA nanotechnology

Before going into more detail about the state of the art, the report first summarizes the relevant theory. The following subjects will be explained to obtain a basic understanding of the topic and research proposal, these are DNA and DNA origami.

2.1.1 DNA

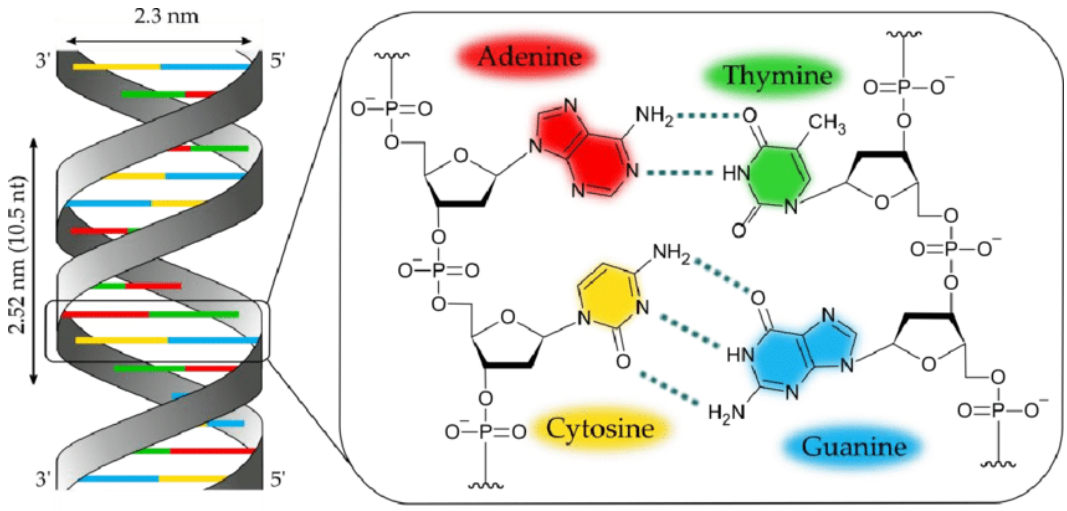

Figure 1: Left: Schematic double helix nature of DNA with labeling of main components. Right: Shows the bonds between different base pairs [17].

DeoxyriboseNucleic Acid(DNA) is a complex molecular structure that can be described as the building block of life and can be found in every cell, both eukaryotic and prokaryotic. DNA is a vital molecule because it encodes everything about a being, from internal physical processes such as metabolism and allergies to external aesthetics like hair color, height or nose structure. The DNA sequences that encode these properties are unique for each person.

Every living organism has DNA which consists of 4 bases, also called nucleotides, namely guanine (G), adenine (A), cytosine (C), and thymine (T). These four bases bind to one other in pairs were T binds preferably with A and C with G. In organisms, these bases in combination with a phosphate backbone form a double helix. The four DNA bases can be further divided into two groups, namely pyrimidines and purines, Guanine and Adenine are purines, and Thymine and Cytosine are pyrimidines. Both groups are nitrogenous bases where purines consist of two carbon-nitrogen rings and pyrimidines have only one carbon-nitrogen ring. The complementary binding between the bases is due to the distinction between these groups and the number of hydrogen bonds that are formed between bases upon bonding. The larger purine bases preferably bind to the smaller pyrimidines, in DNA, Guanine and Cytosine can form three hydrogen bonds whereas Thymine and Adenine can only form two hydrogen bonds. This is known as Watson-crick base pairing [18].

The double helix nature of DNA is schematically shown in Figure 1. Here, on the left, the ends of the phosphate backbone are denoted with 3' and 5', which is often done to denote the part of the deoxyribose sugar group that is open for bonding. On the right, the specific binding between two bases, and the number of bonds between the two pairs is clearly visible. The double helix comes in different forms. Humans have linear DNA, which means it has a clear beginning and end [19], but bacteria have circular DNA and thus do not have a beginning or end. The circular DNA of bacteria is very useful in DNA origami, as will be further discussed in the next paragraph.

2.1.2 DNA origami

DNA origami is a method that can produce nanostructures by folding DNA under specific conditions. In this paragraph, the method of folding DNA origami will be discussed, along with the application of single-molecule switches made of DNA.

2.1.2.1 DNA origami self-assembly

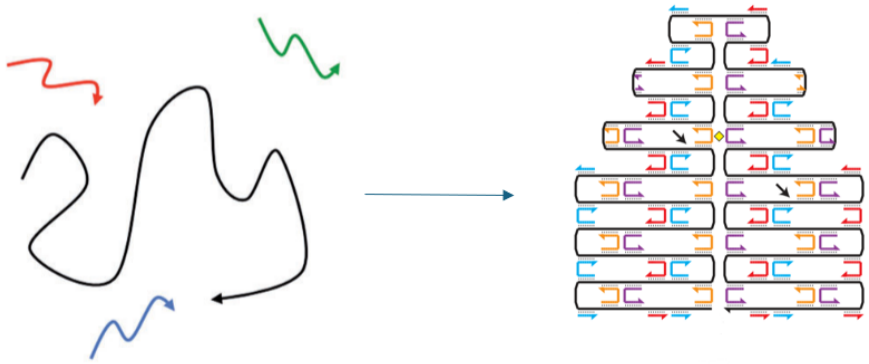

Figure 2: Schematic overview of the combination of scaffold (black) and staple (colored) strands to form a 2D house like structure composed of double helices [13] [14].

In 2006, Rothemund invented a DNA origami assembly technique [13], which, since then, has been widely used across different fields such as drug delivery [8], biosensing [9], and nanoplasmonics [20]. This approach enables the creation of various 2D and 3D [14] DNA-based structures with well-known geometry and controlled dimensions. The DNA origami method uses the Watson-Crick complementary relations of the DNA bases [21]. First, a long circular ssDNA scaffold is commonly extracted from the phage M13MP18 which is 7249 bp long [22]. Due to the size limit if M13MP18, other sources of longer scaffold are documented. [23, 24, 25]. Then short 20-60 nucleotides long staple strands are annealed with the scaffold to create a user-pre-defined dsDNA structure. Figure 23 illustrates the method of folding origamis. Using programs like caDNAno [26], the sequence of the scaffold can be determined such that arbitrary shapes like stars, hexagonal, or circular shapes can be made. Figure 3 shows examples of these arbitrary shapes.

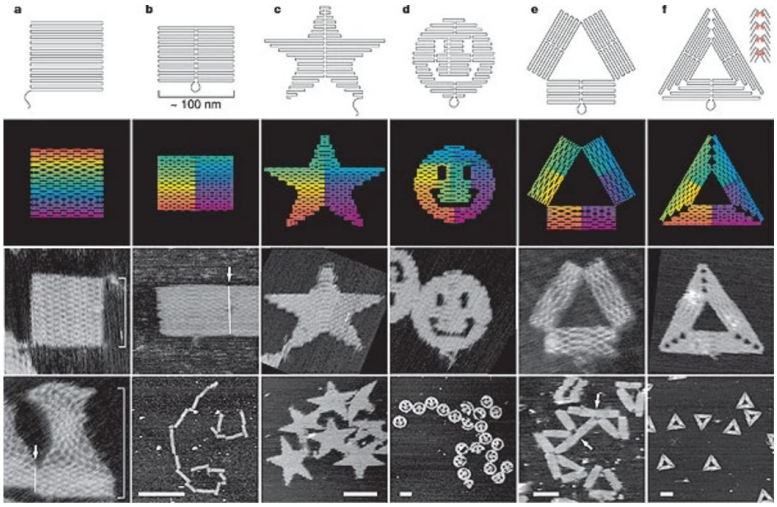

Figure 3: The top two rows of images show the schematic of the origamis, where the bottom two rows show the actual AFM images of the folded origamis [13].

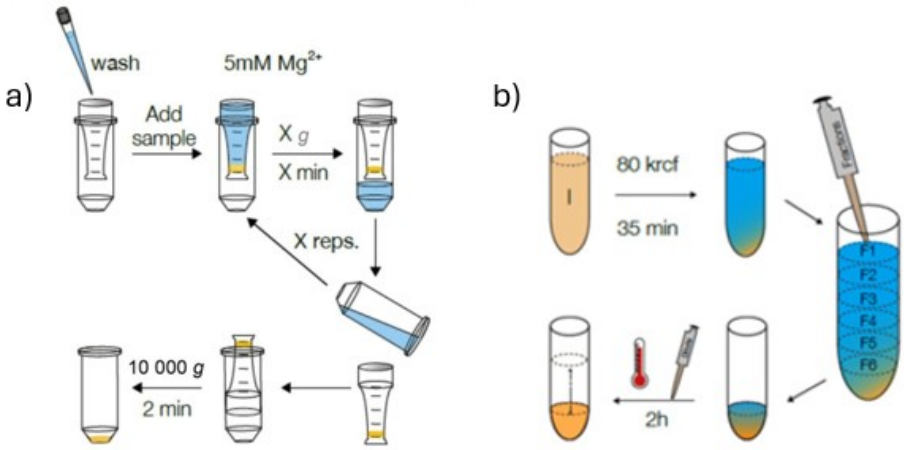

Figure 4: Filtering techniques. a) ultrafiltration. This is a technique where the origami sample is put into a filter and diluted with a buffer containing magnesium. The filter is put into an aliquot and centrifuged for a few minutes, this step is repeated several times. As a last step, the filter is put upside down and centrifuged at a lower speed, after this the sample can be extracted from the aliquot to be further examined. b) ultracentrifugation. This is a technique where the origami sample is put together with a buffer and ultracentrifuged for 35 minutes, after this step a large portion of the origamis is located in the bottom 20 percent of the aliquot.

While the principle of this technique is easy to understand, there are several parameters that need to be taken into account when creating different DNA origami structures. The most important parameters for folding origami are annealing temperature, ion concentration in buffer, and scaffold/staple ratio, as all of these play a crucial role in the folding process. For the production of high-yield origami structures, it is common to use a staple concentration around 10-20 times higher than the scaffold concentration. This is done because the chance that all the staples (this can be in the order of hundreds of different staples) attach to the right place is very low. However, after folding, excess staples still remain in the solution. These excess staples and other unwanted by-products such as misfolded or defective origamis are eliminated by filtering the origami. Gel extraction, ultrafiltration, and ultracentrifugation are commonly used for this purpose [27]. Figure 4 shows the working principle of the latter techniques.

Besides the scaffold and staples, a buffer solution with magnesium cations need to be added to form DNA origami. The magnesium ions are commonly divalent cations (Mg^{2+}) that play an important role in the formation and stability of origami structures [28]. They can form electrostatic bonds and chemical bonds with the DNA. The electrostatic bonds are facilitated by the negative phosphate backbone, and the chemical bonds by hydrogen bonds. When Mg^{2+} binds with DNA, it decreases the electrostatic repulsion that exists between the phosphate backbones of different DNA strands, and thus facilitates DNA-DNA interaction. Besides this, binding of Mg^{2+} with DNA also influences the rigidity of the DNA origami, which can be altered by changing the concentration of Mg^{2+} in the solution [29]. The addition of magnesium ions does not only have a positive influence, when the Mg^{2+} concentration becomes too high, non-specific binding increases and thus lowers the yield of the origamis [30]. Origami structures are often visualized on mica, which is negatively charged and is atomically smooth. In this case, the magnesium ions are very important as they act as salt bridges between the mica sheet and the negatively charged phosphate backbone of DNA to facilitate immobilization [31].

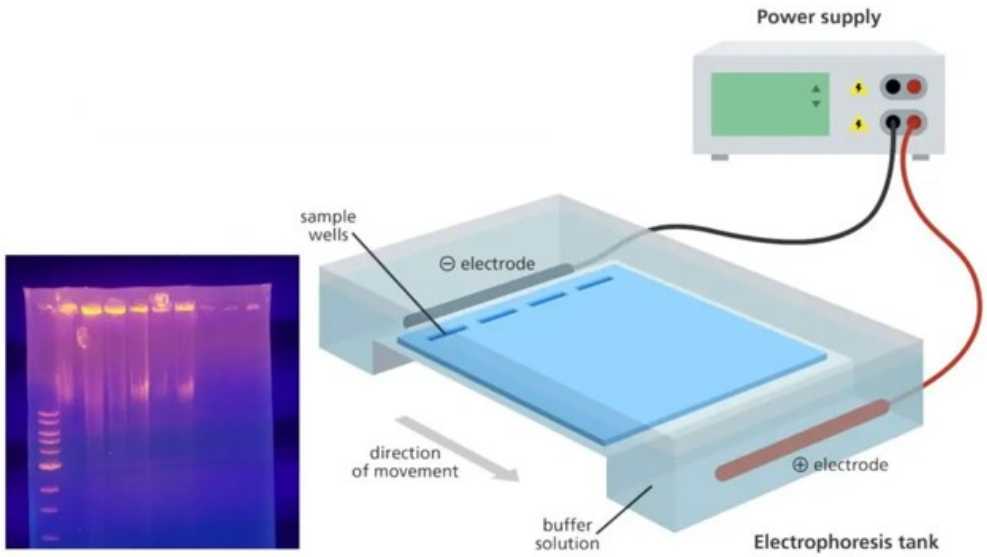

Figure 5: Schematic of the AGE method. Right: Setup with the agarose gel and the wells for the samples. Left: Typical result from such as measurement, where the first well has the molecular ladder sample containing the DNA fragments of the known sizes. Other sample sizes can be determined accordingly.

After the scaffold and staples are combined with the buffer and the right concentration of magnesium ions, they need to be annealed, which is done in a thermal cycler. This machine heats up the sample to a specific temperature and then cools it down at a specific rate, which is crucial for forming origamis. The sample has to be heated in order to break all bonds that exist between DNA strands. After this stage, the slow cooling rate enables the strands to hybridize. The height of the annealing temperature and the cooling rate are dependent on the dimensions (2D, 3D) and the complexity of the origami structures. When the origami structures are annealed and filtered, there is no guarantee that the folding procedure succeeded, so the structure needs to be checked. This can be done by using an atomic force microscope (AFM), or transmission electron microscope (TEM). These methods take a lot of time, and searching for structures without knowing if they are present can be tedious. The simplest way to check if the origamis are folded is by using agarose gel electrophoresis (AGE) [27]. This method uses electrophoresis to push samples through an agarose gel with a set voltage and time. By looking at the distance the samples traveled through the gel compared to the scaffold sample, the degree of folding can be estimated. Figure 5 shows the AGE setup and an example of an AGE result.

The DNA origami method, as has been described above, can be used for multiple purposes and across different fields, because of its nanometer precision, high yield, and programmability. Sensors with dimensions of only tens of nanometers in width can be made [32]. The origami technique however also has disadvantages, the scaffold that is used to form the structure has a limited length, and with this, the size of the structures that can be made is limited to about 100 nm [7]. There are methods to achieve longer scaffolds, but these methods are complicated. Additionally, long scaffolds have a lower yield and due to their length, the chances of non-specific binding are higher. Under environmental changes such as changes in pH, temperature, or ion concentration, origami structures can become unstable. This phenomenon can deliberately be used to generate sensors. In the next paragraph, the topic of origami actuators will be discussed further.

2.1.2.2 DNA origami actuators

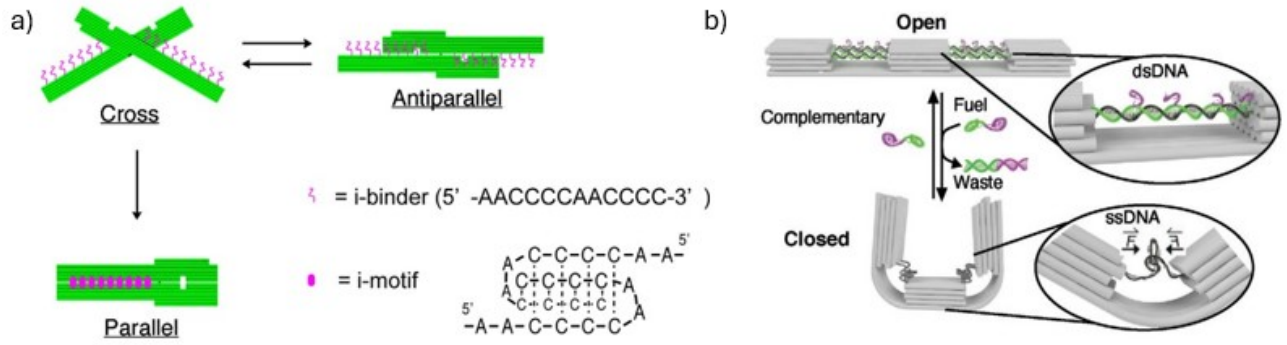

Figure 6: a) Schematic view of the three stages of the pH sensitive actuator, b) Schematic view of the open and closed states of a DNA origami hinge.

DNA origami structures can be used as actuators. These actuators can be programmed to alter their shape or give a signal upon binding with a specific molecule. Moreover, they can react to changes in their environment such as pH, ion concentration or temperature [33]. An example of a switch that reacts to environmental changes is introduced by Kuzuya et al. They made an origami structure that changes its shape under different acidic environments [34]. It is composed of two rectangular antiparallel structures that form an X-structure under standard acidic origami environments, (pH=8.2). When the environmental pH drops to 5.6, the origami structure changes its shape to a rectangle where both of the pieces are placed on top of each other. The change in shape happens because the extended staple strands on both rectangular parts undergo an unusual $C - C^+$ bond when the environment becomes more acidic and forms an i-motif. This goes against the usual base pair preference because now Cytosine binds with Cytosine instead of Guanine. Figure 6a shows the origami actuator and the binding principle. The change in shape after the acidic environment change was imaged using AFM and almost 87 % of the structures changed their shape to a parallel formation.

Origami actuators can also be triggered by adding ssDNA molecules into the solution. Gür et al. made such an actuator by using the different spring constants of ss- and dsDNA [35]. They made a 170 nm long structure with 2 evenly spaced gaps in between, the space between the gaps was filled by inserting two 22 bases long double-stranded staples with a short 5 nt extension. To be able to change the shape of the structure, an excess of complementary staples was added to the sample. In a matter of minutes the double-stranded DNA sequences in the dents was displaced by ssDNA by using strand displacement reactions (SDR) [36]. So the origami structure was able to get into the closed state due to a difference in elastic force between the ss- and dsDNA. This process can also be reversed by again adding ssDNA molecules in the solution. They hybridize with the other ssDNA part to form a double helix, and thus the structure opens again. Such an origami actuator can be used as a sensor for specific DNA molecules. Figure 6b shows the working principle of the actuator.

2.2 DNA-based biosensors and their characterization

DNA origami structures can be used to make biosensors. Establishing whether sensing has occurred is based on the readout method, such as atomic force microscopy (AFM), fluorescence imaging, or surface-enhanced Raman scattering (SERS) [37]. The methods will be further explained below by referring to recent examples.

2.2.1 AFM

The AFM is a microscope that can sample very accurate height information of a sample, by scanning a very small cantilever close to the surface. At the bottom of this cantilever is a very small tip ending with only a few atoms. An example of a tip is shown in Figure 7a. By rastering this cantilever across the surface of the sample, the atoms of the tip experience attraction and repulsive forces depending on the sample height. The presence of these forces result in a change in the height of the cantilever, and this height change can be detected. This detection is done by shining a laser on the end of the cantilever, and the cantilever reflects the laser onto a position-sensitive photodetector. This detector registers the changes in height as a function of position looking at changes in photocurrent from the reflected laser. With this method, height changes in the sub-nanometer range can be detected, Figure 7b shows the working principle of the AFM.

The AFM is commonly used in two different modes, contact mode and tapping mode. In tapping mode the tip vibrates over the surface at the tip's natural frequency, and touches it in between. This is useful for extracting height information when the sample is delicate. In contact mode the tip is dragged across the surface, with this the sample can be damaged but high-quality images can be generated. The AFM can be used to extract height and topography information from samples containing DNA origami structures, by generating very sharp images below the optical diffraction limit. For this project both the height and topography are of interest, and because the samples are very fragile, tapping mode is used.

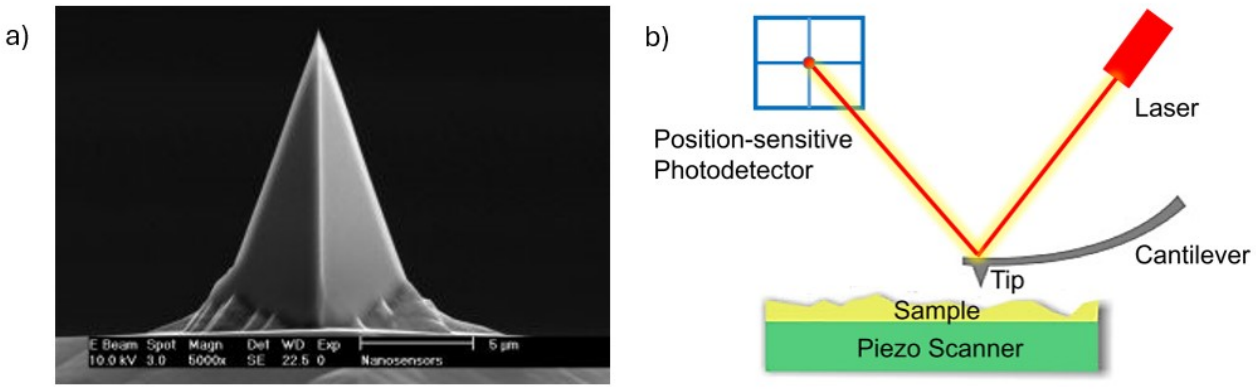

Figure 7: a) Example of size and geometry of an AFM tip, b) Schematic view of the working principle of the AFM [38].

The Yan group used rectangular DNA origami structures to detect hybridization events [39]. On the surface of their origami structure, they created 20 nucleotides long ssDNA segments to act as probe sequences. Then the solution with complementary DNA sequences was added to the sample to hybridize with the probe. The sample was then measured by an AFM, and places that appear higher are places where hybridization has occurred. The ssDNA probes that did not experience a binding event, could not be visualized due to the flexible nature of ssDNA. Figure 8 shows the AFM images of this process.

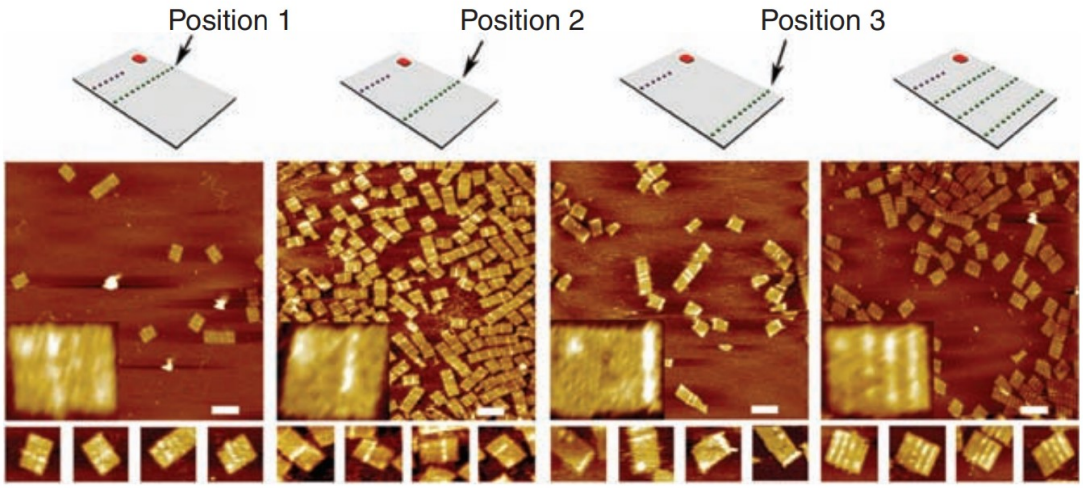

Figure 8: Top: Schematic overview showing how the surface should look like after binding. Bottom: AFM images of the structures with different binding formations

2.2.2 Fluorescence imaging

Fluorescence microscopy is based on the absorption and emission spectra of fluorescent molecules. A sample is illuminated with a laser or LED such that fluorescence molecules become excited, and subsequently emit in a longer wavelength, which can be detected by a camera. Figure 9a shows the setup of a standard fluorescence microscope. Regular fluorescence wide-field microscopes illuminate the entire sample volume with a laser perpendicular to the sample, which may give a low signal-to-noise ratio (SNR). The way to improve this is to use total internal reflection (TIRF) technique. With this method, the sample is illuminated under the critical angle, after which the laser is totally reflected at the interface of two media with different refractive indices. However, part of the energy of the incident light will be converted to the electromagnetic field and pass through the media interface. The resulting evanescent field, which can be seen in Figure 9b [40], illuminates a very thin height of the sample, around 100 nm, which minimizes background noise.

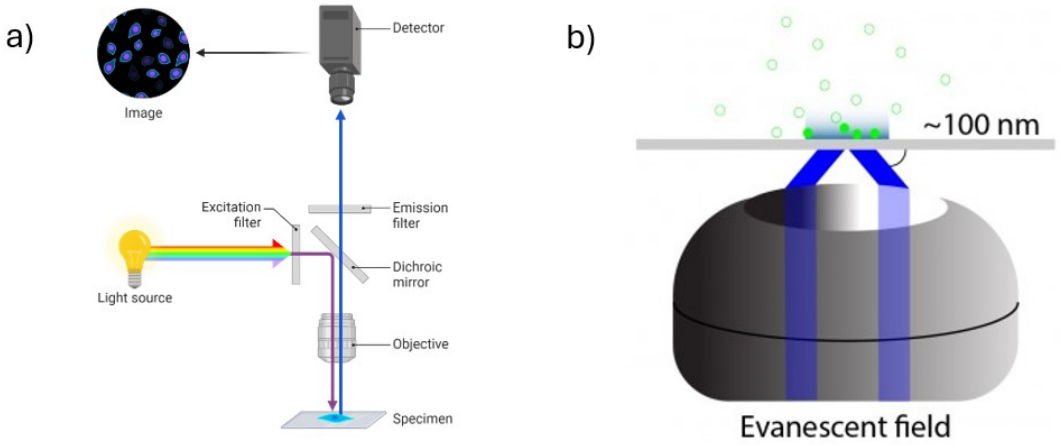

Figure 9: a) Wide-field fluorescence microscope setup, b) TIRF and generation of evanescent field for surface sensitive imaging.

Not all molecules fluoresce when excited, and most molecules convert their energy through vibrational relax-

ation, collisions, or internal conversion [41]. This is why in most cases small 3-15 nm fluorescent labels like cy5, cy3 and, atto576 are used. Each of them has a known chemical structure and emission spectra and can thus easily be distinguished in a measurement. These fluorescent labels can be used in combination with a molecule to facilitate binding or to place the label at a specific position. An example of this is by using a DNA molecule: the specific DNA sequence can make sure the label is positioned with high accuracy. This labeling technique also has disadvantages as it is not always easy to place a probe at a specific location, and before the labeling can happen, adjustments need to be made to the sample, or the sample structure needs to be well known. Moreover, despite the small size of the label, it can still influence the kinetics of the molecule and its conformation [42].

Jiang et al. used the fluorescent labels in combination with a DNA origami structure to create a circularly polarized luminescence signal [43]. By adding a biscyanine fluorescent dye to a DNA molecule consisting of 30 bp, they were able to attach this assembly to a DNA origami platform. Upon attachment the platform acted as a circular polarized emitter. Figure 10 schematically shows the formation of this template.

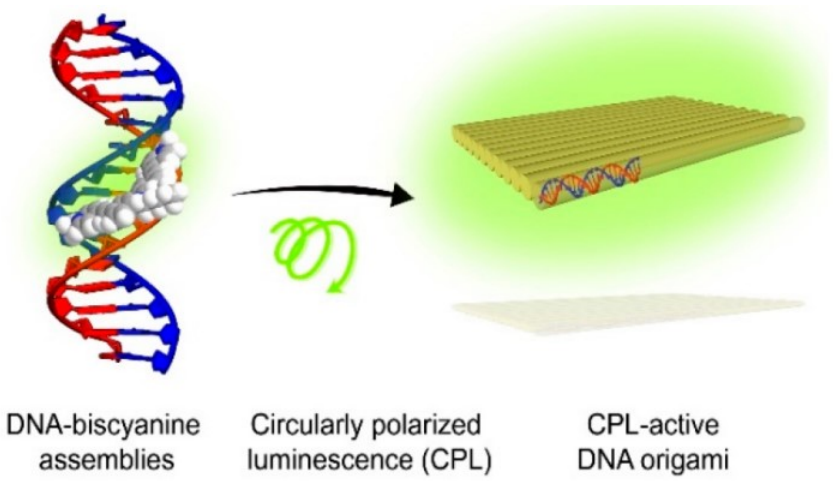

Figure 10: Fluorescence labeling of an origami rectangle

2.2.2.1 Nanoparticles

Besides fluorescent dyes, nanoparticles (NP) can also be used to visualize single molecules, especially gold nanoparticles (AuNP). AuNP are plasmonic nanoparticles that due to their small size exhibit a localized surface plasmon (LSP), which means that when they come in contact with an electromagnetic wave (such as light) the delocalized electrons in the NP start to oscillate [44]. The effect of this LSP is the enhancement of the electric field around the NP. This enhancement decays rapidly when going away from the surface. The LSP can be tuned by changing the NP shape, size, and wavelength of the incident light, with plasmonic effects of the gold nanoparticles being inversely proportional to their size. [45]. Moreover, the size of the AuNPs are bigger then that of fluorescent dyes (15-150 nm) depending on the application, the size can be chosen accordingly. Besides the enhancement of electric fields, AuNPs are also excellent fluorescent quenchers when near a fluorophore. This principle has been used to create a biosensor to detect Ago2 molecules, which can indicate a variety of human diseases including cancers [46]. Here Jiang et al. uses an AuNP in combination with fluorescent labels, utilizing the quenching effect of the AuNPs. By attaching fluorescence labels, consisting of a DNA molecule with a fluorescent dye to the AuNPs the fluorescence was not visible due to the quenching properties of the AuNP. When a complementary sequence binds to the DNA, they come loose and exhibit fluorescence. Using single-molecule counting, the number of loose fluorophores can be counted and a accurate estimate can be made about the Ago2 concentration.

AuNPs are also used in combination with DNA origami structures. Gür et al. positioned eight AuNP on a 6-helix bundle (6HB) DNA origami with protruding single strands [35]. Firstly, they bound single-stranded DNA to AuNPs using thiol modifications, as shown in Figure 11, reaction 1. Then they investigated the binding of the AuNPs and the 6HB via complementary strands hybridization. At room temperature, the AuNPs attach

to the 6HB surface within seconds. The quality of binding depends on the salt concentration, excess AuNPs and assembly order. This process is irreversible under conditions in which the origami structure is stable.

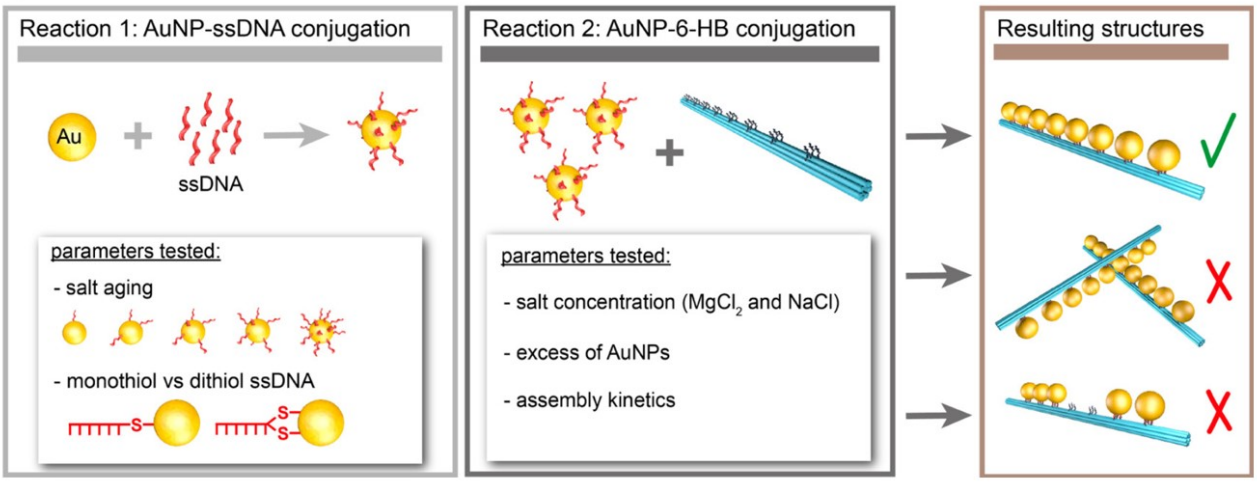

Figure 11: Process of binding the gold nanoparticles to the 6HB surface.

2.2.2.2 Additional methods

A standard fluorescence setup and therefore the application of NPs are still limited by diffraction. However, some techniques can be used to overcome this diffraction limit and localize molecules with nm precision. Two approaches to overcome the diffraction limit will be discussed below.

DNA-point accumulation for imaging in nanoscale topography or (DNA-PAINT) is a super-resolution technique that uses fluorescent probes. Upon bonding the fluorophores fluoresce for a short time, then the transient bond is broken and the dye diffuses back in the solution, a different probe binds, fluoresces, and unbinds. This process goes on for as long as necessary to get all the data from all the binding sites. Using a computer program to overlay these images, the position can be determined below the diffraction limit.

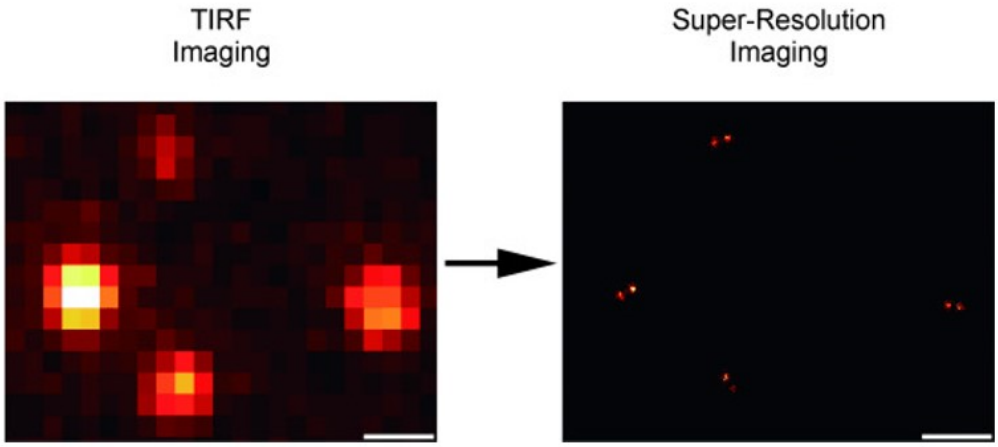

Figure 12: Left: TIRF image, the fluorescence coming from the individual probes is not distinguishable, the spot completely covers all four origami structures. Right: Super-resolution image, showing a more accurate position of the two probes on all four origamis.

As proof of concept for the super-resolution imaging, Steinhauer et al. created a DNA origami structure with two docking strands only 90 nm apart, and thus, well below the diffraction limit, to use as a nanoscopic ruler

[47]. On the top right and the bottom left corners of the origami structure, the fluorescent probes could dock to a complementary ssDNA molecule. They made multiple images using a fluorescence microscope to visualize the difference between a standard fluorescence image in TIRF regime, and an image using super-resolution imaging. The result of their measurements is shown in Figure 12, here the distinction between the two methods is clearly visible.

FRET is a non-radiative energy transfer between two fluorescent dyes or other light-sensitive molecules. A fluorescent 'quencher' in its electronic excited state may transfer energy to an 'acceptor' in its grand state via dipole-dipole coupling. This process depends on several parameters: donor and acceptor spectral overlap, their relative orientation and the distance between them. If the acceptor is not a fluorescent dye and efficiently absorbs the excited state energy, it is called a 'quencher' and there is no light coming from the molecule pair. The light intensity is inversely proportional to the 6th power, meaning that the intensity difference from the pair is highly sensitive to distance changes, which makes it an excellent measure of distance [48]. Dynamical behavior can now be determined below 10 nm, this is well below the diffraction limit.

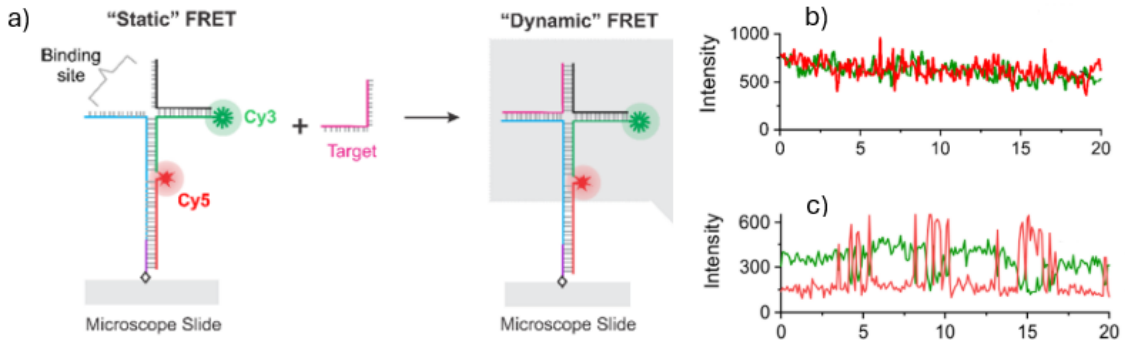

Figure 13: Working principle of the biosensor. a) Holliday junction composed of three ssDNA sequences, when the target strand binds to complete the junction the stiffness decreases and the junction becomes dynamic. b) Static response of the incomplete holliday junction without the target strand. c) Dynamic response of the complete holliday junction including the target strand.

Anoja et al. made a sensor using the FRET principle that consists of a holliday junction. This is a cross-like figure that is made from 4 ssDNA molecules [49], where two fluorescent dyes, a donor and an acceptor, are placed at opposite ends of the same DNA strand. Figure 13a shows the geometry of the holliday junction and the placement of the dyes (cy3 and cy5). The 'fourth target strand', whose presence can be detected by the sensor, is initially missing. The holliday junction itself without the target strand is static, which means that the FRET response is relatively constant. When the missing strand is inserted into the holliday junction the stiffness changes and the structure becomes more dynamic. Thus the hybridization of the strand can be detected via the change of the FRET dynamics and intensity.

2.2.3 SERS

AuNP can be used not only for enhancing their scattering coefficient, but also for enhancement of the scattering coefficient of their surroundings. A technique that uses this property is surface-enhanced Raman scattering (SERS). This technique uses Raman signals amplified by AuNPs by multiple orders of magnitude. It is commonly believed that the enhancement of the scattering coefficient is due to the enhancement of the local electromagnetic field by the oscillating surface plasmon resonance. SERS is a method which allows measuring the samples with single molecule resolution [50]. SERS needs almost no sample preparation and has a narrow Raman band, which makes it a powerful tool for biosensing. The disadvantage of this method is the inability of NPs to provide sufficient scattering signals by them self, this is why constructing assemblies with accurate spatial arrangement is crucial.

An example of a SERS biosensor is made by Prinz et al. [51]. They made a typical triangular DNA origami structure with two binding sites for AuNPs located 25 nm from each other. Three molecules of interest,

TAMRA, were able to bind between the NPs. By looking at the SERS spectra of the hotspot, the Raman peak corresponding to the TAMRA molecules can be distinguished. Figure 14 shows a schematic of the position of the AuNP and the TAMRA molecules in this experiment.

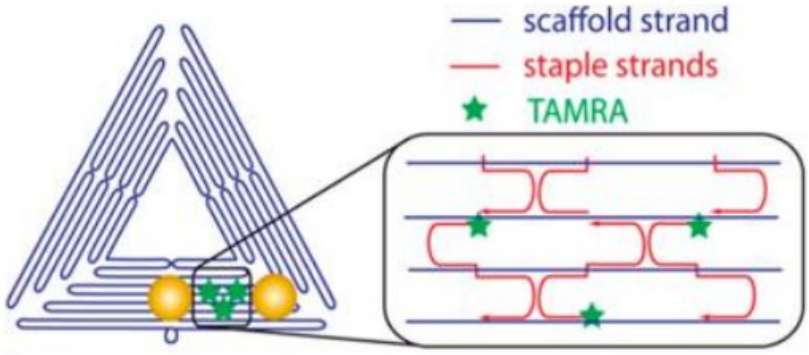

Figure 14: Schematic of the triangular origami sensing platform made by Prinz et al. The three stars indicate the TAMRA molecules and are positioned at the bottom between two AuNPs.

2.3 DNA origami array generation

There are multiple methods for organising DNA origami structures into 2D arrays. Five promising methods that are commonly used will be discussed below. These are lithographically patterning, sticky-end hybridization, blunt-end base-stacking, wireframe origami, and Zero Mode Waveguides. At the end of this section, we will justify which methods will be used in later research.

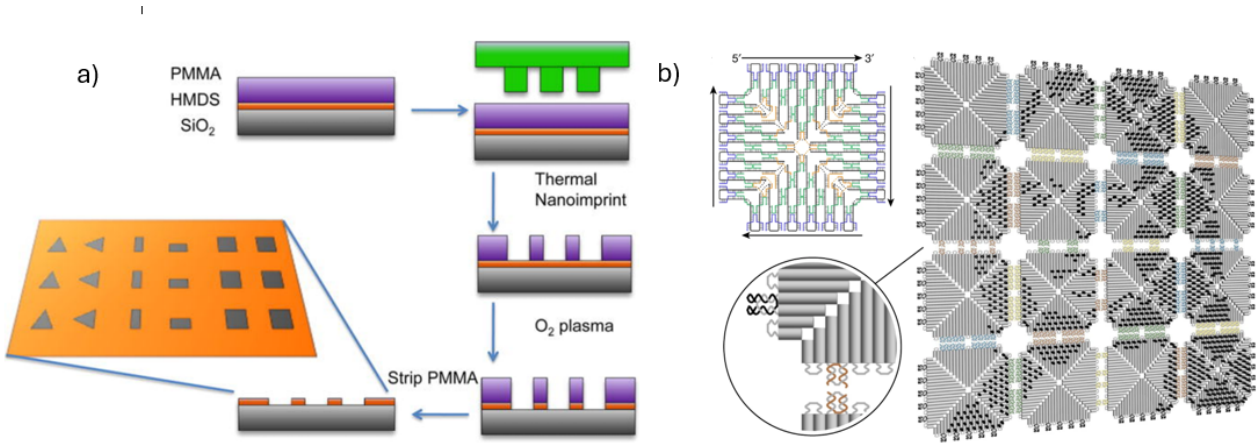

Figure 15: a) Schematic overview of the patterning process and top view of the patterned surface. b) Schematic overview of the sticky-end hybridization mechanism reconstructing the Mona Lisa.

2.3.1 Lithographic patterning

To assemble DNA origami structures in a 2D array, lithographically patterned surfaces can be used. With this method photolithography, electron beam lithography, or nanoimprint lithography (NIL) are used to pattern specific 2D structures on a surface to position the origami structures on [15, 52]. Using this method Penzo et al. created a 2D array of DNA origami structures with multiple geometries. They patterned triangles, rectangles, and squares on a surface using thermal NIL [15]. They used 3 material layers from top to bottom: PMMA, HMDS, and SiO_2. Then a mold patterned using an electron beam was thermally pressed into the PMMA layer to create the 2D patterns. Afterwards the layer of HMDS beneath the imprinted pattern was etched away, finally the residual PMMA and HMDS was rinsed away using an oxygen plasma cleaner. The origami structures were

placed upon the patterned substrate, and due to the hydrophobicity of HMDS and magnesium ions effects, the origami structures with the corresponding geometry were positioned in the desired position. The yield of this method was very high with very few cases of nonspecific binding. Figure 15 schematically shows the process and a top view of the patterned surface.

This method has the advantage of being able to create arrays of almost unlimited dimensions and various geometries. Also, the sizes of the origami structures do not have to be compatible, every tile is placed in its own patterned position. The downside of this method are the production of silicon substrates, the patterning of 2D structures, and the expensive and complex surface treatments.

2.3.2 Sticky-end hybridization

Sticky-end hybridization is based on the hybridization of complementary strands. To assemble different origami tiles, the edges of the origami need to be modified by placing a coplanar ssDNA sequence with a specific sequence and length there. Another tile in the same solution also has these strands at its edge, these strands are complementarity such that hybridization can occur. This method can arrange multiple origami structures in 2D arrays. The ssDNA sequences can be specifically coded such that only 1 specific tile can bind to another, this means that binding can occur with high selectivity. When trying to form arrays it is important to note that the annealing temperature during this step does not disassemble the origami tiles. When the annealing temperature of the arrays comes close to the formation of te single origamis, they disassemble.

This method was used to create a fractal assembly consisting of square origami tiles recreating the Mona Lisa portrait [16], which is shown in Figure 15b. From the image it is clear that to form the Mona Lisa painting, every tile only has one specific position, highlighting the placement specificity of this method. Other possible structures that can be made using this method are cross tiles creating a 2D array, and triangular-shaped patterns creating 3D structures [53, 54]. The downside of the method is the size of the 2D arrays, To specifically place every origami tile, every bond needs to have a different sequence to be able to achieve this. When the structure becomes large, the amount of different sequences that fit on such a small structure is limited, and the more the sequences overlap, the higher the chances of non-specific bonds.

2.3.3 Blunt-end base-stacking

In contrast to the sticky-end hybridization, blunt-end base-stacking uses π-bonds instead of hybridization to make arrays [55]. Due to this phenomenon, the ends of two double helix structures can form a π-bond when nearby. To make sure that the tiles find each other, Mg^{2+} ions are added into the buffer (typically already contained in origami folding buffers) to act as salt bridges between the negatively charged mica surface and DNA. This connection is (depending on the Mg^{2+} concentration) relatively strong. When divalent ions are substituted by monovalt ions, the tiles can diffuse along the 2D surface [56]. Due to the enhanced mobility, the tiles are more likely to find each other and form a bond such that large 2D arrays can be formed. This π-bond can be seen in Figure 16.

This method also has a downside. The specific placement of origami tiles in the arrays cannot be controlled. Also, the strength of the π-bonds is not as strong as that of the covalent bonds which leads to the final structures lower stability.

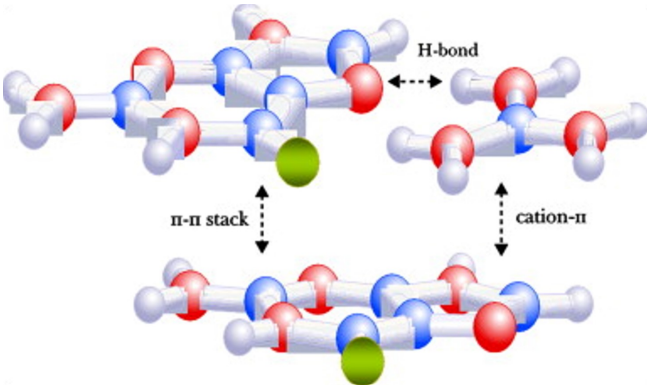

Figure 16: Illustration of the π-bond that facilitates the blunt-end base-stacking method [57].

2.3.4 Supramolecular Wireframe origami

Wireframe DNA origami makes use of parallel half crossovers together with lateral cohesive interactions between staples and the scaffold [58]. Wang et al. designed hexagonal origami structures using the program MENTIS with a six-helix bundel (6HB) edge, which facilitate binding due to multiple half crossovers on them. Figure 17 illustrates the binding principle of the origami tiles. Instead of having relatively large loose single-stranded DNA molecules at the sides like sticky-end hybridization, this method uses much shorter parallel half crossovers consisting only of staples. These staples have a specific sequence, and their complementary sequence is coded into the scaffold of another origami tile, such that specific binding can take place. Aside from the sequence specificity, selectivity is induced by varying the length of the extending staples such that nonspecific binding has a lower probability. The yield of fully bound 6 hexagonal structures after annealing was about 60 %. Wang et al. also made triangular-shaped origami tiles for self-assembly, where the assembly yield of these structures was between 60-75 percent, depending on the length of the overhangs.

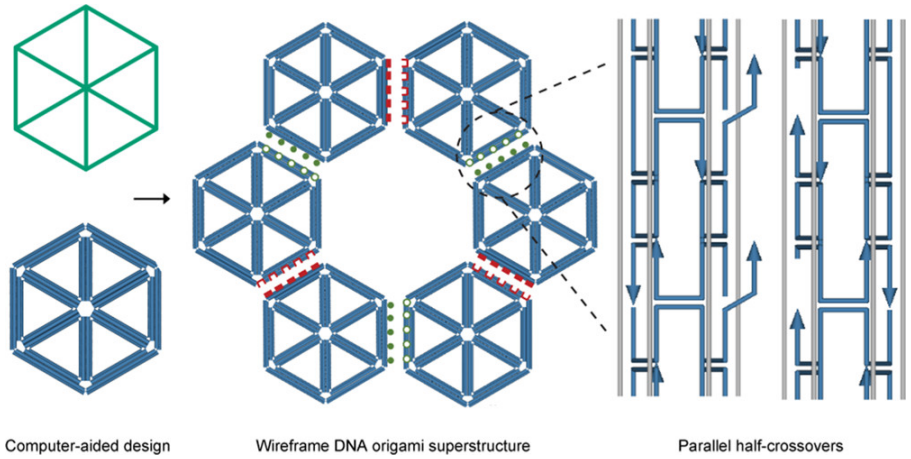

Figure 17: Overview of the wire frame bonding principle, on the left is the origami structure and the assembled structure, on the right is a schematic illustration of the bonding principle.

2.3.5 Zero Mode Waveguide (ZMW) array

ZMWs are small subwavelength holes in metal films. Due to their size they do not allow light propagation, yet when light is introduced from the bottom, an evanescent field occurs in the small volume that can be used to excite only the bottom of the cavity. As a result of the small volume, the target molecule can be imaged with minimal environmental influence such as other molecules present in the solution at higher concentrations, this method is frequently used for single-molecule imaging [59].

DNA origami tiles can be arranged by positioning them in ZMWs [60], Figure 18 shows the described method. Pibiri et al. used a 100 nm thick metal layer with ZMWs with sizes ranging from 120 to 200 nm. At the bottom of each of these holes, a biotin-functionalized surface with neutravidin molecules was present. The ZMWs are used to position circular origami structures with a fluorescent dye on top and biotin modification on the bottom to facilitate binding to the surface. A solution with these origami structures is placed on the metal film, they tend to enter the ZMWs and bind to the bottom surface. Due to the small size of the ZMWs, the holes do not allow light propagation, but an evanescent field does occur in this small volume, allowing very high SNR measurement within the ZMW volume. The occupancy of the ZMWs could easily be determined by using the evanescent field to detect the fluorescent molecules on top of the origami structures. This method has the advantage of being able to image small sample sizes with minimal background noise, when working with fluorescence signals this is very useful. It does have the disadvantage of not being able to place structures at a specific position, and the individual origamis are not in contact i.e. array density over the same area with respect to other techniques is lower.

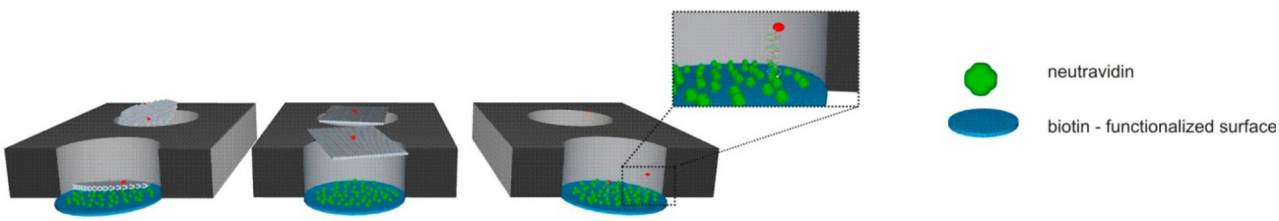

Figure 18: Process and binding principle of origamis in ZMWs

2.3.6 Conclusion

To be able to determine which of the methods will be used in further research, a table consisting of 5 requirements is made. They are rated from 1-4, 4 being the most essential and 1 being non-essential, every cell in the table has a color corresponding to their score for a better overview.

As we can see in from Table 1, all techniques have approximately the same score, only 'zero mode waveguide' scores relatively low. We can distinguish two requirements that are more important than the others, these are 'affinity to hBN' and 'specific placement', both of these play an important role in the forming of the array and the placement on hBN. If the placement of the origami tiles is done without knowing which tile is where, it becomes impossible to know what is detected after a measurement. If the structures have a low affinity to hBN, the formation of arrays becomes very challenging. Based on the results of these two requirements the following techniques are available: sticky-end hybridization and wireframe origami. These will be further investigated in the research section.

	Affinity to hBN	Bonding strength	Specific placement	Complexity	Annealing needed
Lithographically patterning	2; Binding affinity is dependent on the substrate that is used, due to the extra step it scores lower	3; Bonding strength is high due to the adhesion and placement confinement	3; Is possible by patterning different sizes and geometries	1; relatively complex due to the many complex surface treatments necessary	4; No annealing needed when making the array
Sticky-end hybridization	3; dsNDA does not bind with hBN, but ssDNA extensions can be added to facilitate binding	3; Hybridization between ssDNA can create a strong bond depending on the length	4; Due to sequence-specific binding high specific placement can be utilized	3; Relatively simple methods, no special materials or machines needed	1; Annealing is needed to form the array because hybridization needs to occur
Blunt-end base-stacking	3; dsDNA does not bind with hBN, nut ssDNA extensions can be added to facilitate binding	2; π-bonds are less strong then H-bonds	1; No specific placement possible due to random stacking of bases	3; Relatively simple methods, no special materials or machines needed	4; No annealing is needed, surface mobility is enhanced by adding gels or monovalent ions
Wireframe origami	2; dsDNA does not bind well with hBN, ssdNA extensions are more difficult to add with this method	3; Hybridization between ssDNA can create a strong bond depending on the length	3; Specific placement can be induced by altering docking sequences and varying the length	2; The structure has more requirements, such as the sides	1; Annealing is needed to form the array because hybridization needs to occur
Zero Mode Waveguide	2; Difficult to keep hBN pristine when doing FIB	4; When bonded in the ZMW the bond strength is very high	2; Precise localization within areas but no connected network	2; Relatively complex, the bonding procedures and the film with very small holes need to be acquired	4; No annealing is needed when forming the array

Table 1: Table of DNA origami assembly methods

2.4 hBN as a surface for DNA nano-actuators

As mentioned in the Introduction, this section will combine the DNA origami nanostructures with hBN surfaces. This section will introduce the material properties and usage of hBN and will explain the reasoning for using hBN as a novel surface for DNA origami.

2.4.1 hBN

hBN is a 2D material, also called a Van der Waals material, that has a hexagonal structure with alternating boron and nitrogen atoms. There are other 2D materials such as graphene, and also lesser known materials such as WS_2, MoS_2, $MoSe_2$, and WSe_2 [61]. 2D materials have nanometer thickness, this can range from 0.40 - 200 nm, and so can be thought of as only having two dimensions. Due to the atomic thickness of 2D materials, their properties differ from their bulk material. This is because the volume/surface ratio is different, meaning that there are relatively more atoms at the surface in comparison to the bulk material. Figure 19 shows the hexagonal structure of the hBN lattice.

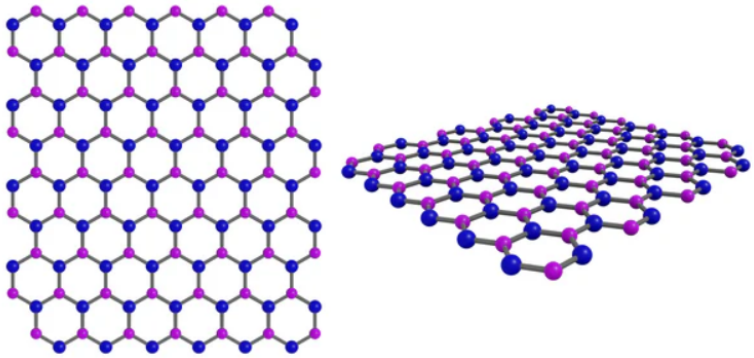

Figure 19: Schematic view of the hBN lattice structure

In contrast to graphene, which also has an hexagonal layered structure, hBN is an insulator with a wide 6 keV bandgap. Due to this bandgap, hBN does not absorb light in the visible spectrum and is thus transparent. hBN also has fascinating optical properties, the material does not auto-fluoresce but when defects are induced in the hBN lattice, they act as optical emitters. The chemical and structural properties of the defect determine the wavelength and stability of the emitters [62]. The special optical properties arise from the large bandgap of 6 keV of the material, which is much larger than other 2D materials. Within this bandgap, the defect can be optically active and have a ground and excited state within the bandgap. Using a sub-bandgap laser these defects can be excited and detected using a fluorescence microscope.

hBN is a material that cannot be found in nature. Usually, a single crystal bulk hBN is synthesized first. It can be made using various techniques such as the slow cooling method, temperature gradient method, or saturation [10]. After the bulk hBN is produced, hBN flakes can easily be peeled off from the surface. This is possible because non-covalent van der Waals interplanar bonds that form the layered structure of hBN are much weaker than the in-plane covalent bonds [10]. Removing layers of hBN can be done by exfoliation. The most simple example of hBN exfoliation is by taking a piece of sticky tape [63], and placing it on the hBN surface. By slowly removing the tape, the flakes on the piece of tape can now be visualized by AFM of TEM, there are alternative exfoliation techniques such as hydrothermal exfoliation or ultrasonic exfoliation [64, 65]. These techniques more easily damage the structural properties by inducing more defects.

2.4.2 Using DNA origami with hBN

DNA origami motion and assembly on hBN is a relatively new topic that gained significant attention only in the last couple of years. An example of combining hBN with origami structures has been performed by Wang et al. They used the optical properties of hBN nanoparticles (NPs) [66], and combined these with a DNA origami nanopore with staple extensions at the edges of the nanopore. Figure 20a shows the schematic of this origami structures with a clear view of the staple extensions at the edge of the nanopore. The ends of these extensions were used to capture the hBN nanoparticle these nanoparticles host crystal defects and thus act as optical emitters under different excitation wavelengths and could be positioned with nanometer precision due to π-stacking interactions between the bases and the hBN surface. Figure 20b shows the AFM images before and after the addition of hBN NPs, the height difference at the position of the extensions is clearly visible as the brighter feature.

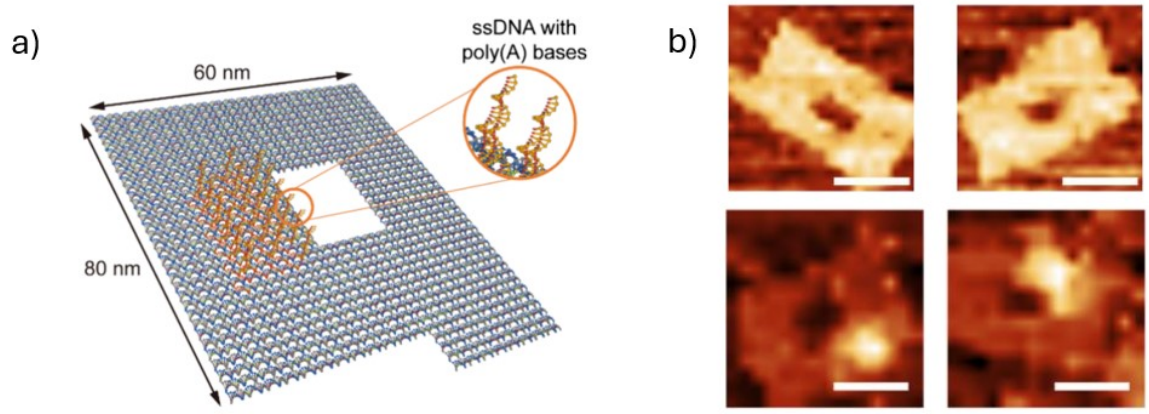

Figure 20: a) Schematic of DNA origami made by Wang et al. b) AFM images before and after the addition of hBN NPs.

Shin et al. mapped the movement of ssDNA across an hBN surface. They used a ssDNA molecule with a fluorophore attached to the end, and positioned it on pristine, untreated hBN [67]. They mapped the diffusion of the fluorophore across the surface and found out that the ssDNA molecule diffuses freely across the surface but is limited by the edges of the hBN flake. When coming across a step edge on the hBN it resulted in reduced mobility of the DNA molecule and the confinement within the boundary domain. Figure 21 shows an image of the experimental setup used to track the DNA across the hBN surface.

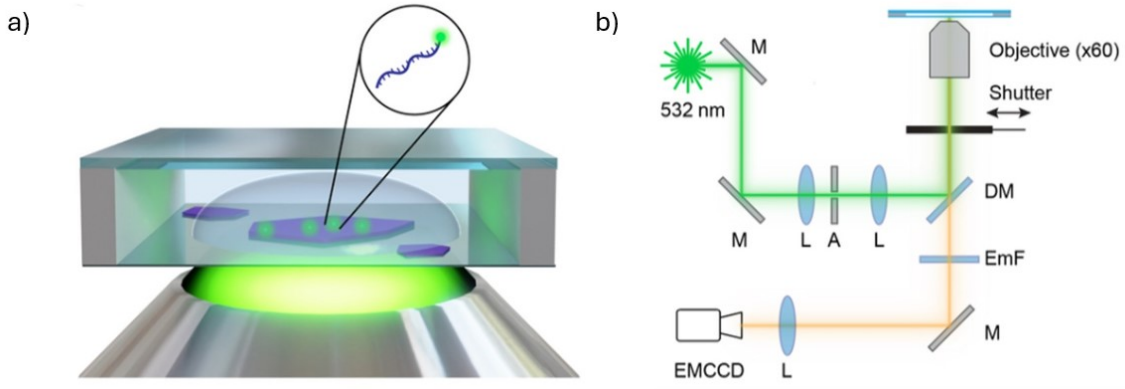

Figure 21: a) Experimental setup of the hBN flake and the DNA molecule is shown. b) Setup for the microscope used for the single-molecule imaging experiments [67].

The binding between hBN and dsDNA has been researched by Sülzle et al. [68]. They developed a method to image the binding between hBN and dsDNA in liquid without labeling the sample. By using interferometric

scattering (iSCAT) microscopy, they could visualize the transient binding affinity of dsDNA to hBN. It became clear that dsDNA prefers binding to defects and edges in the hBN. Defects in the hBN were induced by using a focused ion beam, the binding between these defects in hBN and dsDNA molecules could be visualized. They also tried to measure the motion of dsDNA along specific tracks etched in the hBN by the focused ion beam, but they were not able to measure this phenomenon.

Zhan et al. made a molecular switcher that makes use of the overlapping chemical properties of hBN and DNA [69]. They positioned a ssDNA molecule with a known sequence on hBN in combination with a fluorescent dye, due to π-π bonding this molecule bonded to the hBN. Via photo-induced electron transfer (PET), the fluorescent dye was quenched and thus not visible under the fluorescence microscope. When adding the complementary sequence to the solution, it hybridized with the other DNA molecules forming a double helix. Now the π-π bonding is not possible anymore and the DNA comes loose from the surface, due to the distance-dependent quenching behavior of hBN the fluorescent molecule can be detected. This contradicts the experimental findings mentioned above regarding the retention of florescence properties of the dye close the the hBN surface.

Tinnefeld et al. investigated the conformational changes of DNA strands attached to graphene. They illustrated that the different chemical structures of ssDNA and dsDNA interact differently with the hexagonal graphene substrate. Figure 22 shows three DNA strands that are partially ssDNA and partially dsDNA. The ssDNA, due to their overlapping chemical structure of the DNA bases and graphene, binds to the surface while the dsDNA does not. The results from this paper are of importance for this research because while the substrates are different, the crystal structure of graphene and hBN closely overlap. This is very promising for this project, because a comparable actuation mechanism will be investigated as an extension of this thesis work.

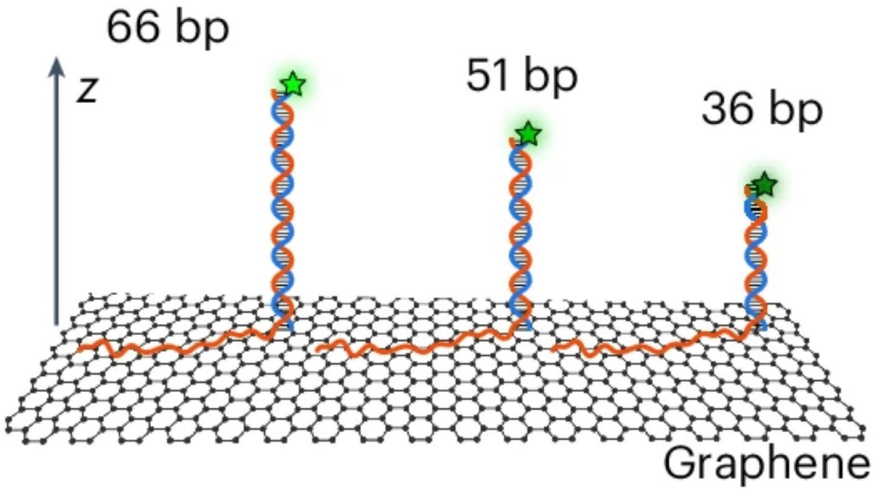

Figure 22: Schematic of DNA strands positioned on a graphene substrate. The ssDNA part binds to the surface while the dsDNA does not.

The mapping of the interactions between hBN and DNA origami structures are far from complete. This is why the research investigated and proposed in this review is novel and promising for future biosensor geometries.

3 Experimental methods

3.1 DNA origami preparation

One of the main components of this research is the successful folding of the origami structures. In this section, the methods that are used for DNA origami are listed and explained. These are in particular the assembly of origami structures, filtration, annealing, and agarose gel electrophoresis (AGE).

3.1.1 Assembly and characterization of origami structure

In this research I used the origami made by Wang et al. [66] The structure described in this paper is shown in Figure 23. The 2D DNA origami is made from 39 helices, and has dimensions of 60x80nm with 30 ssDNA extensions protruding from the left of the hole. The advantage of this structure is the designed 'tail' on one side, which allows immediate visual spotting of its orientation (i.e. top to bottom) on hBN and mica.

The original structures were not specifically designed for forming arrays or dimers, because their sides end in ssDNA extensions, not specifically designed for sticky end hybridization. The sides can be functionalized to form random 1D arrays or dimers. This can be done by including the 'edge staples' into the solution. These staples are complementary to the ssDNA extensions on the sides, such that they now become dsDNA extensions. When the sides of the origami are made of double helices, blunt-end base stacking can occur. With this non-specific binding method, random 1D arrays and dimers can be formed [70]. When the edge staples are not included, arrays can not be formed because the ssDNA extensions are not rigid enough to form the π bonds that facilitate blunt-end base stacking.

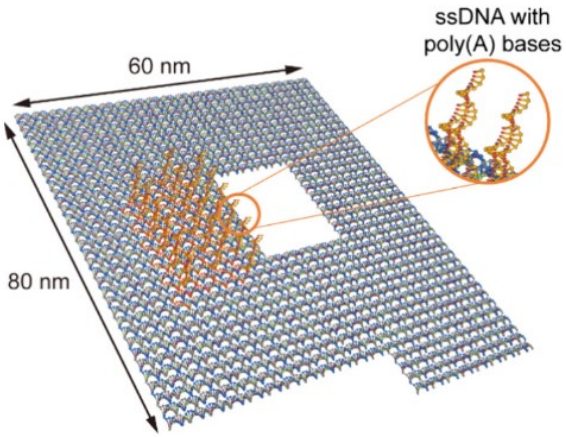

Figure 23: Schematic of the origami structure made by Wang et al [66].

To generate the origami structures, scaffold from the M13mp18 phage, consisting of 7549 nucleotides, was mixed with complementary edge staples, divalent magnesium ions, TAE buffer, and milli Q water. The concentrations and volumes of these components are shown in Table 4, ending with a total volume of 50 μL. The presented recipe is valid for the DNA origami without the edge staples, containing 131 different staples. When the edge staples are included, the number of staples increases to 167 and the staple volume to 4.2 μL. The staple volume in Table 4 refers to the concentration of each staple, not the total staple volume. Other recipes, such as the creation of arrays, can be found in the supplementary information.

Component	Concentration bulk	Desired concentration	Volume
Scaffold	100 μM	10 nM	5 μL
Staples	100 μM	50 nM	3.5 μL
Mg^{2+}	100 mM	12,5 nM	6,25 μL
TAE	100 mM	10 nM	5 μL
Milli Q	M	M	30,25 μL

Table 2: Concentration and volumes assembly of DNA origami structure without edge staples.

Step 1: Annealing

After all components are mixed within the right volume and concentrations, the aliquot is put into the thermal cycler T100, which precisely controls the heating and cooling of the samples at a defined rate. The DNA origami annealing procedure used in this work involves heating to 90 °C for 5 minutes, followed by a gradual temperature decrease at a rate of 1 °C per minute until reaching 20 °C. The whole annealing protocol lasts roughly 6 hours.

Step 2: Filtration

Excess oligonucleotides were removed via ultrafiltration, with the Eppendorf 5420 centrifuge. First, a 100 or 50kDa Amicon Ultra 0.5 mL Ultracel filter containing 50 μL of the origami sample and 400 μL of TAE with 15 mM Mg^{2+} buffer was put into an aliquot. The aliquot including the filter was put into the LOT VL211, and the sample was centrifuged at 4000 rpm for 3 minutes. Afterwards, the filter was gently removed and the residual liquid in the aliquot emptied. The filter was placed back, and again 400 μL of the same buffer (TAE with 15 mM Mg^{2+}) was added. This round of ultrafiltration was repeated three times. The fourth time the filter was put upside down in a new aliquot to prevent contamination, and centrifuged on a different program, namely 2000 rpm for 3 minutes.

Step 3: Agarose Gel Electrophoresis (AGE)

To do a preliminary check to see if the origamis are folded, I used the AGE method. The agarose gel was created by taking 0.6 g of agarose combined with 42.5 mL of running buffer, and heating until the agarose was completely dissolved. The running buffer consists of 2.5 mL Mg^{2+}, 25 mL of TBE and is diluted with milli Q water until 500 mL. The mixture was then poured into the mould to solidify. Afterwards, the gel was placed into the electrophoresis unit and filled with running buffer until completely covered. The sample containing 5 μL filtered DNA origami sample and 1 μL was put into to designated wells. An electric potential of 80 V was applied for 70 minutes. Finally the position of the DNA origami bands was visualized on a UV transilluminator under high intensity UV light.

Step 4: Origami transfer to mica and preparation of the AFM sample

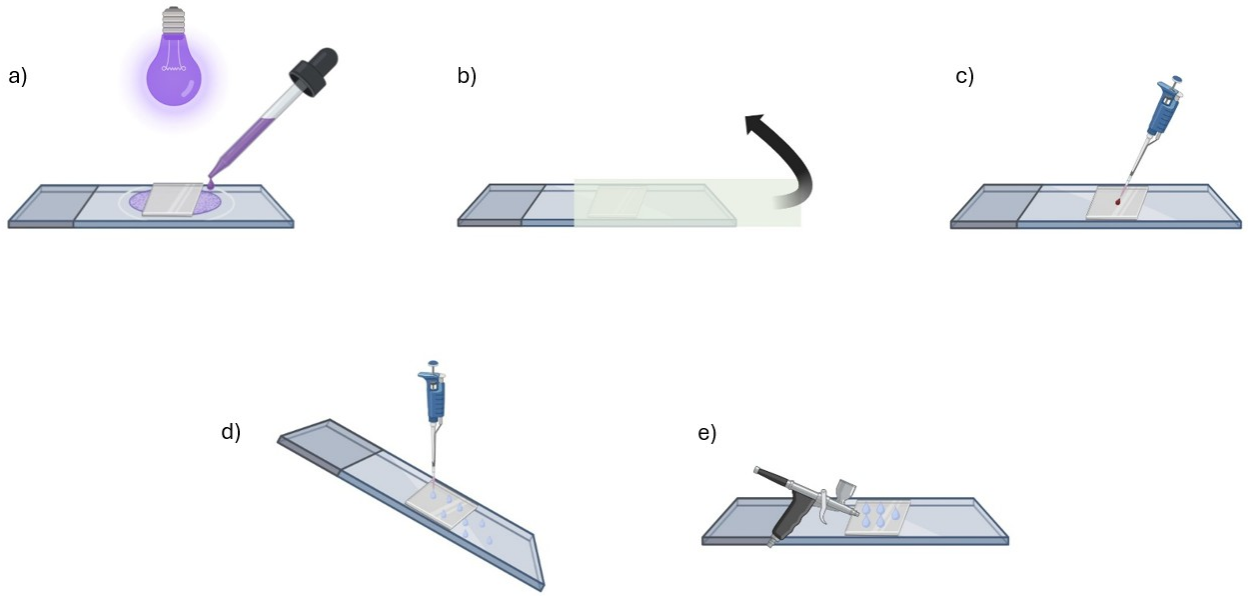

Figure 24: Steps regarding transfer of origamis to mica. a) Positioning the mica sheet on top of the glue and curing it with an UV lamp until the glue is dry, b) exfoliating the top layer(s) of mica to assure a clean working area, c) pipetting the origami solution on the mica surface, d) rinsing the mica surface with 200 μL of water to get rid of the salt and non-adsorbed origamis, e) drying the surface with a nitrogen gun to evaporate the water and freeze the origamis in their position.

After the origamis passed the AGE test, they can be positioned on mica to be visualized with the AFM. The preparation of mica goes as follows. First, a square of approximately 1x1 cm was cut from a mica sheet. The small piece of mica was then glued onto glass surface such that it could be placed under a microscope. By placing the glued mica under an extreme UV lamp for 2 minutes, the glue is cured, and the mica is immobilized. The glue is transparent, such that the sample can be visualized by illuminating it from the bottom with a microscope. This sample with the mica can be used repeatedly.

Now that the mica is immobilized on the glass surface, it needs to be prepared, this is done by exfoliating the top surface before each measurement. The mica material is composed of layers that are held together by $\pi - \pi$ stacking bonds, which can easily be overcome such that thin layers can be removed to create a fresh and clean surface. This exfoliation was done by placing a piece of sticky tape over the mica piece, covering the entire mica surface, and ripping it off quickly. By looking at the cleaved mica on the tape, it can be determined if the whole mica surface has been renewed. This process is repeated 1-3 times until the whole surface is new.

Now that the surface is clean, it is ready for origami deposition. 3.5 μL of origami solution was placed in the center of the mica surface. After waiting 40 seconds for the origamis to adsorb to the surface, the mica surface was washed 3 times with 200 μL of milli Q water to erase any residual salt and origamis.

Finally, the surface was dried with cold air by going from top to bottom over the mica surface with the air gun, until all the residual liquid was removed. Then the origamis were ready for visualization. The schematic representation of this protocol is depicted in Figure 24

3.1.2 Glass cleaning

For the preparation of glass, a more complicated cleaning procedure is used because glass is not atomically smooth and is usually quite dirty. First, the glass coverslip is taken from inventory, and a couple of glass substrates are put into a holder and lowered into a beaker to be fully submerged in Acetone. The beaker is covered with aluminum foil and placed into the Branson 1800 sonification machine, and is ultrasonically cleaned for 3

minutes. After this, the acetone is thrown away and replaced by Isopropanol. Again, the glass substrates are fully submerged in the liquid and are ultrasonically cleaned for 3 minutes. Now the surface needs to be dried, and I did this using compressed air. By blowing the water droplets from the surface and carefully placing them in a container for storage.

For cases where the glass substrate needs to be exceptionally clean, as an extra step the glass substrates are cleaned using the oxygen plasma cleaner. The glass substrates are placed in the oxygen plasma machine, and plasma cleaned for 10 minutes. The now-cleaned glass coverslips will be used as a substrate for hBN flakes.

3.2 Visualization

The two MAIN visualization methods i used in this work are AFM and Fluorescence widefield microscope. The following section contains information about the setup and protocols

3.2.1 AFM

The AFM used in this research is the JPK Nanowizard 4, and is used to make high-contrast images by measuring the sample topography. Two different modes have been used, these are Alternating Current(AC) mode and Quantitative Imaging(QI) mode. AC mode vibrates over the surface at its natural frequency, while touching the surface periodically at certain increments. This way it generates high quality images about the surfaces topography. In this work i used the TESPA-V2 with an natural frequency of 315 kHz. QI mode does not use the frequency to determine the topography of the sample, but does this following a force displacement curve. The tip moves across the surface, and touches it periodically at certain increments. When the tip feels the repulsive force form the interaction between the tip and the sample it registers this, with this the height information can be extracted. With this method the CONTR-50 tip was used. Figure 25 shows the AFM setup that was used and denotes its important components. All measurements were conducted in a dry environment.

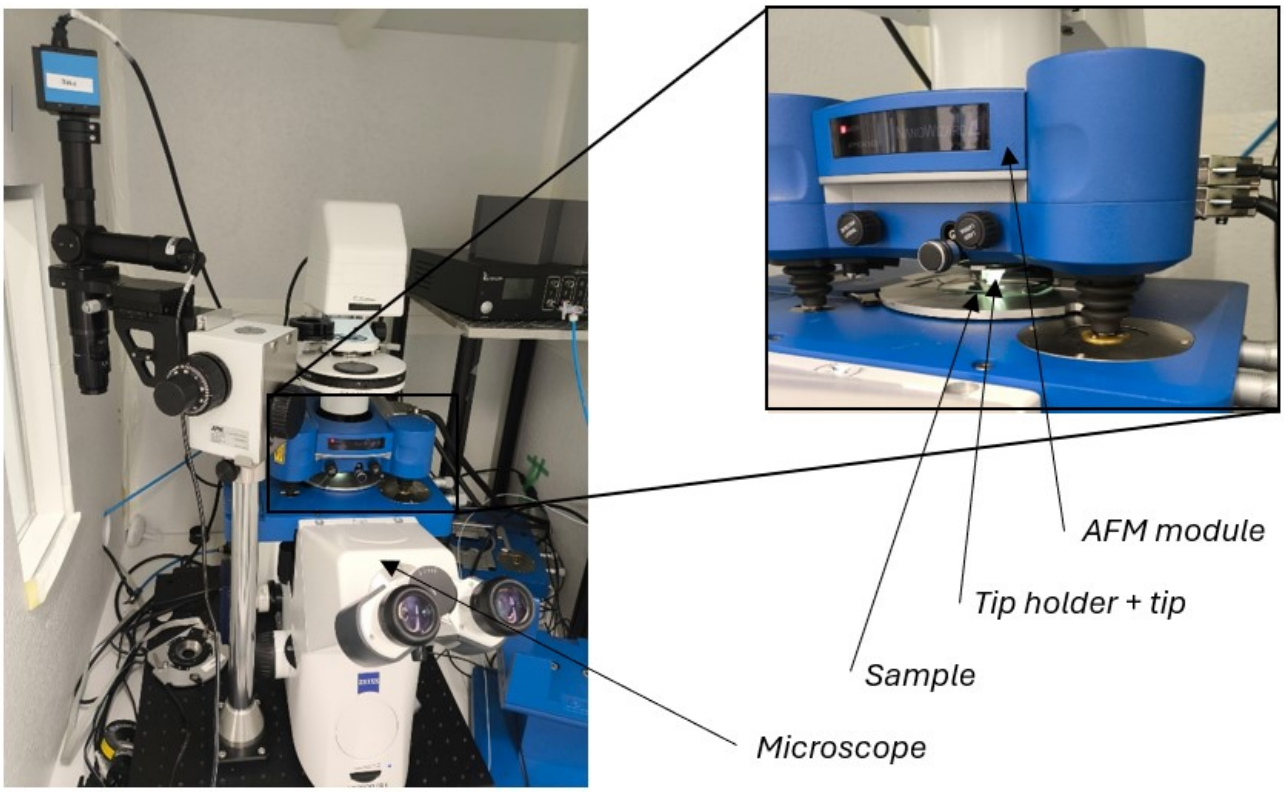

Figure 25: Schematic and main parts of JPK Nanowizard 4 used in this work

3.2.2 Widefield microscope

For single molecule experments I used the inverted microscope (Nikon Intruments, Eclipse Ti2) with 100x oil-immersion objective (nikon instruments, TIRF x100/numerical aperature 1.49). During the measurements the total internal reflection (TIRF) angle was used, which enabled a higher signal to noise ratio. The setup has three different laser, enabling blue (473nm), green (532nm) and red (640) excitation. Measurement done in this work were measured via 640nm excitation with 661-690 emission filter. The fluorescence movies and images were collected by a sCMOS camera. Before each experiment the hBN flake was ound beforehand by used the white light illumination module built in the setup. This allowed to find the sample surface without potential bleaching of the fluorophores. Figure 26 shows the setup and highlights important parts.

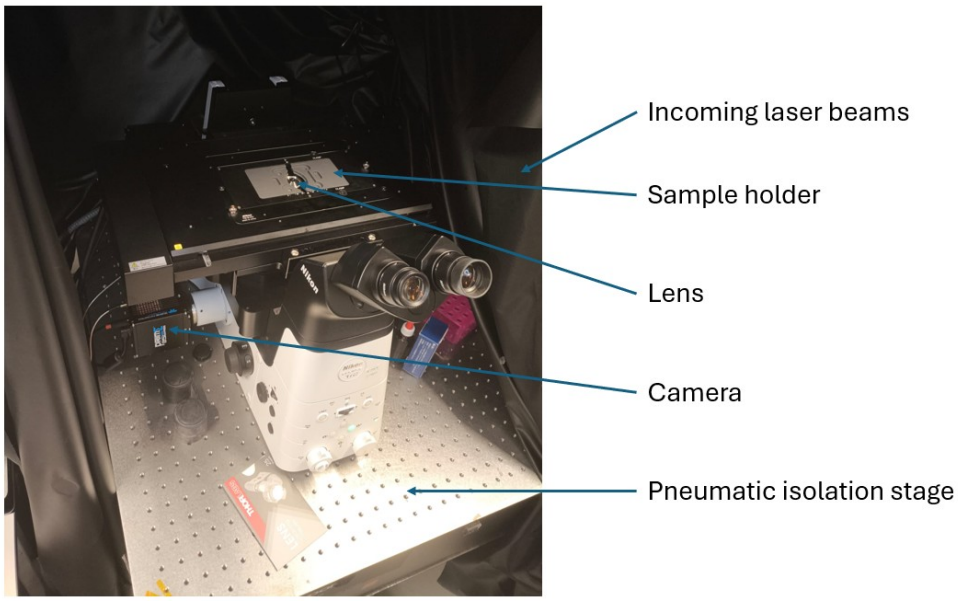

Figure 26: fluorescence setup, highlighting important parts.

3.3 hBN transfer to glass

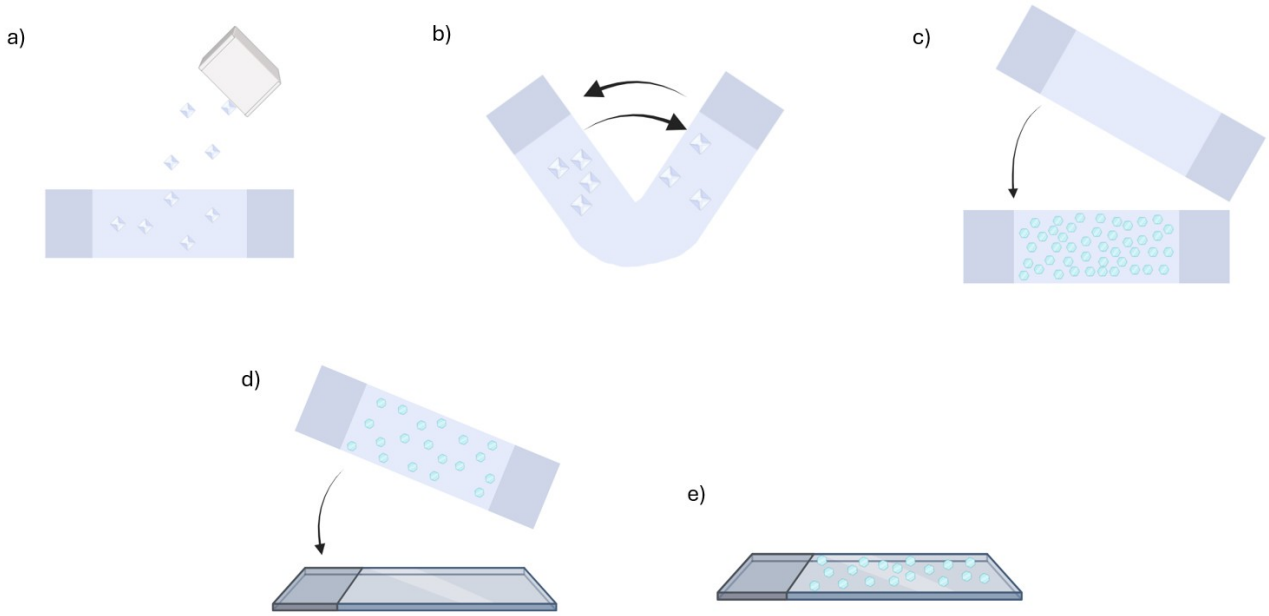

Figure 27: Schematic viusalization hBN transfer procedure, a) deposition of large hBN crystals on scotch tape, b) opening and closing of tape to distribute hBN crystals, c) placing tape on another tape to decrease the yield, d) placing tape on glass for hBN transfer, e) final result of hBN flakes on glass.

Before the origamis can be deposited on hBN, the hBN needs to be transported onto a surface, this was done on glass. This was chosen due to its transparency and its smooth surface. The following method was used to transport the flakes onto the glass surface.

First, a new piece of scotch tape (Magic Tape, 3M) was taken and placed with the sticky side up, onto a piece of aluminum foil. The edges were folded inside such that they could be handled properly. Now, small hBN crystals were distributed over the tape, after which the tape was opened and closed repeatedly such that the entire surface was covered in thin hBN flakes. This piece of tape can be closed and used repeatedly until the yield upon transfer becomes too low, then the process needs to be repeated. To get rid of glue and to decrease the density of the flakes, the flakes were transferred to another piece of tape. By placing the previously made tape on the new, fresh tape, the flakes can be transferred. The tapes need to be pressed together, and air bubbles need to be removed to get the best overlap. After all air bubbles were cleared, the two pieces of tape were slowly peeled off each other. The first tape can be closed and stored, while the second tape is placed on a clean glass coverslip. Again, air bubbles were cleared, and the tape was pressed firmly on the surface to guarantee contact. Finally, the tape was slowly pulled off the glass coverslip, showing hBN flakes covering the surface. The second tape was also closed and stored, both of these tapes can be used repeatedly, until the yield decreases too much. Figure 27 visualizes this procedure.

4 Results

4.1 Changing origami properties with caDNAno

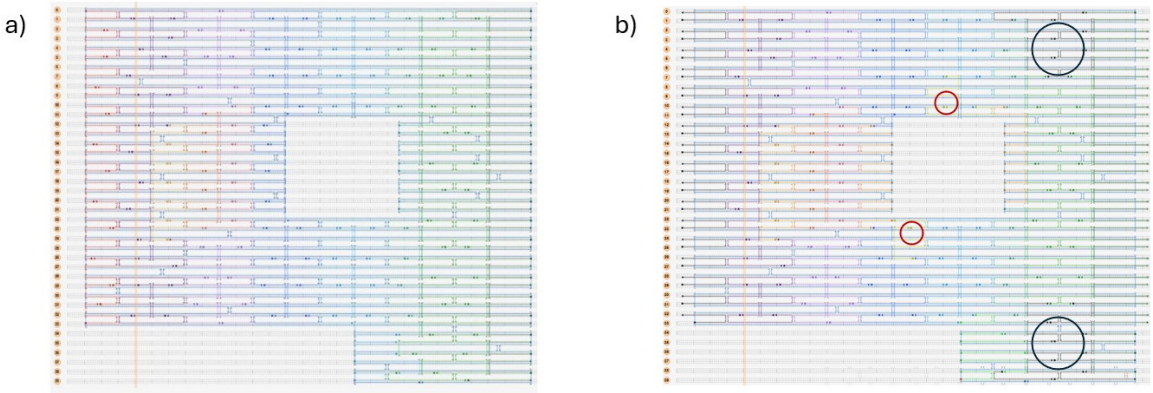

Figure 28: a) Origami designed by Wang et al. b) Adjusted origami structure with 33 staple extensions on each side consisting of 6 bases. The Red dots indicate docking strands for fluorescent dyes, and the black dots indicate the 30X A extensions for adsorption to hBN.

The origamis used in this research are made by Wang et al. but have a disadvantage when trying to control the formation of arrays. Due to the blunt-end base stacking mechanism that allows for random attachments. For this research, the DNA origami structures have been altered such that sticky end hybridization facilitates the bonds between origamis. The origami nanopore was designed using the caDNAno2 software. Figure 28 shows the layout of the origami structure in the caDNAno2 software. To be able to control the formation of arrays, the edges of the helices have been altered such that the left side has complementary sticky ends to the right side. Figure 29 visualizes this connection. Each side is equipped with 33 extending staple strands consisting of 6 bases. Due to the helicity of the helices, the origamis have to be slightly shifted in height in order to form a bond. The origami is designed with 19 extending ssDNA strands near the nanopore, consisting of 30 A bases. Originally, this was meant to catch hBN nanoparticles for fluorescence imaging. But now this area will be used to attach to the hBN surface and form π stacking bonds to immobilize the structures.

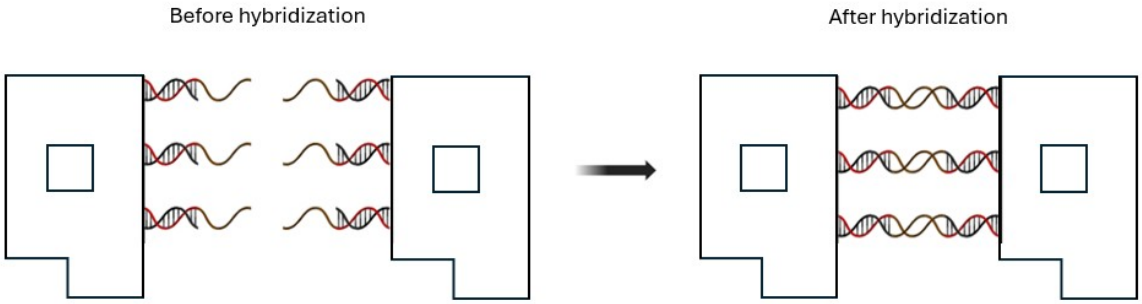

Figure 29: Visualization sticky end binding mechanism, before and after hybridization.

When designing the origami structure, no attention was paid to the formation of kinetic traps that arise from using too many cross-sections in close proximity. This results in the formation of origami structures with internal stresses, and subsequently in the bending of the structure after folding. Deformation due to these stresses is visualized in Figure 30. To prevent the origamis from curling up and deforming when trying to attach them to the hBN surface, two more locations with a 30 A base extension called docking staples were added to the design. The locations of these extensions are visualized in Figure 28 with black circles, each of which has 6 docking staples. The locations are chosen based on the highest deformation according to Figure 30. Moreover,

two binding sites for attachment of fluorescent labels were created. The red dots in Figure 28 show their locations. Each fluorescent dye is attached to an ssDNA sequence consisting of 30 bases, which terminates with an ATTO647N dye.

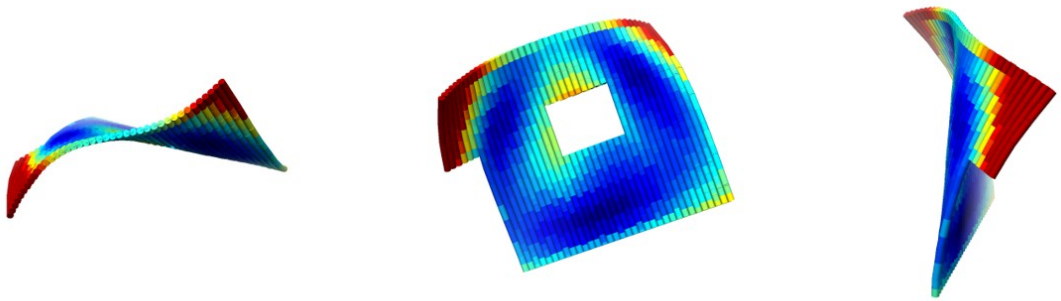

Figure 30: Deformation graph of origami structure showing bending after folding.

4.2 DNA origami on mica

Before the DNA origami structures can be placed on hBN, they are placed on mica to determine if the origami structures are folded, given that mica is proven to be a good substrate for origami structures. This section will make a distinction between single origamis with and without docking staples.

4.2.1 Origamis without docking staples

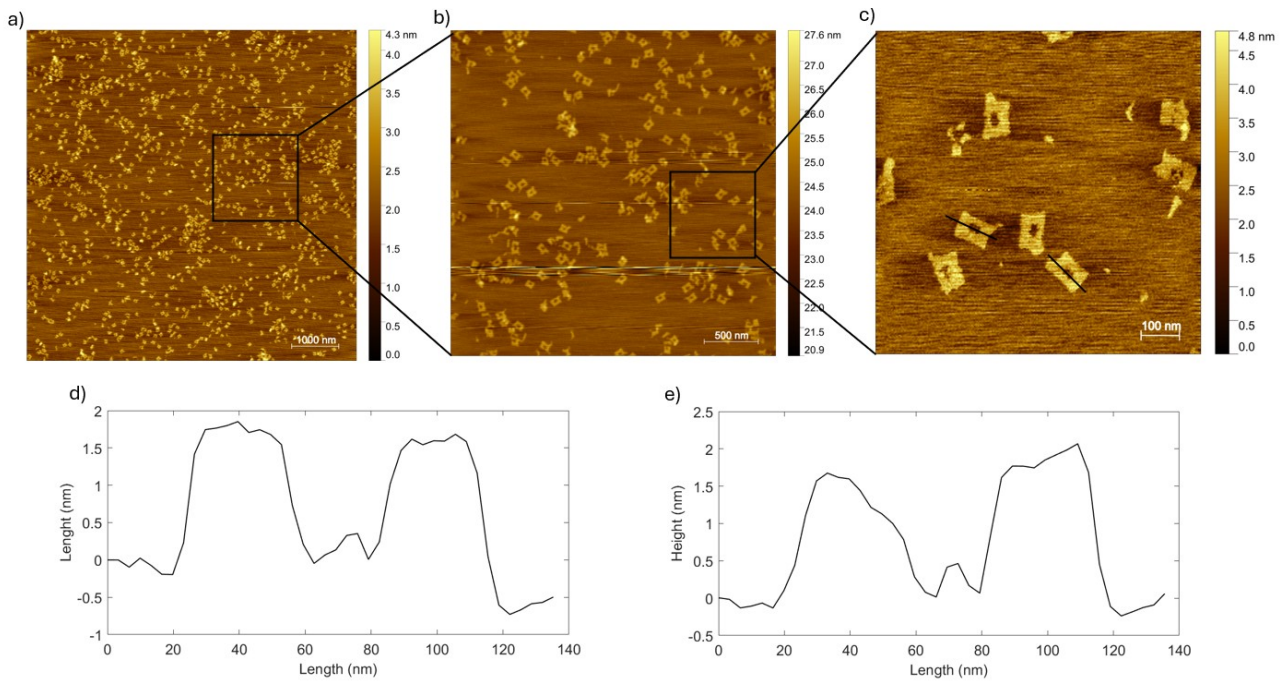

Figure 31: AFM images depicting different fields of view. a) image in AC mode, large field of view showing large amounts of origami structures, b) image made in AC mode, individual origamis become more visible, and asymmetrical features also become visible, c) Image made in QI mode, origami geometry including asymmetrical feature are visible, d-e) height traces of two different origami structures along the length.

Figure 31(a-c) shows three AFM images showing different origami views, going from a large area to a zoomed-in image, respectively. The smaller the field of view, the more accurate the asymmetrical features of the origami structures can be distinguished. For all images, 100 KDa filters were used. The size of the individual origami structures is around 30 KDa, to make sure the right filters are used, a sample with a 50 KDa filter was produced. The results did not differ from that of 100 KDa, images can be found in the supplementary information. To get a better understanding regarding the height trace of the origamis, Figure 31d and e show height traces covering two origamis. The traces show the expected origami geometry and size. 68 % of the origamis land with their protruding docking staples away from the surface(on their top), and 32 % flipped with the docking staples towards the surface(on their bottom). No difference was detected in the sizes of origamis with different orientations.

4.2.2 Origamis with docking staples

When forming origamis including the extending docking staples, in addition to those already implemented by Wang et al. the staples that were previously implemented in those positions need to be changed. A total of 5 staples were removed, where 17 staples were changed to the new ones. The specific rearrangement can be found in the supplementary information. The edge staples were not implemented. To be certain that the single origamis including the docking staples are stable, they were first placed on mica for inspection. Figure 32 shows the results. It is clear that the origamis are stable, although the yield has slightly decreased. This could be due to steric hindrance when implementing staples with large extending DNA sequences. 64 % of the origamis have landed on their top, and 36 % on their bottom. These numbers closely resemble those of the results of origami without extra docking staples.

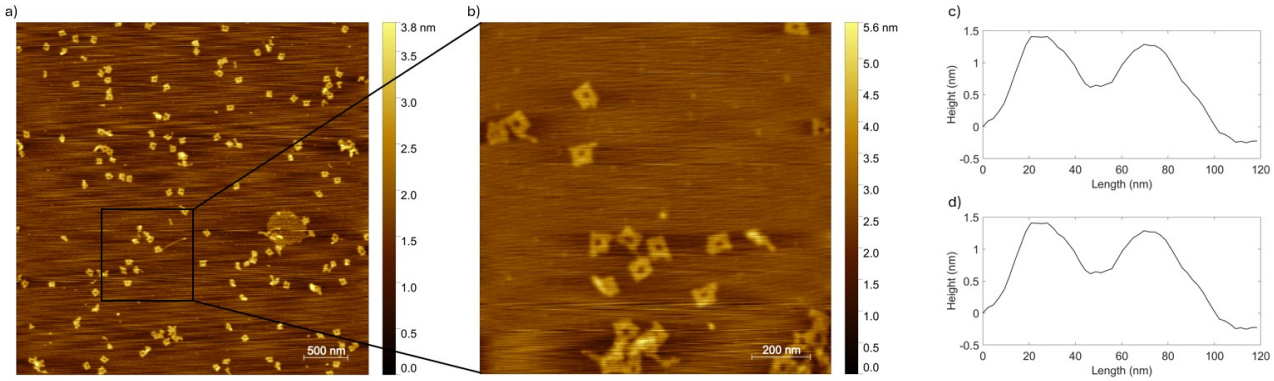

Figure 32: AFM images DNA origami structures including docking staples. a) large field of view showing folded origami structures, b) zoomed-in image clearly showing the origami geometry, c-d) height traces of two different origami structures along the length.

4.3 Forming arrays on mica

For the formation of arrays on mica, two different sets of DNA origami structures were made: with and without docking staples. The results are described in the following paragraph.

4.3.1 Arrays without docking staples

In order to create DNA origami arrays, the protocol must be modified as the simple addition of the edge staples to one sample with other components for annealing led to no formation of DNA structures. This could have happened due to the large size expected from the arrays and incorrect choice of concentrations. Afterwards, a new method was designed: first, the single DNA origami structures were folded without any edge staples. Subsequently, all edge staples were added, with concentrations 5x as high as the scaffold. With the additional staples, a second annealing was carried out at a lower temperature, as the temperature increase could lead to the unfolding of already existing origami structures. According to Lee et al. the melting point of simple rectangular origamis lies around 55 °C [71], thus the annealing temperature of 40 °C was used with a linear ramp of 0.5 °C per minute. Figure 33 shows the results of this method. The arrays can already be observed, although the yield

is still low. The majority of the images are filled with thinner clusters, which were thought to be edge staples that, instead of hybridizing to the origamis, hybridized with each other to form clusters. This is undesired, given that it pollutes the images and decreases the available edge staples for the formation of arrays.

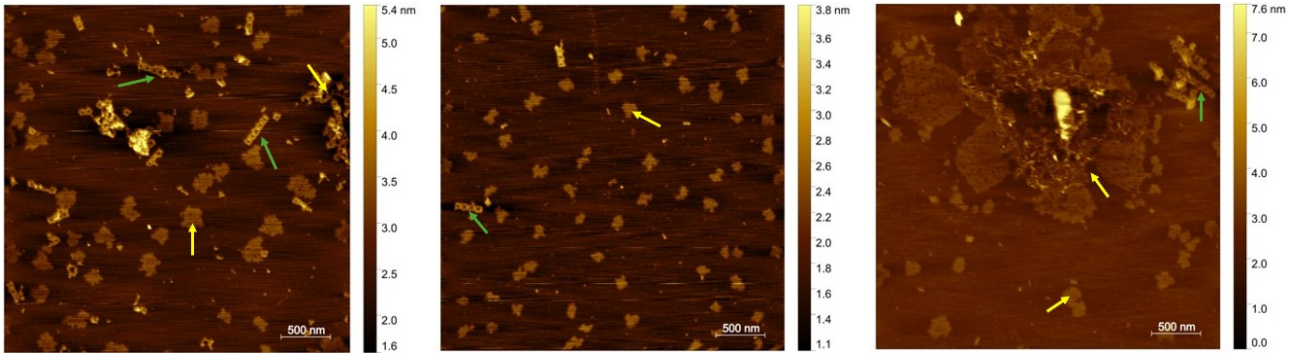

Figure 33: Array formation using all staples in one sample. Three representative areas are shown. Yellow arrows indicate the undesired products such as clusters or broken origamis, Green arrows indicate the arrays.

To get rid of the self-hybridization of edge staples, the two-pot assembly method was designed. The edge staples were added to the solution for the formation of single origamis. Two samples were made, one containing the even edge staples on the right and the odd edge staples from the left (looking from top to bottom). The other sample will contain the opposite, the even staples on the left and the odd staples on the right. Figure 34 schematically shows the edge interactions of the individual samples, and that of when adding them together. When producing these origamis, their right and left sides are not complementary anymore, such that they cannot hybridize with other origamis in the annealing procedure. When the two samples are annealed and filtered, they are put together, now the sides of the first and second batch are complementary, such that arrays can be formed without the pollution or interference of non-bonded edge staples. After this, the sample containing the two different origamis is annealed with a linear ramp of 0.5 $\frac{^{\circ}C}{min}$ starting at 40 degrees. Figure 34 shows the results of this procedure. It is clear that the clusters observed before are now gone, and the length and yield of the arrays increased.

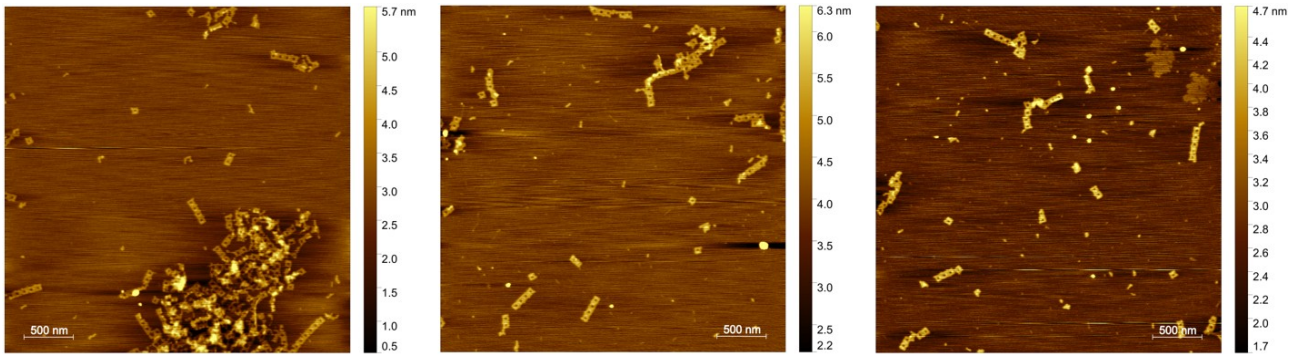

Figure 34: Array formation using two samples, each sample containing half of the edge staples.

To make sure the optimal annealing results are being used, annealing procedures with temperatures of 45, 50, and 55 °C were also prepared. The yield did not increase, and in some instances, they decreased the yield. Also, the duration of the annealing was altered to 24h and 72h, these parameter changes did not improve the performance.

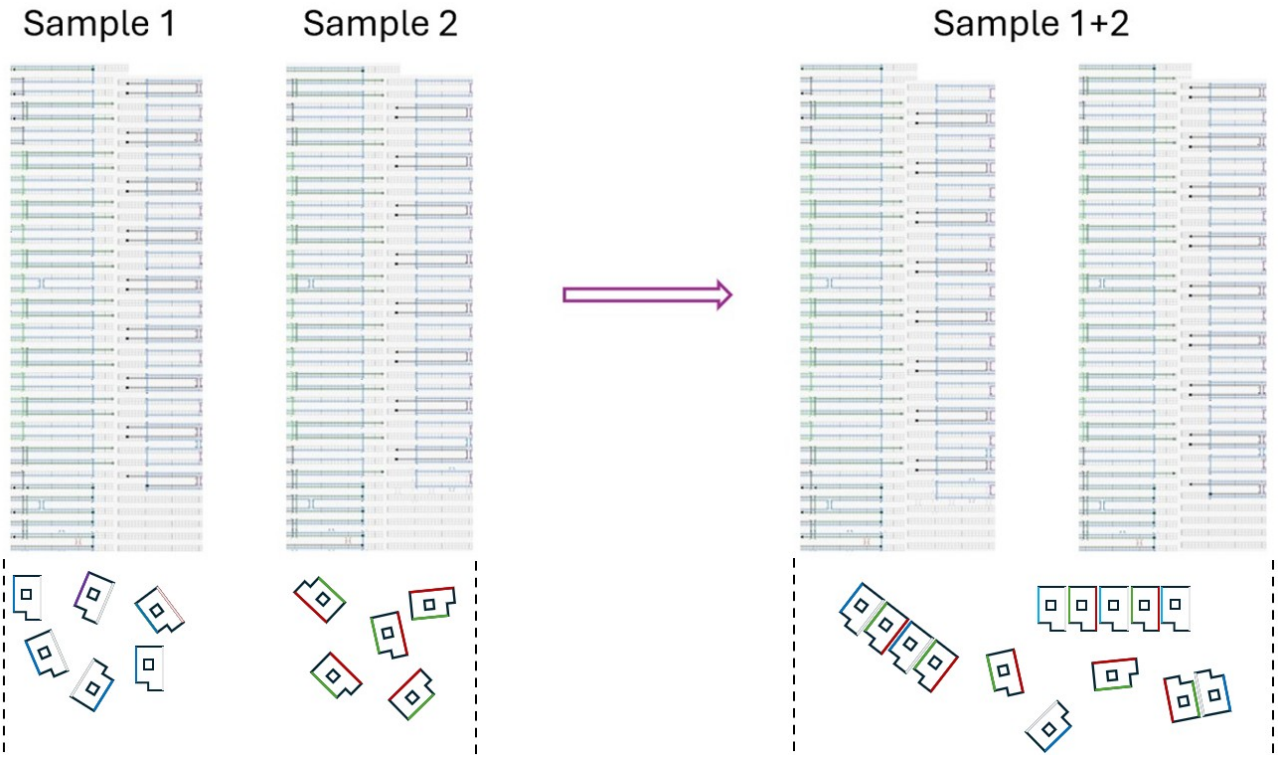

Figure 35: Visualization of the edge interaction between origamis. On the left, the two different samples are shown, focusing on the edges, here no interactions are possible due to the absence of the complementary staples for both sides. On the right, the edges of the combined samples are shown, showing that the edges of sample 1 are complementary to sample 2, and vice versa.

4.3.2 Arrays with docking staples

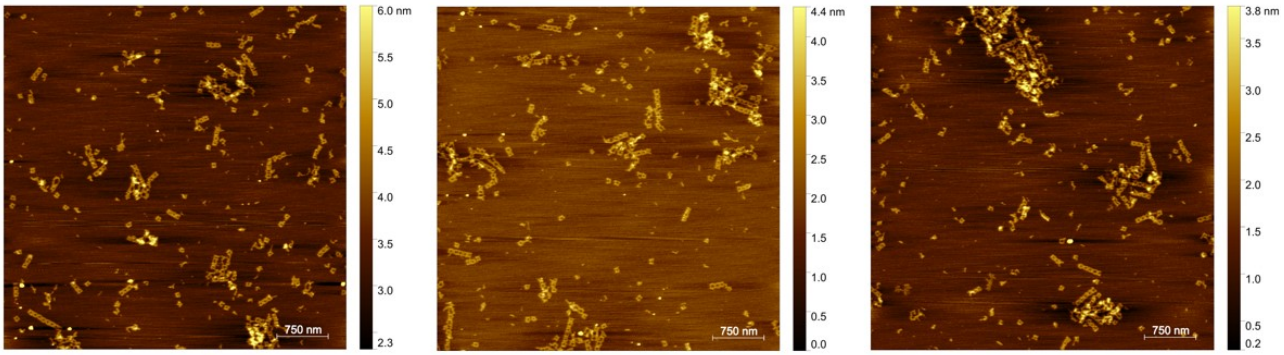

Figure 36: Array formation including docking staples using two samples, each sample containing half of the edge staples.

The production of origami arrays including the docking staples, is the same as for the arrays without docking staples. Figure 36 shows the results for the two pot assembly measurements including docking staples. It is clear that arrays are formed, but the array yield is lower, and upon close inspection, most of them are broken or misformed. This can again be a result of the lower yield of the single origamis and the large interfering ssDNA extensions. Figure 37 shows the size distribution of the arrays in a bar graph, here the percentage of origami arrays formed is shown for the sample with and without docking staples. Structures that were misformed or unrecognizable were not included in this count.

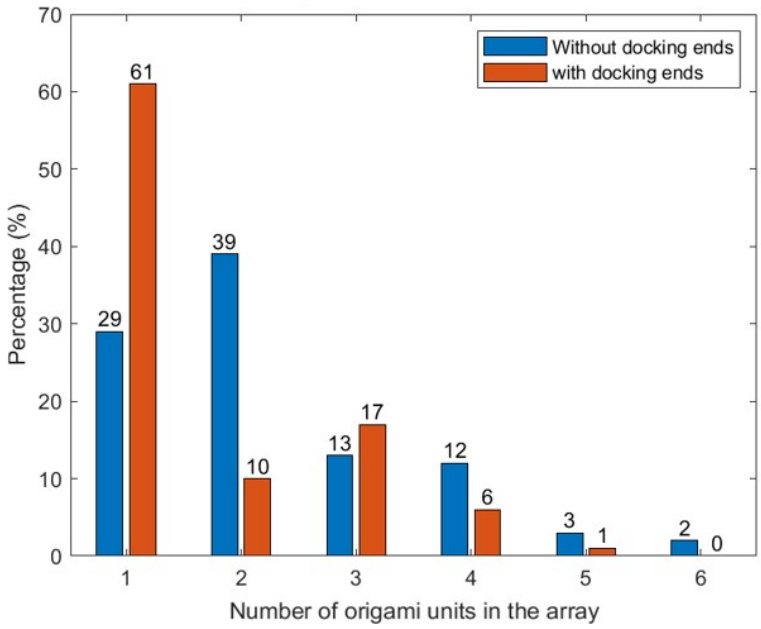

Figure 37: Overview of the size distribution of the arrays with and without docking staples.

4.4 hBN transfer and cleaning optimization

In this paragraph, the steps to optimization of the hBN exfoliation and transfer will be described. The goal is to get a high yield of large flakes on the glass with the lowest possible amount of glue contamination coming from the sticky tape. When the flakes or surrounding area is covered in glue, the possibility of origami binding decreases.

4.4.1 hBN yield on glass

To obtain the highest yield of flakes on the glass coverslips, 4 samples were made. The hotplate with controlled heating at 100 °C was used for glue evaporation and redistribution. Figure 38(a-d) shows images of the flake yield on the glass surface with: no heating, 1 minute heating, 2 minute heating, and 3 minute heating, respectively. It can be seen that the 1 minute heating already significantly increases the yield of hBN flakes on the glass. Further heating only leads to noticeable glue melting and contamination. In the rest of this paper, the procedure regarding Figure 38b will be maintained due to the flake yield/contamination ratio.

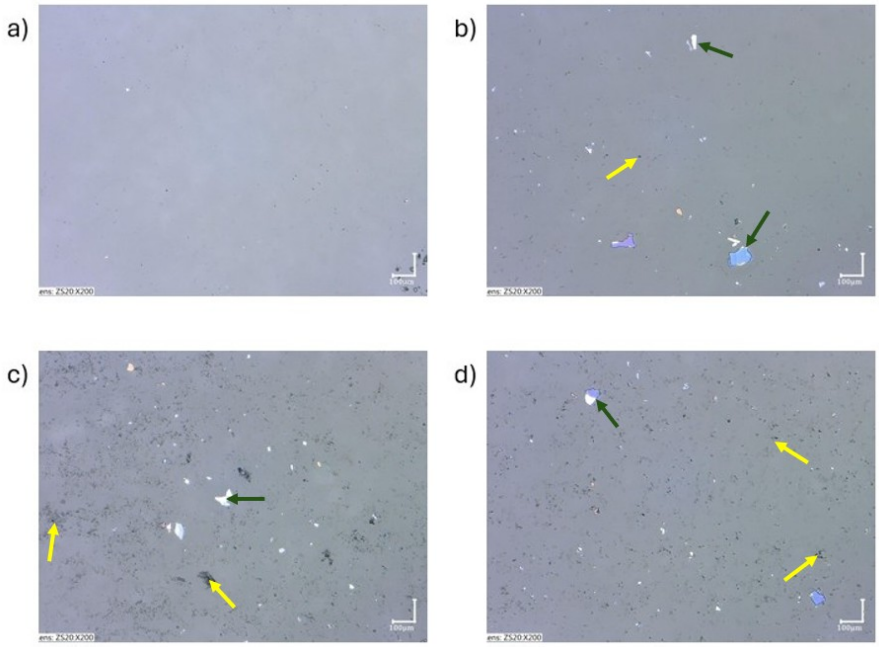

Figure 38: hBN flakes on glass using different heating procedures at 100 °C. a) no heating, b) 1 minute heating, c) 2 minute heating, d) 3 minute heating. Yellow arrows indicate undesirable structures such as dirt, green arrows indicate the hBN flakes.

4.4.2 Glue removal strategies

Now that the procedure for the production of a high flake density on glass is determined, the removal of the remaining glue needs to be discussed. Three glass samples containing hBN flakes were made using the same exfoliating procedure to guarantee reproducibility. Each sample underwent a heating process of 10, 20, and 30 minutes at 450 °C on the hotplate, the result of this measurement is shown in Figure 39(a-c), respectively. The results show that the removal of glue from the coverslip is approximately the same for all three experiments.

In this work, the AFM samples will be heated to 450 degrees for 10 minutes. However, this protocol will not be used for the fluorescence measurements, as when heated, melted glue residuals disturb the images. When heating the sample, a bright fluorescence signal covers the hBN flake and generates noise in the images.

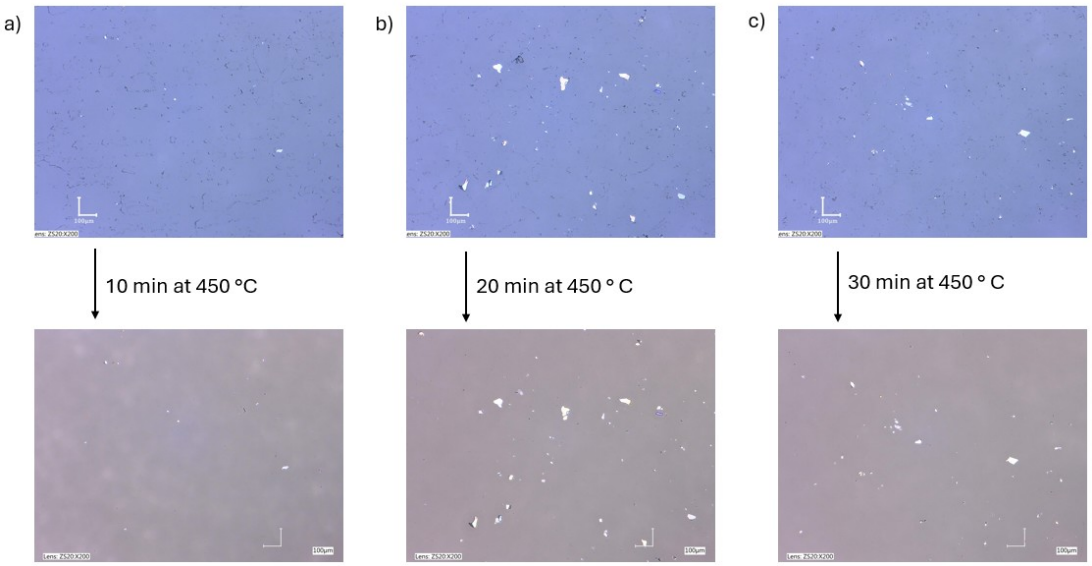

Figure 39: Different heating treatments for glue removal.

4.5 Origami structures on hBN surface

Before placing DNA structures and arrays on the hBN surface, the hBN flakes need to be characterized, Figure 40 shows three hBN flakes. Each flake has a force displacement image and a phase contrast image, each showing the surface topography. The phase contrast images give more insight into the topography due to their high contrast. The layered structure and sharp edges are also visible and are characteristic for hBN flakes, enabling them to be distinguished from dirt and other contaminants. From the AFM profiles can be seen that the hBN surface is atomically smooth and does not have any defects.

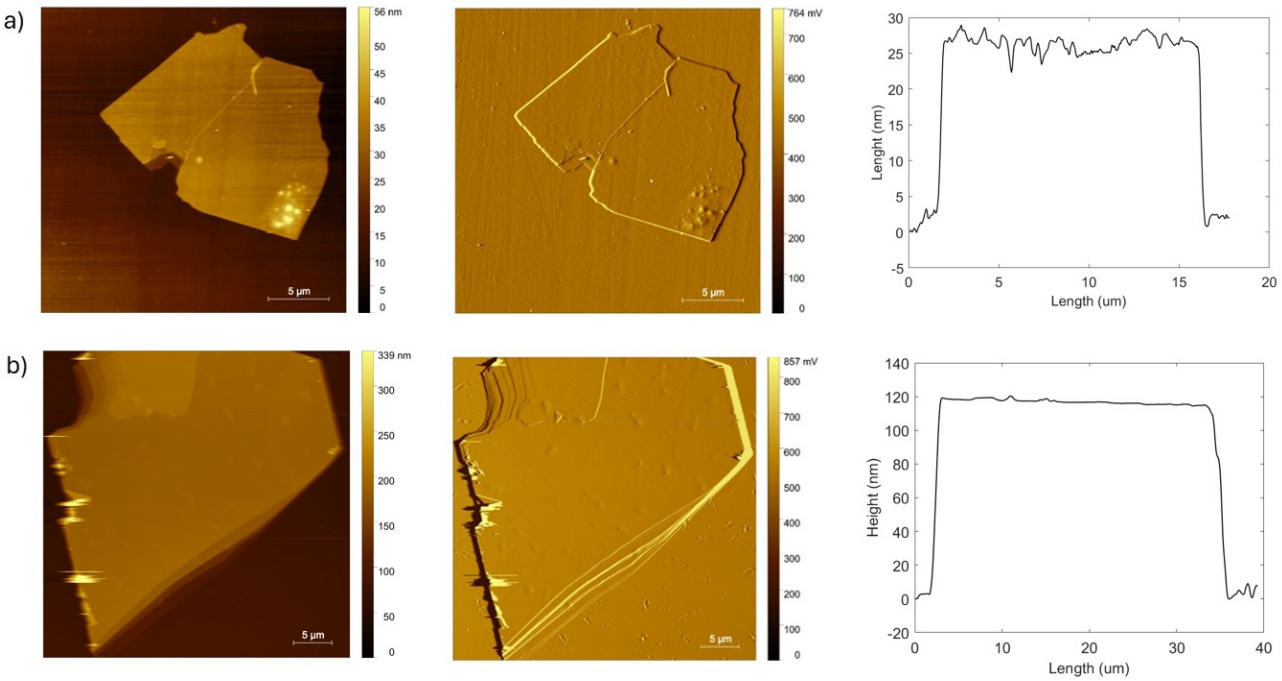

Figure 40: AFM images of hBN flakes on glass, showing the topography images in phase contrast(bottom) and force displacement(top). a) AFM images and height trace of hBN flake of approximately 25 nm in height. b) AFM images and height trace of hBN flake of approximately 120 nm in height.

4.5.1 Placement of single origamis on pristine hBN

Before measuring origami structures on the hBN surface, a reference measurement was done on hBN with only $MgCl^{2+}$ containing TAE buffer. With this, the risk of falsely identifying origami structures is limited, and a nice background signal can be obtained. Figure 41 shows the results of these measurements. Here, the bare hBN image shows a mostly flat surface with some contaminants, possibly glue contaminants due to the tape exfoliation procedure. However, the addition of the buffer to the hBN surface led to the formation of random structures. The sizes and heights of these structures come quite close to that of the origami structures, which makes identifying origamis on hBN a challenge. The change of the hBN surface can be attributed to hBN/Mg ion interactions or contaminant redepositioning.

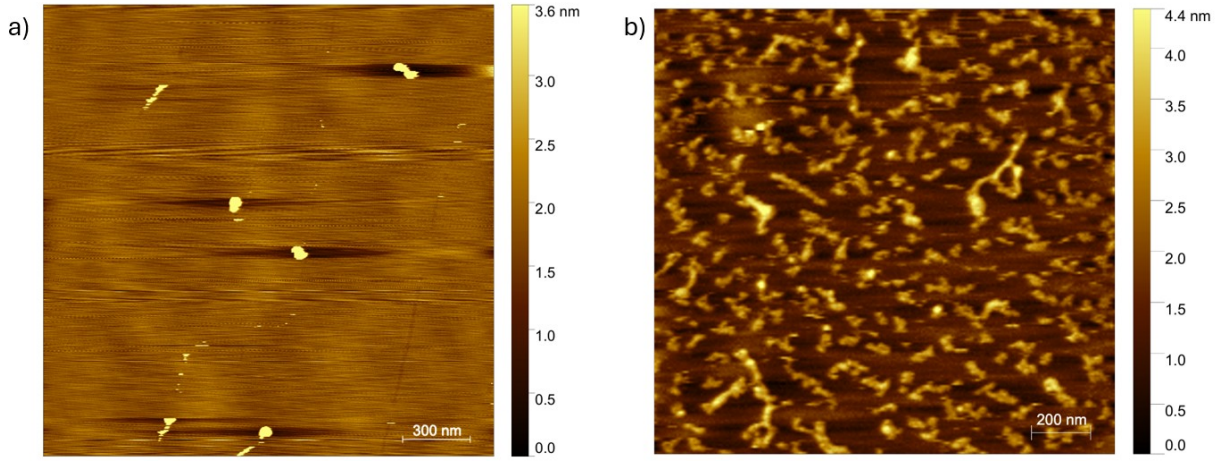

Figure 41: a) bare hBN, b) hBN with buffer solution, dried.

Now that background topography is known, origamis are placed on the hBN surface in the same concentration as on mica. One sample containing single origamis including the docking staples, and one excluding those were tested. The origami samples are deposited on the hBN-covered glass coverslip for 60 seconds, and washed 3x with 200 μL milli Q water. Results are shown in Figure 42. It becomes clear that for both samples, the individual origamis are hard to distinguish. In Figure 42a, it looks like the origami structures have been pulled apart, such that the individual structures are not recognizable. This can happen due to the attractive force of the hBN surface that disturbs the structural integrity of the origamis [72]. Some structures appear too have the correct size and shape of the origamis, but the image is too highly distorted to confirm this. Figure 42b shows a background that resembles that of Figure 42a, but on top of this, some origami structures can be identified in contrast to Figure 42a. Some origamis are well placed such that their orientation can be determined, and for each of those cases, the docking staples point away from the surface. This means that the immobilization of these origami structures is not facilitated by the docking staples. None of the origamis in these measurements was placed directly on the hBN surface, each visible origami was placed on the interference layer. The larger distance from the hBN surface could be the reason that the origamis were visible. Kabiri et al. positioned origami structures on graphene, and found that origamis experienced similar deformations and a similar background mesh structure to those imaged here [72].

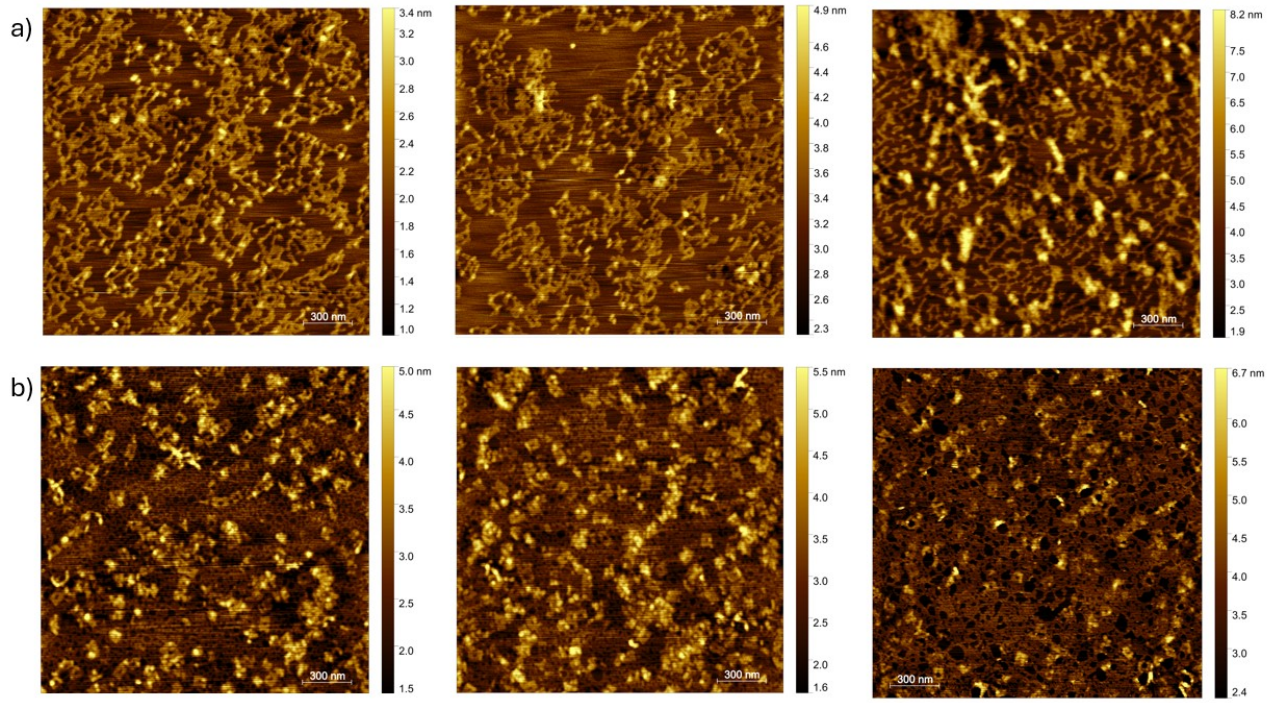

Figure 42: a) origamis excluding docking staples, b) origamis including docking staples.

To get a better look at the difference between the origamis placed on hBN and on mica, hBN flakes are placed on mica. By stamping flakes on mica, the origami structures can be placed on the mica/hBN surface for imaging. Figure 43 shows the results of this measurement. Due to the large height difference between the hBN and mica, both surfaces can not be placed into focus at the same time. Figure 43a focuses on the hBN surfaces, while Figure 43b focuses on the mica surface. The mesh covering the hBN flake and the structures on mica are clearly visible.

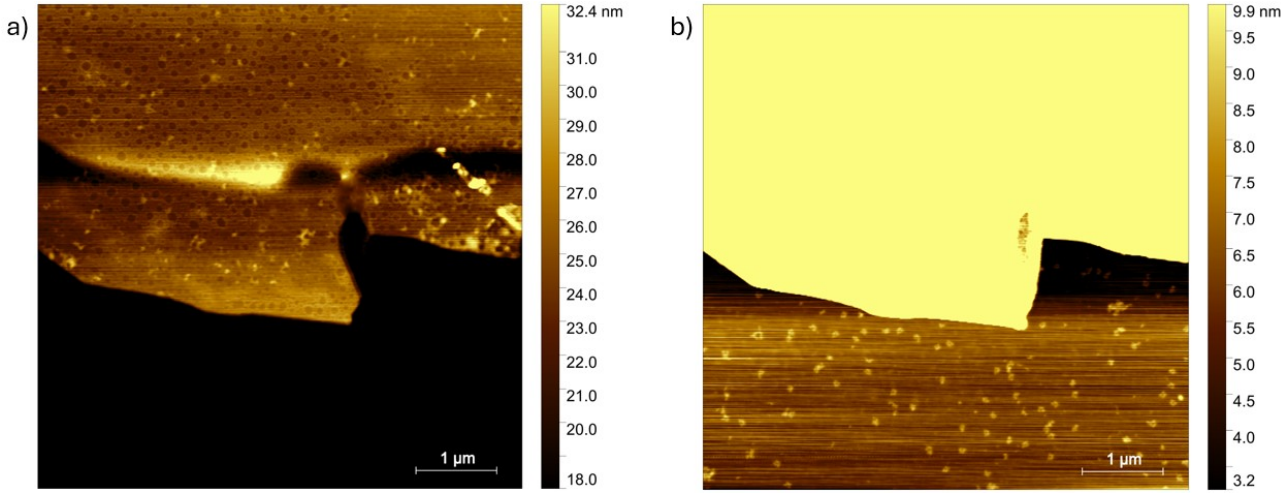

Figure 43: a) focusing on origamis on hBN, b) focusing on origamis on mica. The scale bar was changed for improved contrast.

4.5.2 Placement of single origamis on defective hBN

According to Shin et al. DNA has a higher potential of binding to defects in the hBN lattice [11]. To further investigate the binding affinity between the origami structures and defective hBN, origamis are placed on oxygen plasma-treated hBN. The hBN sample is bombarded with charged oxygen particles, when impacting onto the

hBN surface, pieces are etched away. When inducing defects in the hBN material, optical emitters arise from these defects and emit in different wavelengths, which can be a disadvantage when measuring the fluorescence signal from the DNA structures on hBN. An image of the bare defective hBN was taken, followed by an image of hBN with magnesium containing TAE buffer on the surface. Figure 44 shows these results. The bare hBN images without buffer shows a similar image as that of Figure 41, it also shows the same kind of contamination. The defects induced during the oxygen plasma treatment are too small to be seen with the AFM, meaning it could be expected that the images would look similar. Aside from some small contamination on Figure 41, the images look alike. This is a difference compared to the images, which were not oxygen plasma treated, meaning that when depositing buffer on defective hBN, the amount of random aggregates significantly decreases.

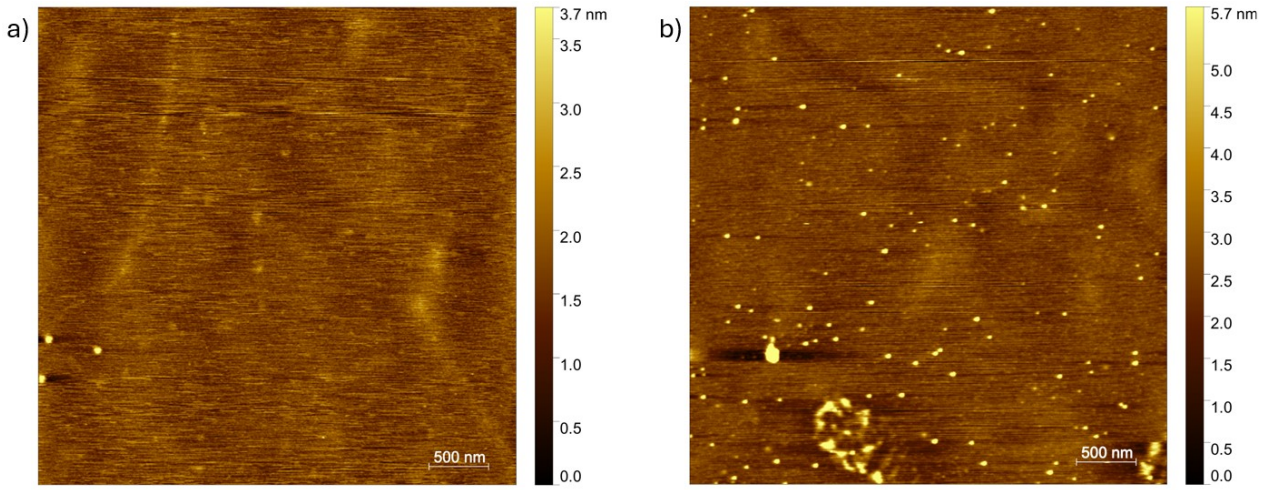

Figure 44: a) bare hBN 5 min oxygen plasma treated, b) hBN with MgCl containing buffer

Afterwards, single origami structures with docking staples were placed on the hBN surface. The result of this measurement is shown in Figure 45. The origamis were visible in the three images shown in Figure 45, when zooming in, the shape of the origamis becomes more visible. The mesh-like background that was visible in Figure 42 has cleared, showing only the origami structures and the hBN surface. This means that, in contrast to the pristine hBN, the defective hBN shows origamis that are on the hBN surface without any intermediate layer. These results demonstrate that it is possible to engineer the surface to enable the molecular switching mechanism. This relies on the different interactions between ssDNA and dsDNA on hBN, the actual hBN surface must be used, without an intermediate layer. Otherwise, the stacking interactions between the surface and DNA are believed not to be sufficient.

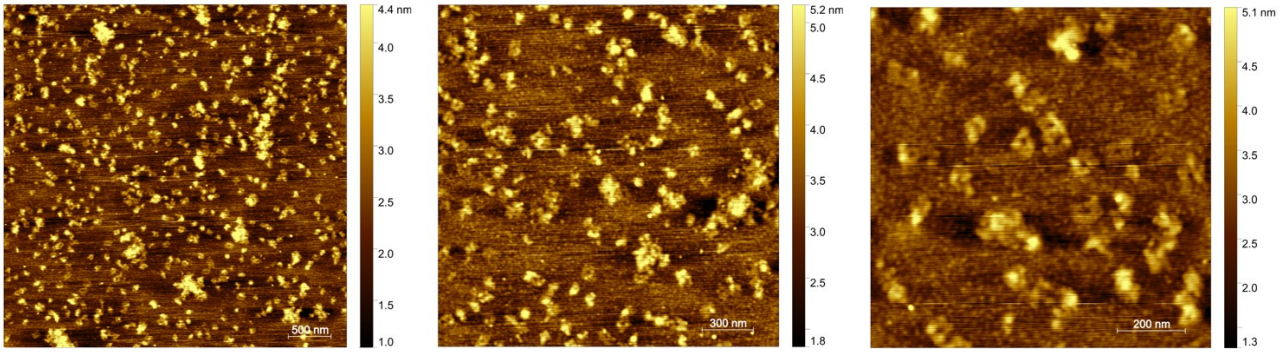

Figure 45: Images of different sizes and different flakes of docking origamis on hBN.

When looking at the results from Figure 45, several different shapes can be distinguished. Part of the origamis are so misformed that their geometry was not visible anymore, while others look very clear. Two different origami sets can be distinguished from each other: one was thicker and smaller, the other was thinner but longer. The thinner origami shows that the protruding docking staples point away from the surface, meaning that the sticking mechanism is not aided by the docking staples. The other origami was smaller and thicker.

This could be due to issues in the self-assembly procedure, but it could also indicate the origamis whose docking staples point towards the surface. The asymmetric feature of these origamis was not visible, and therefore, this assumption cannot be made with certainty. On five different substrates, ten origamis were measured, and their length and width (excluding their asymmetrical feature) are plotted in the graph in Figure 46. The yellow bars indicate the length of the origami, and the blue bars the width. It becomes clear that the width barely changes when positioning on different substrates or adding docking staples. But the length does significantly change, especially when origamis with docking staples were placed on hBN. An analysis of the height of the origamis on different substrates can be found in the supplementary information.

When looking at the changes in size, it becomes clear that this is perpendicular to the orientation of the double helices. Meaning the double helices do not elongate, but the distance between the helices changes. Kabiri et al. drew the same conclusion when placing origami structures on graphene [72].

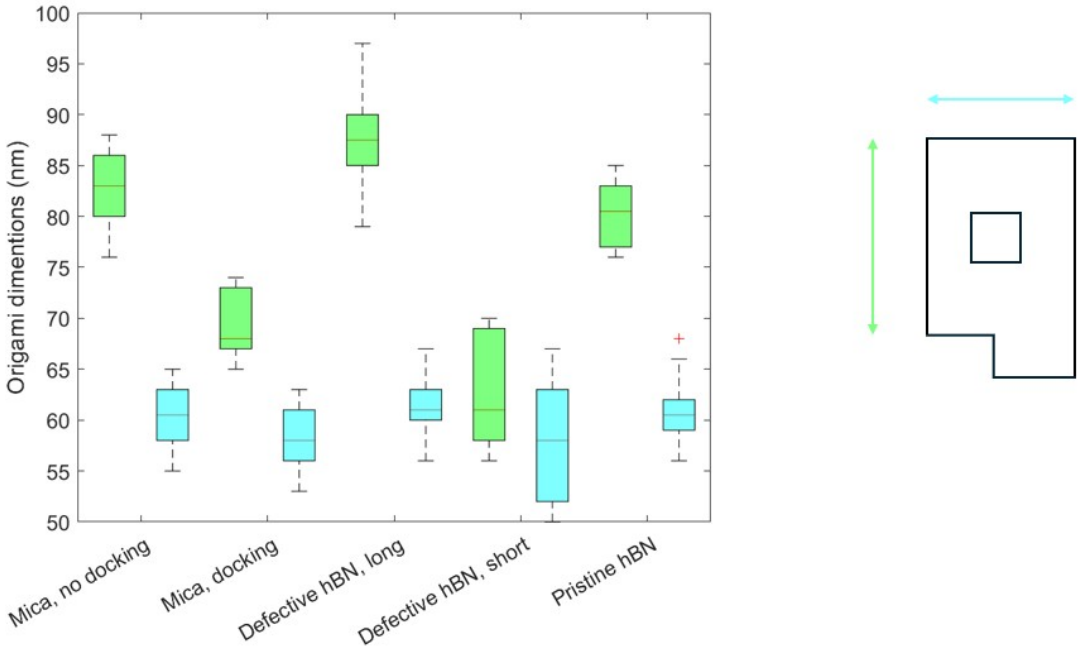

Figure 46: Overview origami dimensions on different substrates.

To make sure the origamis in Figure 45 are supported on a highly dense surface of DNA and buffer, the background was analyzed. By looking at the background roughness of 5 different samples, namely, mica(0.05 nm), pristine hBN(0.10 nm), defective hBN(0.12 nm), defective hBN with origamis(0.15 nm) and pristine hBN with origamis(0.47 nm). By tracing five, 5 μm lines through each image, the height trace along these lines was analyzed. By taking the absolute value of the height trace centered at 0, and integrating over the graph, the roughness of the surface was estimated. By plotting the results in a boxplot, the mean and the deviation were visualized. Figure 47 shows the data plot of these traces and the position of the traces in the images. As can be expected, apart from mica, the roughness of the pristine hBN is the lowest, followed by that of the oxygen plasma treated hBN. The roughness of the oxygen plasma treated hBN with origamis is slightly higher with a mean 0.016 nm above the defective hBN result. This higher number could be due to the AFM setup and tip properties, give that when the AFM travels over a relative high structure, a small area behind this structure is imaged slightly lower than it actually is. It could also be contamination due to broken pieces of origami that attached to the surface. When looking at the roughness result of the origamis on pristine hBN, it is a lot higher. Although the background of the defective hBN is slightly higher, no mesh-like layer is observed, and thus expect that the orgiamis are in direct contact with the hBN surface, and no intermediate layer is present between the origamis and hBN surface.

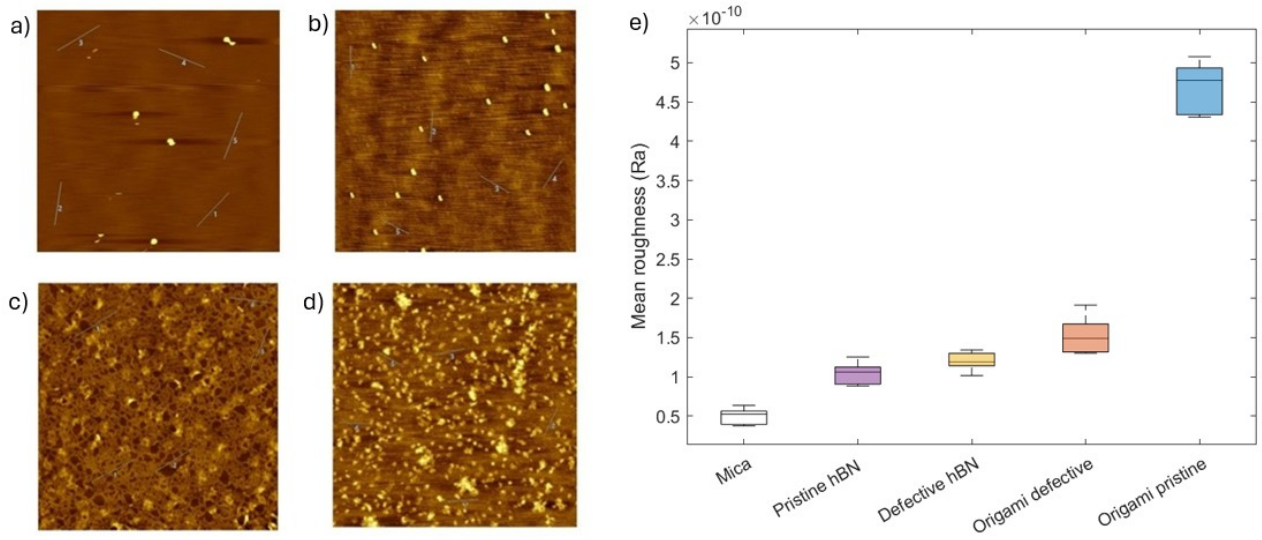

Figure 47: Roughness measurements of five different samples. a) pristine hBN, b) defective hBN, c) pristine hBN with origamis, d) defective hBN with origamis, e) Ra roughness plotted for each sample.

4.5.3 Placement of arrays on hBN

Given that origamis on hBN could potentially be intact, depending on the properties of the surface, as a first test, the origami arrays were placed on pristine hBN. Figure 48 shows the result of this measurement. The background looks similar to the placement of single origamis on pristine hBN, although the lines of the background mesh are thicker. When zooming in on those lines, it becomes clear that some single origamis are immobilized or aggregated there. This is analogous to the single origami measurement, i.e. no distinguishable origami structures, arrays, or singles, are immobilized directly on the hBN surface.

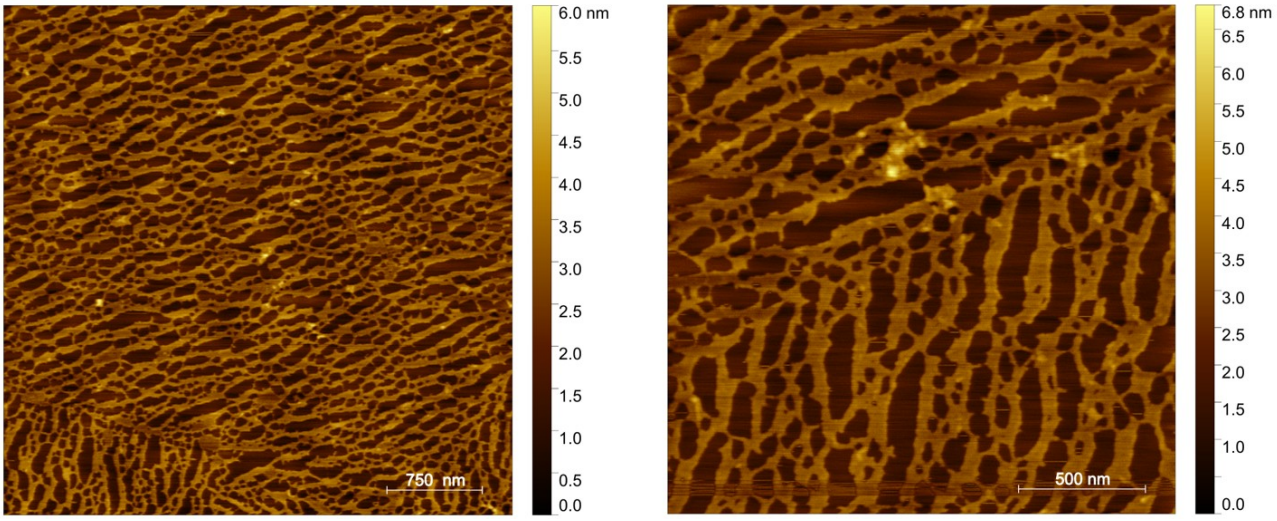

Figure 48: Two different magnification AFM images of origami arrays on pristine hBN.

To follow the procedure used for the single origamis, the arrays were placed on defective hBN. Figure 49a shows the results of this measurement. In some cases it is clear that the arrays are present but it is hard to distinguish the single origamis in the arrays, due to the fact that the origamis are misformed. Other arrays clearly show the geometry of the origamis in the arrays. The sample has been positioned on mica to make sure the arrays are formed, providing a control measurement of the orgiamis under idealized conditions.

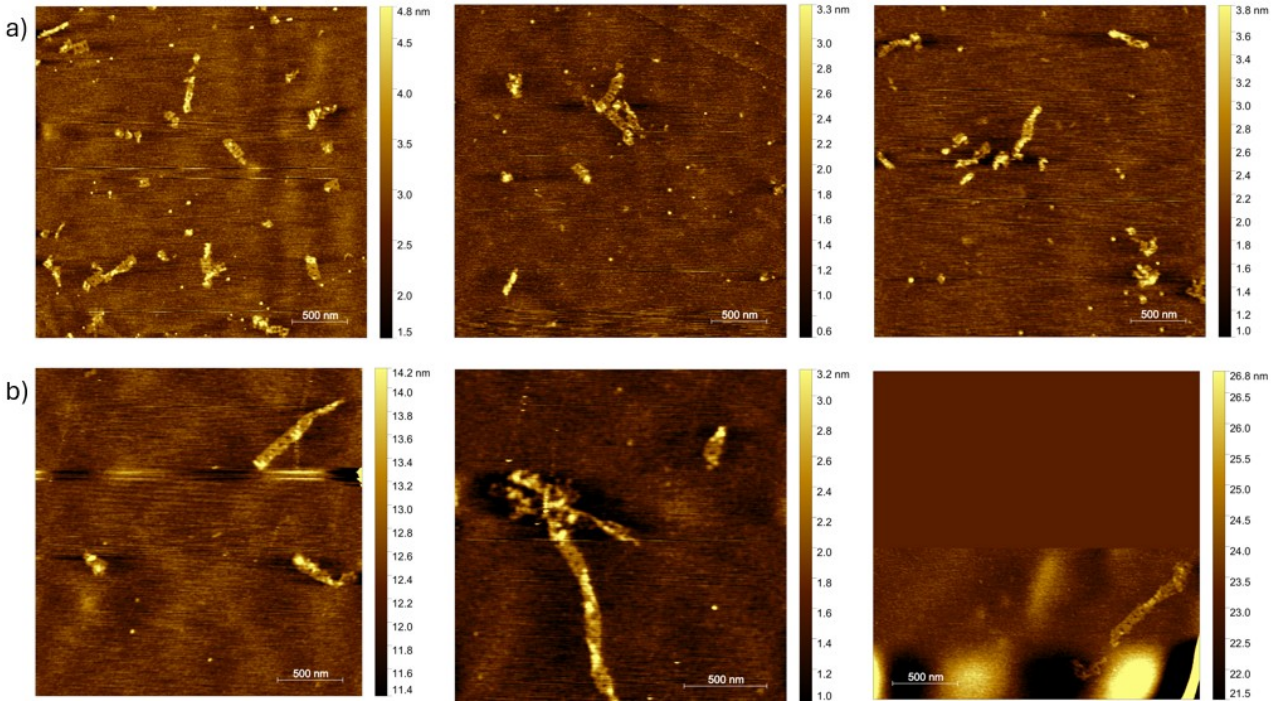

Figure 49: Arrays on hBN. a) arrays with 7-8 binding sites per interface, b) arrays with 17 binding sites per interface. The scale bar was changed for improved contrast.

The two pot assembly method that has been used to form the arrays has a downside, namely, the reduced number of binding sites per origami interface. Given that the hBN material tries to reduce the structural integrity of the origamis, the strength between the origamis becomes of great importance. Tikhomirov et al. produced origami arrays comprised of 64 tiles, after using specific placement with sticky ends, they inserted the remaining ssDNA strands to fortify the structures [16]. This method can be applied on the nanopore arrays in this paper. Previously, there are 7-8 binding sites per origami interface, by adding a 10 fold excess of the full set (34 staples) the origamis will have 17 binding sites per interface. The following method will be used to guarantee the hybridization of the staples. The annealing cycle used for creating the arrays after implementing the full set of edge staples, will be repeated. With this, the remaining 'empty' origami interfaces will be filled. The results of the immobilization of the stronger arrays on hBN is shown in Figure 49.

The images shown in Figure 49 show the same distinction between origami structures as Figure 42. Some origamis appear thinner and longer, more smeared out, other are smaller but thicker. The thin origami structures clearly show the correct geometry corresponding to the 'ideal' origami structures, in some instances the asymmetric feature is visible such that the orientation can be determined. Figure 49a shows the 'normal arrays', meaning the non reinforced arrays. Arrays of 2-4 origami units are visible. Upon close inspection of the arrays, a gap between the origami interfaces becomes visible, indicating the absence of remaining edge staples. Figure 49b shows the reinforced arrays, which are longer in comparison to the normal arrays, closer packed together and no gap can be seen in these arrays. It does show that when the arrays become longer they tend not to stay fully aligned along the surface, but bend after 3-4 origamis. The second image in Figure 49b clearly shows this property. This means that for creating longer arrays on hBN, different measures need to be taken to overcome bending with array length.

4.6 Fluorescent characterization of DNA origami arrays on hBN

To be able to distinguish the fluorescenct signal coming from the ATTO647N attached to the origamis, several reference measurements were done. Previously, arrays were placed on pristine and defective hBN, the defective hBN was used here, given that this material gave the best results. The fluorescent signal coming from defective hBN is mostly visible in green, the red fluorescenct signal is weaker and less dense than the green signal. This allows to resolve the ATTO647N fluorophores on hBN with high signal to noise ratio as their peak emission is at 664 nm.

After this initial check, two flakes were investigated. On the first flake, 5μL TAE buffer was deposited to make sure that potential emitters are not activated by buffer solution. After this, 5 μL the DNA origami arrays were placed on top of this buffer solution. Both images were images made in liquid. On the second flake, TAE buffer was also deposited, followed by 5μL of 10 pM concentration of ATTO647N. The ATTO647N is used as a reference regarding the fluorescenct signal coming from the origami structures. Knowing the intensity of this signal, the amount of fluorophores in the arrays can be estimated. Figure 50 shows the results of these measurements. From the images, it becomes clear that the background produced by possible defects and the buffer solution are minimal. When looking at the results of the arrays and ATTO647N, both show a good distribution across the surface.

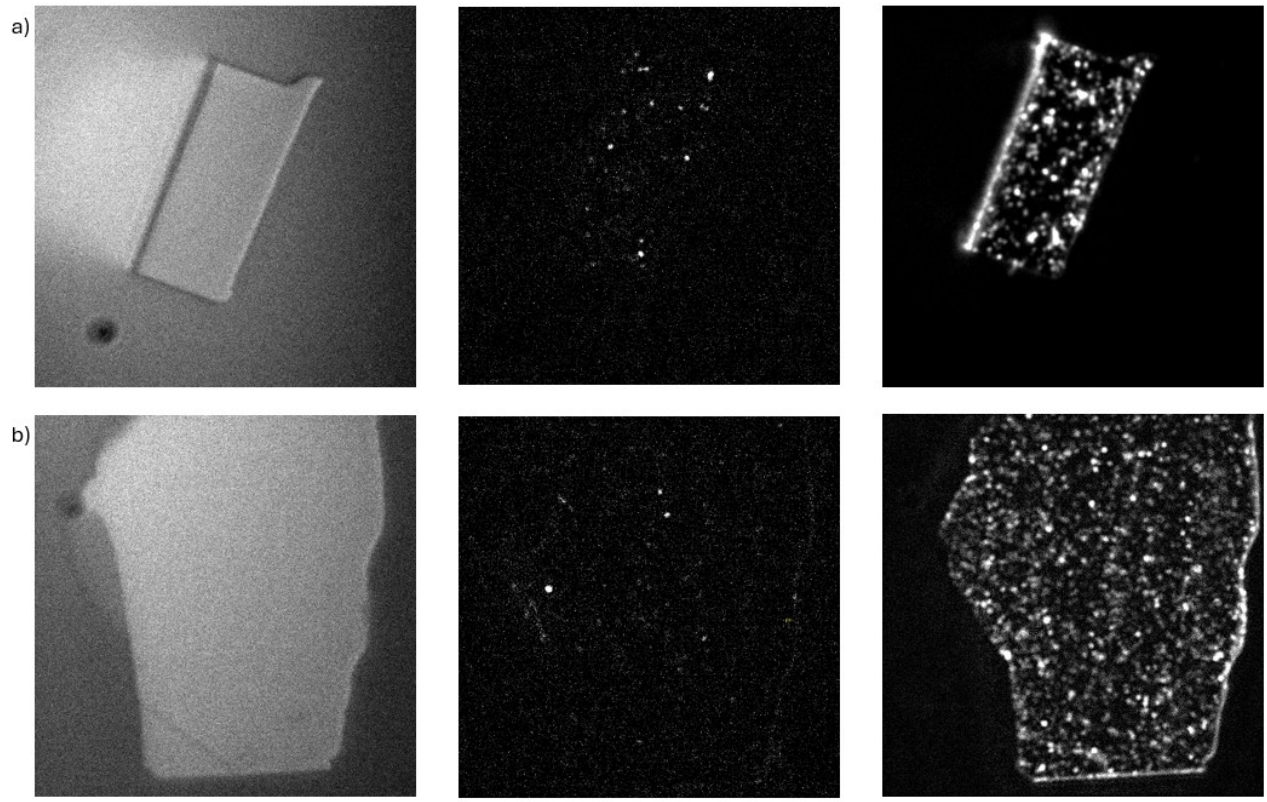

Figure 50: Fluorescence images acquired with the 125mW red laser. a) Flake illuminated with white light, only buffer illuminated in red, and arrays in red. b) Flake illuminated with white light, only buffer illuminated in red, and ATTO647N in red. The intensity in the images is not the same for better visibility of individual spots.

The optimal diffraction limit of optical microscopes is around 200-300 nm, meaning points can be distinguished from each other when they are at least 200-300 nm apart. Practically, the microscope used for these experiments has a diffraction limit closer to 450 nm. This is due to the 'non-ideal' conditions, only in a perfect environment, meaning an isolation stage without any tilt, the optimal wavelength, and the highest numerical aperture(NA), can this be achieved. Given that the origamis dimensions are 80x60 nm^2, and the arrays have a maximum of 4-5 consecutive origamis, an array would appear as a spot. When looking at the intensity of the spots, a difference should be noticed if the spot is comprised of multiple origamis carrying a fluorophore. By taking a video and tracking the spot intensity as a function of time, an estimate can be made regarding the number of origamis in that spot. This measurement would identify the number of fluorophores by revealing bleaching steps in the time trace. This approach is limited because while it could detect the number of fluorophores contained in a spot, it cannot give definite information about the conformation of the origamis. The bleaching steps of a well-formed array look the same as that of a broken-apart cluster with the same number of fluorophores.

Two videos were made, both lasting 1 minute, with a laser intensity of 125 mW. The first video was made of the flake containing arrays, and the second only of the ATTO647n dye. The average intensity over all spots in the video for the ATTO647N was 10.72, while that of the arrays was 67.54. Every origami, when correctly folded, has 2 fluorophores attached, meaning every signal coming from the array sample should be twice as high as that coming from the ATTO647N sample. According to the profiles, the average intensity is 6.3 times as high as that coming from the ATTO647N. This could indicate the presence of several origami arrays attached to the surface of the flake.

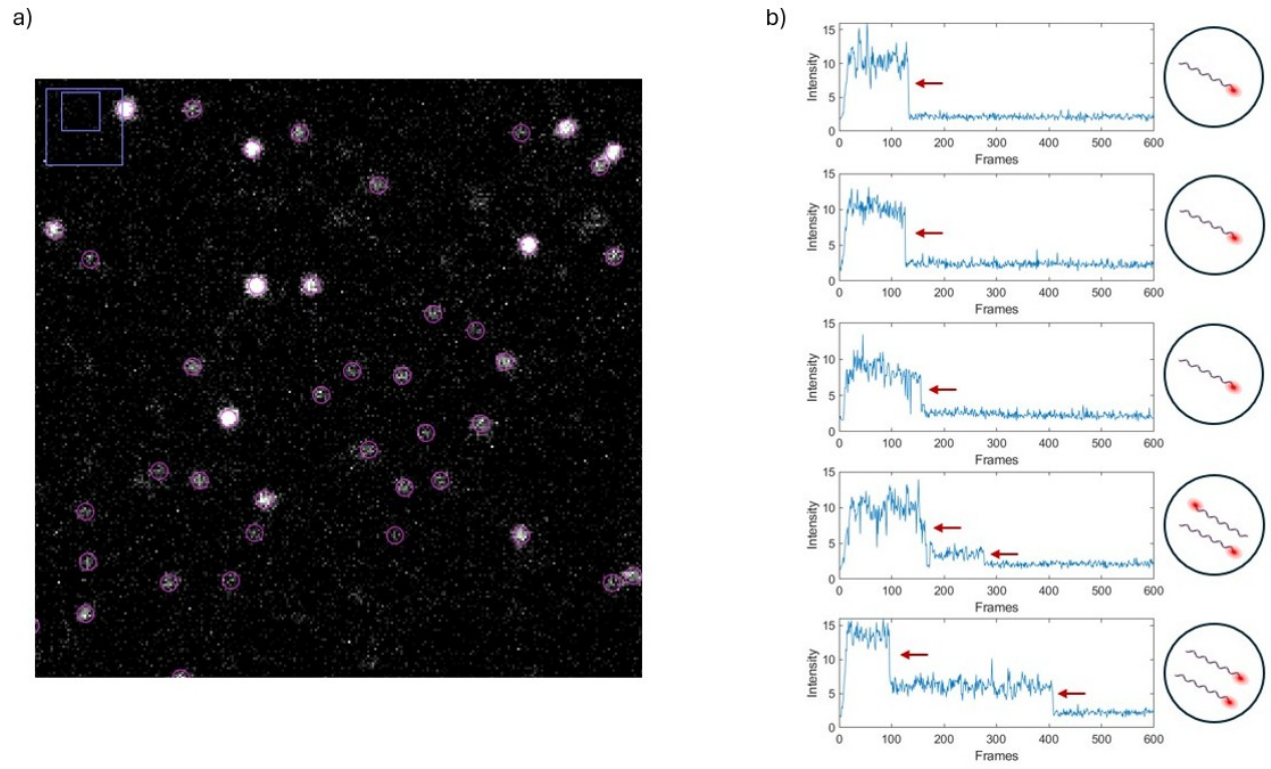

Figure 51: Intensity profiles ATTO647N sample. a) zoomin fluorescent signal containing distinct spots, image made with Fiji, b) intensity profiles of individual spots plotted as a function of time.

When looking at the individual intensity profiles as a function of time, the bleaching steps of individual fluorophores could be characterized. According to literature, when multiple fluorescent dyes are in close proximity, their signal is visualized as a single spot, their individual bleaching steps can be imaged [73]. Gür et al. shows this by combining three fluorescent dyes such that when imaged, only one single spot can be seen with the camera. When illuminating the sample with a laser, the three dyes did not bleach at the same simultaneously, but one at a time. When looking at the intensity trace over time, this resulted in a step response, where each step represents the bleaching of one dye.

With the method proposed above, the number of fluorescent dyes in a single spot can be estimated. To try and estimate the number of ATTO647N dyes present in the array sample, 10 intensity traces were taken from the ATTO647N and the array sample. Figure 51 shows five traces per sample, where each bleaching step is visualized with a red arrow, the remaining results are shown in the supplementary information. The ATTO647N sample clearly shows this step behavior, each step in intensity corresponds to one bleached dye. When multiple dyes are present, multiple intensity steps should be visible. Most spots only contain one dye, but Figure 51 also shows two traces that contain two dyes, here the two steps in intensity profile are visible.

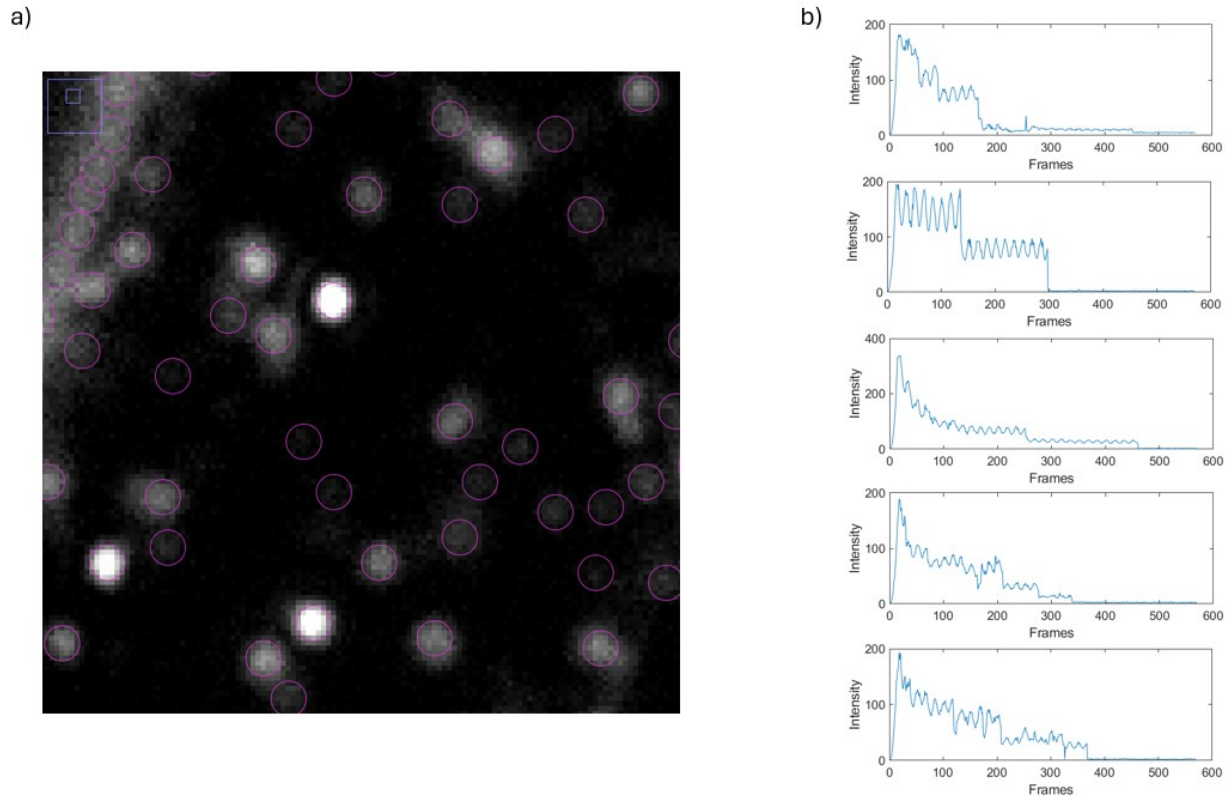

Figure 52: Intensity profiles array sample. a) zoomin fluorescent signal containing distinct spots, image made with Fiji, b) intensity profiles of individual spots plotted as a function of time.

Analyzing the array sample becomes more difficult. The intensity traces show higher intensities, as expected, but the bleaching steps do not correspond directly to that of the ATTO647N sample. Figure 52 shows the five intensity profiles as a function of time, the remaining profiles can be found in the supplementary information. The bleaching behavior does not show the clear, distinct platforms, as with the dyes, but shows a profile containing more noise. This can be seen by looking at the periodically repeating units present in the signal, when comparing this with the ATTO647N sample, this was not the case, and this also does not characterize the dye behavior correctly. It is challenging to extract a specific number of dyes present per spot, given that when the number of dyes doubles, the intensity does not necessarily also double. This can be seen when looking at the intensity profiles of Figure 51, single dyes overall bleach at an intensity of 10, while a spot with two dyes does that at 15. Due to the noisy profiles, the fluorophores also cannot be counted by looking at the bleaching steps. Due to the much higher intensity per spot in the array sample in comparison to that of ATTO647N, it can be noted that the chances of having detected arrays are present.

5 Conclusion

The purpose of this research, was to immobilize origami arrays on hBN, and characterize their structure and assembly with the AFM and fluorescence microscopy. The structure of choice was the single origami structures made by Wang et al. These orgiamis were assembled and placed on mica. For the close up images, QI mode was used, while for all other measurements, AC mode was used. AC mode gives a better resolution due to the extra information that is acquired by resonating the tip at its natural frequency. After the initial origamis made by Wang et al. were imaged on mica, the origami structure was modified to enable the following properties. 1) Imaging with fluorescence microscopy, by adding ssDNA handles for dyes, each origami was equipped with two binding sites. 2) Sticky end hybridization, the sides of the orgiamis were altered by inserting 17 extending sticky ends per origami interface. Each sticky end has a 6 bp overhang, that can hybridize with the 6 bp overhang on the other side of the origami. 3) immobilization on hBN, due to the non flat surface of the origamis, two locations that underwent the largest deformation were equipped with 6 protruding ssDNA 'docking staples'. These consist of 30 Adenine bases, and are meant to attach to the hBN material for immobilization. After self-assembling the origamis with the new docking staples, they appeared stable.

Knowing that the individual origamis with and without docking staples are stable, origami arrays can be formed. The first approach towards engineering the arrays was to combine all edge staples and origami staples, but this did not result in the formation of arrays. Then, by first creating origami structures without edge staples, and subsequently adding the edge staples, and annealing the sample again, we formed arrays. However, we saw that the concentration was very low, and the background was combined with clusters of self hybridized edge staples, which was not de desired outcome. To get rid of these clusters, we designed the 2 pot assembly method. With this, we made two samples, each with a different set of edge staples, such that within one sample, orgiamis could not hybridize with each other. After the formation of these single origami samples, they were mixed with equal volumes and annealed from 40 to 20 °C with a linear ramp of 0.5 °C per minute. This resulted in a higher yield of well formed origami arrays. When trying this same procedure with the origami with docking staples, the results were comparable.

Following the successful assembly and characterization of origamis on mica, we then proceed to the characterization on hBN. As a first measurement, we placed single origami structures with and without docking staples on pristine hBN. Interestingly, the results are strikingly different then those on mica. showing that the surface properties play a major role in the attachment of DNA origami structures. The result show a mesh-like structure directly on the hBN, probably comprised of broken origamis and salt. On top of this layer, origami structures were visible. The origamis including docking staples show a higher yield on this layer, but all recognizable origamis showed that the docking staples pointed away from the surface. This appears to indicate that their initial function to attach to the hBN via docking staples did not influence the immobilization, however, in future measurements only the origamis with docking staples will be used. When oxygen plasma treating the hBN surface for 5 minutes, the single origami structures adhered to the hBN surfaces without an interfacial layer. Two distinct origami structures could be imaged, one that was stretched and appeared thinner, and one that had slightly shrunk but appeared thicker. Both origami structures barely changed their width, but primarily changed their length. The thicker origami shrunk to 6.2 nm in length, and the thinner origami to 87.7 nm. This while the mean length of the origami structures with docking staples is 69.3 nm. From the results we can confirm the orientation of the stretched origami by identifying the asymmetrical feature, that shows the docking staples points away from the surface. The shrunk origamis are not as well formed, their asymmetrical feature is not visible, but it is possible that these are the origamis whose docking staples point towards the surface.

The next step involves placing the arrays on the hBN surface. As a preliminary check, we first placed the origami arrays on pristine hBN. This resulted in a comparable background mesh previously seen for the individual origami measurement, with occasionally an origami on top of this layer. Strikingly, when placing arrays on defective hBN, we identified arrays comprised of 3-4 origamis. Some arrays still appeared to be misformed when coming in contact with the surface, but in every measurements, we identified several arrays. The two pot assembly method used for producing the arrays, results in 7-8 binding sites per origami interface, while 17 contact points exist. Given the nature of the hBN surface to deform origami structures, the stronger the structures placed upon the surface, the more force required to break them. By inserting the full set of 34 edge staples, and annealing the sample again, the remaining 9-10 interfaces should be filled to generate a stronger array. When placing these structures on hBN, they resulted in closer packed, and longer arrays. The arrays did,

when surpassing 3-4 origamis, twist in such a way that the origami(s) in the twisted section are unrecognizable. The yield on the hBN flakes did decrease when working with stronger arrays, but their visibility increased due to their improved stability.

For the fluorescent characterization of origami arrays on hBN, we took several reference measurements. After finding a suitable flake, it was imaged with white, green and red light to obtain reference 'blank' samples. To ensure potential emitters are not caused by the buffer in the origami sample, we first imaged only the buffer solution on hBN. The number of emitters in red did not significantly increase when exposed to the buffer solution. Now the ATTO647N dye was placed on the flake, this showed a homogeneous distribution of emitting spots over the flake. These intensity patterns can be used as reference for the array measurement, since we expect individual fluorophores that are not tethered to a common substrate. When following the intensity trace of individual spots as a function of time, We identified bleaching steps of single and double fluorophores. The results of arrays on hBN also showed a homogeneous distribution over the surface, while the intensity in most spots was significantly higher then with just ATTO647N. This could indicate the formation of arrays, given the arrays are smaller then the diffraction limit, they would appear as spots. The average intensity over the flake with arrays was 6.3 times higher over to full length of the image, then that of the ATTO647N sample, indicating the possibility of the identification of arrays. When again following the intensity trace as a function of time, we identified several bleaching steps, indicating several origami structures present in the spot. Due to the large number of fluorophores per spot, the bleaching steps of all individual fluorophores could not be extracted. Also, due to the limitation of diffraction, no difference can be noticed between well formed arrays and clustered or destroyed origamis.

6 Future work

This research shows that it is possible to immobilize single and origami arrays on hBN. Which could eventually be used as a key component for biomarker detection for e.g. circulating tumor DNA sensing. Several subjects that could be investigated further, or subjects that were not fully exploited, are listed here for future work.

Switching mechanism

The switching mechanism introduced at the beginning of this research makes use of the different interaction principles of ssDNA and dsDNA on hBN. As a next step, an experiment could be designed that includes this switching mechanism inside the origami when placing it on hBN. This can provide evidence that the origamis are lying on the hBN surface, and not on an interference layer, provided the structure does not deform too much, such that the working principle is compromised. Figure ?? shows what could happen with the actuation mechanism when not directly placed on hBN, as was the case for pristine hBN. The working principle is based on the overlapping chemical structure of hBN and the DNA bases, which would only work when coming in direct contact with the hBN surface.

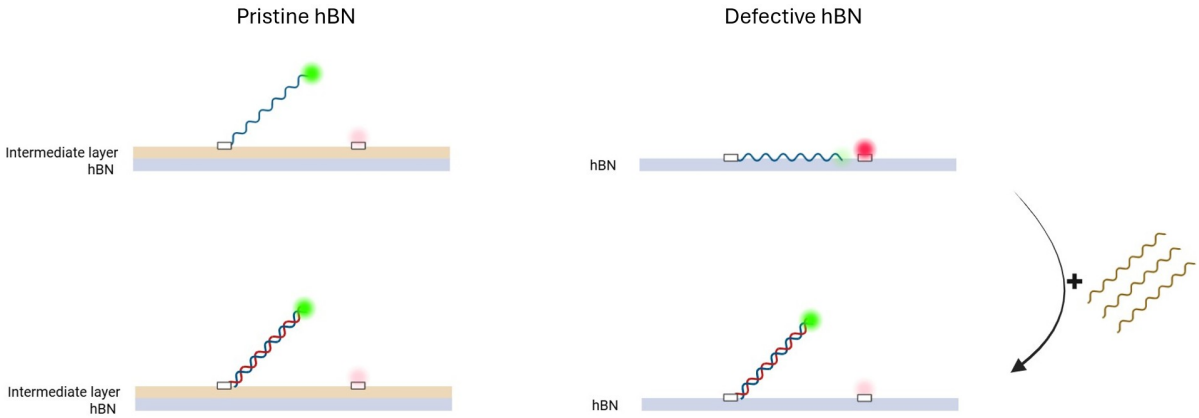

Figure 53: Visualization working principle of actuation mechanism on pristine and defective hBN.

Immobilization mechanism

Although it is demonstrated that origamis do attach to defective hBN, the principle behind this mechanism is still unclear. It would be interesting to know what exactly makes them adhere to the surface compared to pristine hBN. By creating measurements that include an origami structure with zero docking staples and one that has docking staples covering the entire surface, this mechanism can be better understood. By knowing exactly what mechanisms immobilize the structures the best, experiments can be altered to optimize the results.

Fluorescent characterization

The fluorescent measurements in this research were relatively short. This is mainly due to the lack of time. By using super-resolution methods, the arrays on the hBN surface can be individually visualized. This is a first step towards creating a reliable output for the proposed preliminary cancer detector. Two well-known methods could be utilized for this work, DNA-PAINT(DNA point accumulation for imaging in nanoscale topography) and SOFI(super-resolution optical fluctuation imaging). Both methods take multiple images of a dynamic sample with blinking dyes. By overlapping all images of the sample, an image is constructed, resolving distances below the diffraction limit.

References

[1] A. Pulumati, A. Pulumati, B. S. Dwarakanath, A. Verma, and R. V. L. Papineni, "Technological advancements in cancer diagnostics: Improvements and limitations," *Cancer Reports*, vol. 6, 2 2023.

[2] F. Bray, M. Laversanne, H. Sung, J. Ferlay, R. L. Siegel, I. Soerjomataram, and A. Jemal, "Global cancer statistics 2022: Globocan estimates of incidence and mortality worldwide for 36 cancers in 185 countries," *CA: A Cancer Journal for Clinicians*, vol. 74, pp. 229–263, 5 2024.

[3] J. D. Merker, G. R. Oxnard, C. Compton, M. Diehn, P. Hurley, A. J. Lazar, N. Lindeman, C. M. Lockwood, A. J. Rai, R. L. Schilsky, A. M. Tsimberidou, P. Vasalos, B. L. Billman, T. K. Oliver, S. S. Bruinooge, D. F. Hayes, and N. C. Turner, "Circulating tumor dna analysis in patients with cancer: American society of clinical oncology and college of american pathologists joint review," *Journal of Clinical Oncology*, vol. 36, pp. 1631–1641, 6 2018.

[4] N. Akkilic, S. Geschwindner, and F. Höök, "Single-molecule biosensors: Recent advances and applications," *Biosensors and Bioelectronics*, vol. 151, p. 111944, 3 2020.

[5] A. Koyun, E. Ahlatcolu, and Y. Koca, *Biosensors and Their Principles.* InTech, 6 2012.

[6] X. Cai, Y. Luo, B. Liu, and H. M. Cheng, "Preparation of 2d material dispersions and their applications," 2018.

[7] Y. Liu, X. Duan, H. J. Shin, S. Park, Y. Huang, and X. Duan, "Promises and prospects of two-dimensional transistors," 2021.

[8] Q. Jiang, S. Liu, J. Liu, Z. Wang, and B. Ding, "Rationally designed dna-origami nanomaterials for drug delivery in vivo," *Advanced Materials*, vol. 31, 11 2019.

[9] K. Lymperopoulos, R. Crawford, J. P. Torella, M. Heilemann, L. C. Hwang, S. J. Holden, and A. N. Kapanidis, "Single-molecule dna biosensors for protein and ligand detection," *Angewandte Chemie - International Edition*, vol. 49, 2010.

[10] C. Su, E. Janzen, M. He, C. Li, A. Zettl, J. D. Caldwell, J. H. Edgar, and I. Aharonovich, "Fundamentals and emerging optical applications of hexagonal boron nitride: a tutorial," *Advances in Optics and Photonics*, vol. 16, no. 2, pp. 229–346, 2024.

[11] D. H. Shin, S. H. Kim, K. Coshic, K. Watanabe, T. Taniguchi, G. Verbiest, S. Caneva, A. Aksimentiev, P. G. Steeneken, and C. Joo, "Diffusion of dna on atomically flat 2d material surfaces," *bioRxiv*, 2023.

[12] Q. Lin, X. Zou, G. Zhou, R. Liu, J. Wu, J. Li, and W. Duan, "Adsorption of dna/rna nucleobases on hexagonal boron nitride sheet: An ab initio study," *Physical Chemistry Chemical Physics*, vol. 13, 2011.

[13] P. W. Rothemund, "Folding dna to create nanoscale shapes and patterns," 2006.

[14] B. Saccà and C. M. Niemeyer, "Dna origami: The art of folding dna," 2012.

[15] E. Penzo, R. Wang, M. Palma, and S. J. Wind, "Selective placement of dna origami on substrates patterned by nanoimprint lithography," *Journal of Vacuum Science Technology B, Nanotechnology and Microelectronics: Materials, Processing, Measurement, and Phenomena*, vol. 29, 11 2011.

[16] G. Tikhomirov, P. Petersen, and L. Qian, "Fractal assembly of micrometre-scale dna origami arrays with arbitrary patterns," *Nature*, vol. 552, pp. 67–71, 12 2017.

[17] K. Ebel, "Quantification of low-energy electron induced single and double strand breaks in well-defined dna sequences using dna origami nanostructures," doctoralthesis, Universität Potsdam, 2021.

[18] J. D. Watson and F. H. Crick, "Molecular structure of nucleic acids: A structure for deoxyribose nucleic acid," *Nature*, vol. 171, 1953.

[19] L. J. e. a. Alberts B, Johnson A, *Molecular Biology of the Cell. 4th edition.* Garland science, 2002.

[20] A. Kuzyk, R. Schreiber, Z. Fan, G. Pardatscher, E.-M. Roller, A. Högele, F. C. Simmel, A. O. Govorov, and T. Liedl, "Dna-based self-assembly of chiral plasmonic nanostructures with tailored optical response," *Nature*, vol. 483, no. 7389, pp. 311–314, 2012.

[21] D. Renneberg and C. J. Leumann, "Watson-crick base-pairing properties of tricyclo-dna," *Journal of the American Chemical Society*, vol. 124, 2002.

[22] H. Said, V. J. Schüller, F. J. Eber, C. Wege, T. Liedl, and C. Richert, "M1.3 – a small scaffold for dna origami ," *Nanoscale*, vol. 5, pp. 284–290, 2013.

[23] T. R. Shepherd, R. R. Du, H. Huang, E. C. Wamhoff, and M. Bathe, "Bioproduction of pure, kilobase-scale single-stranded dna," *Scientific Reports*, vol. 9, 2019.

[24] A. R. Chandrasekaran, M. Pushpanathan, and K. Halvorsen, "Evolution of dna origami scaffolds," *Materials Letters*, vol. 170, pp. 221–224, 5 2016.

[25] X. Chen, Q. Wang, J. Peng, Q. Long, H. Yu, and Z. Li, "Self-assembly of large dna origami with custom-designed scaffolds," *ACS Applied Materials Interfaces*, vol. 10, pp. 24 344–24 348, 7 2018, about making longer scaffold ssDNA using gibson assembly.

[26] S. M. Douglas, A. H. Marblestone, S. Teerapittayanon, A. Vazquez, G. M. Church, and W. M. Shih, "Rapid prototyping of 3d dna-origami shapes with cadnano," *Nucleic acids research*, vol. 37, no. 15, pp. 5001–5006, 2009.

[27] "How we make dna origami," *ChemBioChem*, vol. 18, pp. 1873–1885, 10 2017.

[28] Y. Hu, Z. Chen, Z. Hou, M. Li, B. Ma, X. Luo, and X. Xue, "Influence of magnesium ions on the preparation and storage of dna tetrahedrons in micromolar ranges," *Molecules*, vol. 24, p. 2091, 6 2019.

[29] K. Serec, S. D. Babić, R. Podgornik, and S. Tomić, "Effect of magnesium ions on the structure of DNA thin films: an infrared spectroscopy study," *Nucleic Acids Research*, vol. 44, no. 17, pp. 8456–8464, 08 2016. [Online]. Available: https://doi.org/10.1093/nar/gkw696

[30] V. Linko and A. Keller, "Stability of dna origami nanostructures in physiological media: The role of molecular interactions," *Small*, vol. 19, 8 2023.

[31] C. Kielar, S. Ramakrishnan, S. Fricke, G. Grundmeier, and A. Keller, "Dynamics of dna origami lattice formation at solid–liquid interfaces," *ACS Applied Materials Interfaces*, vol. 10, pp. 44 844–44 853, 12 2018.

[32] P. Wang, T. A. Meyer, V. Pan, P. K. Dutta, and Y. Ke, "The beauty and utility of dna origami," 2017.

[33] P. Zhan, A. Peil, Q. Jiang, D. Wang, S. Mousavi, Q. Xiong, Q. Shen, Y. Shang, B. Ding, C. Lin, Y. Ke, and N. Liu, "Recent advances in dna origami-engineered nanomaterials and applications," *Chemical Reviews*, vol. 123, pp. 3976–4050, 4 2023.

[34] A. Kuzuya, R. Watanabe, Y. Yamanaka, T. Tamaki, M. Kaino, and Y. Ohya, "Nanomechanical dna origami ph sensors," *Sensors*, vol. 14, pp. 19 329–19 335, 10 2014.

[35] F. N. Gür, S. Kempter, F. Schueder, C. Sikeler, M. J. Urban, R. Jungmann, P. C. Nickels, and T. Liedl, "Double- to single-strand transition induces forces and motion in dna origami nanostructures," *Advanced Materials*, vol. 33, 2021.

[36] D. Y. Zhang and G. Seelig, "Dynamic dna nanotechnology using strand-displacement reactions," *Nature Chemistry*, vol. 3, 2011.

[37] S. Wang, Z. Zhou, N. Ma, S. Yang, K. Li, C. Teng, Y. Ke, and Y. Tian, "Dna origami-enabled biosensors," *Sensors*, vol. 20, no. 23, p. 6899, 2020.

[38] Y. Qin, W. Yang, H. Chu, Y. Li, S. Cai, H. Yu, and L. Liu, "Atomic force microscopy for tumor research at cell and molecule levels," *Microscopy and Microanalysis*, vol. 28, pp. 585–602, 6 2022.

[39] Y. Ke, S. Lindsay, Y. Chang, Y. Liu, and H. Yan, "Self-assembled water-soluble nucleic acid probe tiles for label-free rna hybridization assays," *Science*, vol. 319, no. 5860, pp. 180–183, 2008.

[40] D. El Arawi, M. Cardoso Dos Santos, C. Vézy, and R. Jaffiol, "Incidence angle calibration for prismless total internal reflection fluorescence microscopy," *Optics Letters*, vol. 44, no. 7, pp. 1710–1713, 2019.

[41] K. Dreier, "What are fluorescence and phosphorescence?" *ChemViews*, 2017.

[42] K. Jahnke, H. Grubmüller, M. Igaev, and K. Göpfrich, "Choice of fluorophore affects dynamic dna nanostructures," *Nucleic Acids Research*, vol. 49, pp. 4186–4195, 4 2021.

[43] Q. Jiang, X. Xu, P.-A. Yin, K. Ma, Y. Zhen, P. Duan, Q. Peng, W.-Q. Chen, and B. Ding, "Circularly polarized luminescence of achiral cyanine molecules assembled on dna templates," *Journal of the American Chemical Society*, vol. 141, pp. 9490–9494, 6 2019.

[44] N. Sarfraz and I. Khan, "Plasmonic gold nanoparticles (aunps): Properties, synthesis and their advanced energy, environmental and biomedical applications," *Chemistry – An Asian Journal*, vol. 16, pp. 720–742, 4 2021.

[45] S. Link and M. A. El-Sayed, "Size and temperature dependence of the plasmon absorption of colloidal gold nanoparticles," *The Journal of Physical Chemistry B*, vol. 103, pp. 4212–4217, 5 1999.

[46] "Construction of a gold nanoparticle-based single-molecule biosensor for simple and sensitive detection of argonaute 2 activity," *Journal of Materials Chemistry B*, vol. 10, pp. 5594–5601, 2022.

[47] C. Steinhauer, R. Jungmann, T. Sobey, F. Simmel, and P. Tinnefeld, "Dna origami as a nanoscopic ruler for super-resolution microscopy," *Angewandte Chemie International Edition*, vol. 48, pp. 8870–8873, 11 2009.

[48] R. B. Sekar and A. Periasamy, "Fluorescence resonance energy transfer (fret) microscopy imaging of live cell protein localizations," 2003.

[49] A. Megalathan, K. M. Wijesinghe, and S. Dhakal, "Single-molecule fret-based dynamic dna sensor," *ACS Sensors*, vol. 6, 2021.

[50] S.-Y. Ding, E.-M. You, Z.-Q. Tian, and M. Moskovits, "Electromagnetic theories of surface-enhanced raman spectroscopy," *Chemical Society Reviews*, vol. 46, no. 13, pp. 4042–4076, 2017.

[51] J. Prinz, B. Schreiber, L. Olejko, J. Oertel, J. Rackwitz, A. Keller, and I. Bald, "Dna origami substrates for highly sensitive surface-enhanced raman scattering," *Journal of Physical Chemistry Letters*, vol. 4, 2013.

[52] R. J. Kershner, L. D. Bozano, C. M. Micheel, A. M. Hung, A. R. Fornof, J. N. Cha, C. T. Rettner, M. Bersani, J. Frommer, P. W. K. Rothemund, and G. M. Wallraff, "Placement and orientation of individual dna shapes on lithographically patterned surfaces," *Nature Nanotechnology*, vol. 4, pp. 557–561, 9 2009.

[53] W. Liu, H. Zhong, R. Wang, and N. C. Seeman, "Crystalline two-dimensional dna-origami arrays," *Angewandte Chemie - International Edition*, vol. 50, 2011.

[54] G. Tikhomirov, P. Petersen, and L. Qian, "Triangular dna origami tilings," *Journal of the American Chemical Society*, vol. 140, 2018.

[55] N. Avakyan, J. W. Conway, and H. F. Sleiman, "Long-range ordering of blunt-ended dna tiles on supported lipid bilayers," *Journal of the American Chemical Society*, vol. 139, 2017.

[56] A. AghebatRafat, T. Pirzer, M. B. Scheible, A. Kostina, and F. C. Simmel, "Surface-assisted large-scale ordering of dna origami tiles," *Angewandte Chemie International Edition*, vol. 53, pp. 7665–7668, 7 2014.

[57] S. A. Coulocheri, D. G. Pigis, K. A. Papavassiliou, and A. G. Papavassiliou, "Hydrogen bonds in protein–dna complexes: Where geometry meets plasticity," *Biochimie*, vol. 89, pp. 1291–1303, 11 2007.

[58] X. Wang, H. Jun, and M. Bathe, "Programming 2d supramolecular assemblies with wireframe dna origami," *Journal of the American Chemical Society*, vol. 144, pp. 4403–4409, 3 2022.

[59] P. Zhu and H. G. Craighead, "Zero-mode waveguides for single-molecule analysis," *Annual Review of Biophysics*, vol. 41, pp. 269–293, 6 2012.

[60] E. Pibiri, P. Holzmeister, B. Lalkens, G. P. Acuna, and P. Tinnefeld, "Single-molecule positioning in zeromode waveguides by dna origami nanoadapters," *Nano Letters*, vol. 14, pp. 3499–3503, 6 2014.

[61] B. Luan and M. A. Kuroda, "Electrophoretic transport of single-stranded dna through a two dimensional nanopore patterned on an in-plane heterostructure," *ACS nano*, vol. 14, no. 10, pp. 13 137–13 145, 2020.

[62] T. T. Tran, K. Bray, M. J. Ford, M. Toth, and I. Aharonovich, "Quantum emission from hexagonal boron nitride monolayers," *Nature Nanotechnology*, vol. 11, pp. 37–41, 1 2016.

[63] R. J. Koch, J. Katoch, S. Moser, D. Schwarz, R. K. Kawakami, A. Bostwick, E. Rotenberg, C. Jozwiak, and S. Ulstrup, "Electronic structure of exfoliated and epitaxial hexagonal boron nitride," *Physical Review Materials*, vol. 2, no. 7, p. 074006, 2018.

[64] N. Wang, G. Yang, H. Wang, C. Yan, R. Sun, and C.-P. Wong, "A universal method for large-yield and high-concentration exfoliation of two-dimensional hexagonal boron nitride nanosheets," *Materials Today*, vol. 27, pp. 33–42, 2019.

[65] W. Cai, N. Hong, X. Feng, W. Zeng, Y. Shi, Y. Zhang, B. Wang, and Y. Hu, "A facile strategy to simultaneously exfoliate and functionalize boron nitride nanosheets via lewis acid-base interaction," *Chemical Engineering Journal*, vol. 330, pp. 309–321, 2017.

[66] Y. Wang, Z. Yu, C. S. Smith, and S. Caneva, "Site-specific integration of hexagonal boron nitride quantum emitters on 2d dna origami nanopores," *Nano Letters*, vol. 24, pp. 8510–8517, 7 2024.

[67] D. H. Shin, S. H. Kim, K. Coshic, K. Watanabe, T. Taniguchi, G. J. Verbiest, S. Caneva, A. Aksimentiev, P. G. Steeneken, and C. Joo, "Diffusion of dna on atomically flat 2d material surfaces," *ACS Nano*, vol. 19, pp. 21 307–21 318, 6 2025.

[68] J. Sülzle, W. Yang, Y. Shimoda, N. Ronceray, E. Mayner, S. Manley, and A. Radenovic, "Label-free imaging of dna interactions with 2d materials," *ACS Photonics*, vol. 11, 2024.

[69] Y. Zhan, J. Yan, M. Wu, L. Guo, Z. Lin, B. Qiu, G. Chen, and K. yin Wong, "Boron nitride nanosheets as a platform for fluorescence sensing," *Talanta*, vol. 174, pp. 365–371, 11 2017.

[70] J. F. Berengut, W. R. Berg, F. J. Rizzuto, and L. K. Lee, "Passivating blunt-ended helices to control monodispersity and multi-subunit assembly of dna origami structures," *Small Structures*, vol. 5, 4 2024.

[71] J. L. T. Wah, C. David, S. Rudiuk, D. Baigl, and A. Estevez-Torres, "Observing and controlling the folding pathway of dna origami at the nanoscale," *ACS Nano*, vol. 10, pp. 1978–1987, 2 2016.

[72] Y. Kabiri, A. N. Ananth, J. van der Torre, A. Katan, J. Hong, S. Malladi, J. Kong, H. Zandbergen, and C. Dekker, "Distortion of dna origami on graphene imaged with advanced tem techniques," *Small*, vol. 13, 8 2017.

[73] F. N. Gür, F. W. Schwarz, J. Ye, S. Diez, and T. L. Schmidt, "Toward self-assembled plasmonic devices: High-yield arrangement of gold nanoparticles on dna origami templates," *ACS Nano*, vol. 10, 2016.

7 Supplementary information

7.1 Origami recipies

Component	Concentration bulk	Desired concentration	Volume
Scaffold	100 μM	10 nM	5 μL
Staples	100 μM	50 nM	4 μL
Mg^{2+}	100 mM	12,5 nM	6,25 μL
TAE	100 mM	10 nM	5 μL
Fluorescent probe	1 μM	50 nM	2.5 μL
Milli Q	M	M	27,25 μL

Table 3: Concentration and volumes assembly of DNA origami structures including docking staples.

Component	Concentration bulk	Desired concentration	Volume
Scaffold	100 μM	10 nM	5 μL
Main staples	100 μM	50 nM	4 μL
Edge staples	100 μM	50 nm	0.9 μL
Mg^{2+}	100 mM	12,5 nM	6,25 μL
TAE	100 mM	10 nM	5 μL
Fluorescent probe	1 μM	50 nM	2.5 μL
Milli Q	M	M	26,35 μL

Table 4: Concentration and volumes assembly of DNA origami structures including docking staples for array formation.

7.2 AFM images

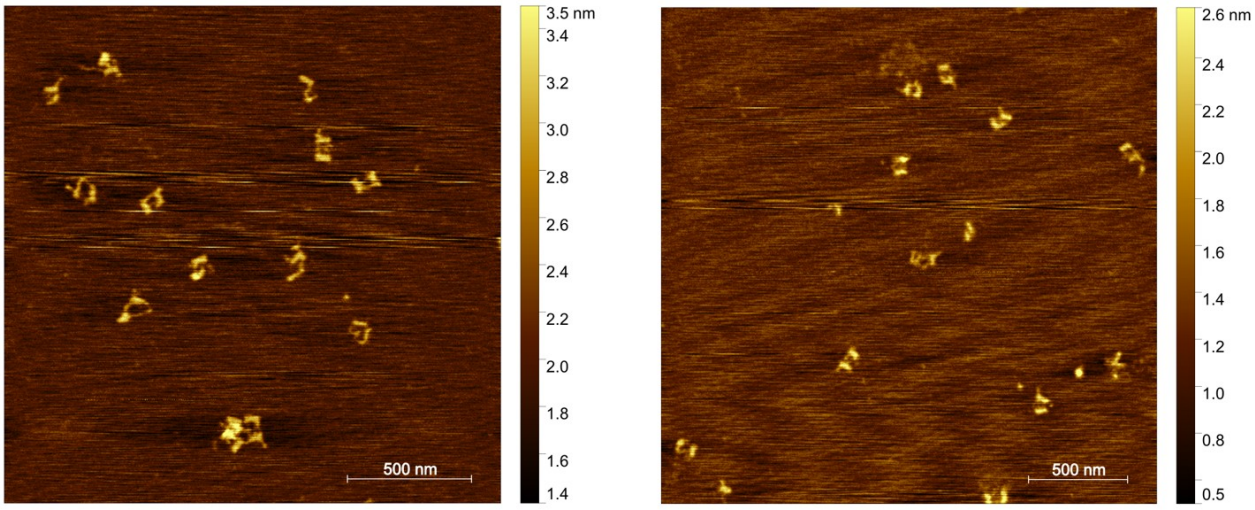

Figure 54: AFM images of single origami structures without 19 sticky ends extensions near nanopore.

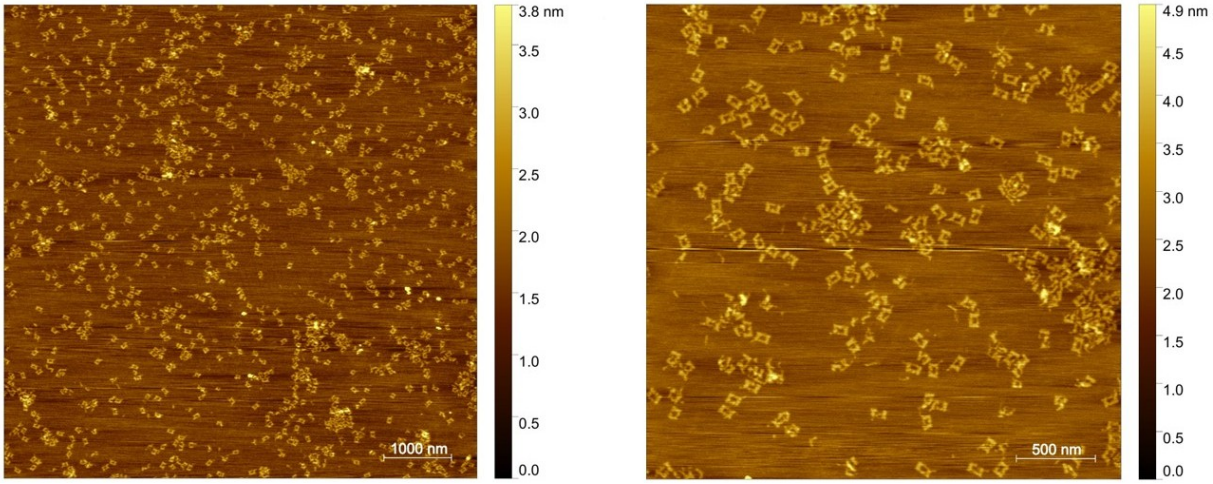

Figure 55: AFM images of origamis filtered with a 100Kda filter.

7.3 4 Staple visualization

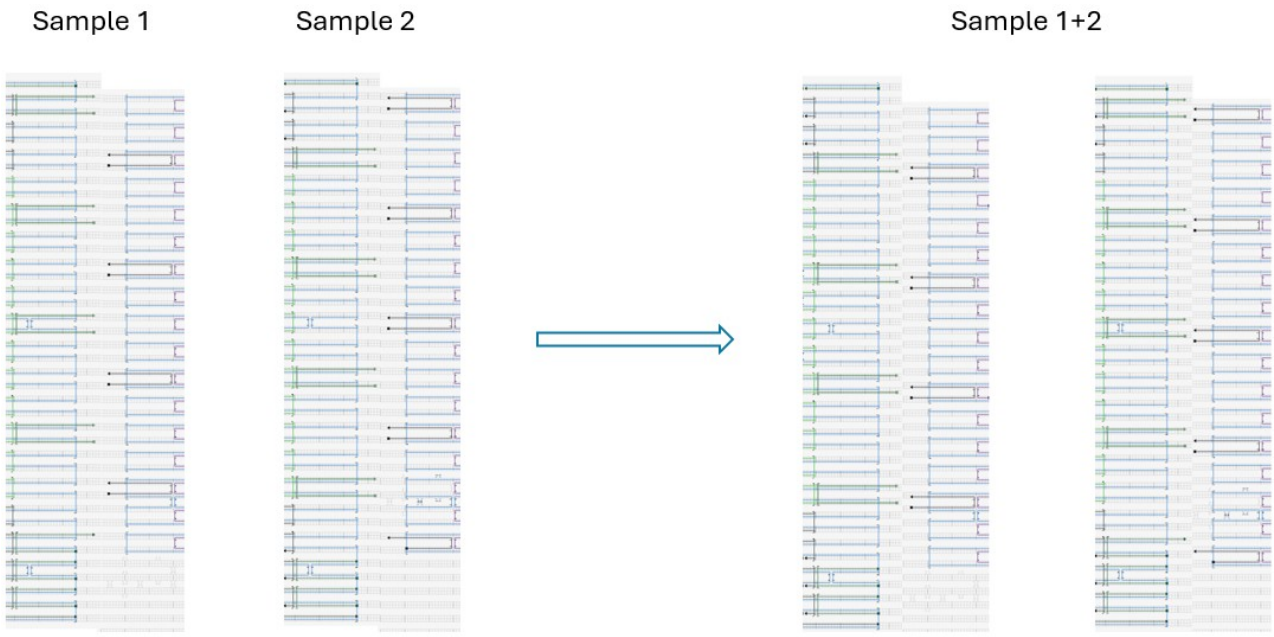

Figure 56: Schematic visualization of origami side interactions between different samples.

7.4 Roughness graphs

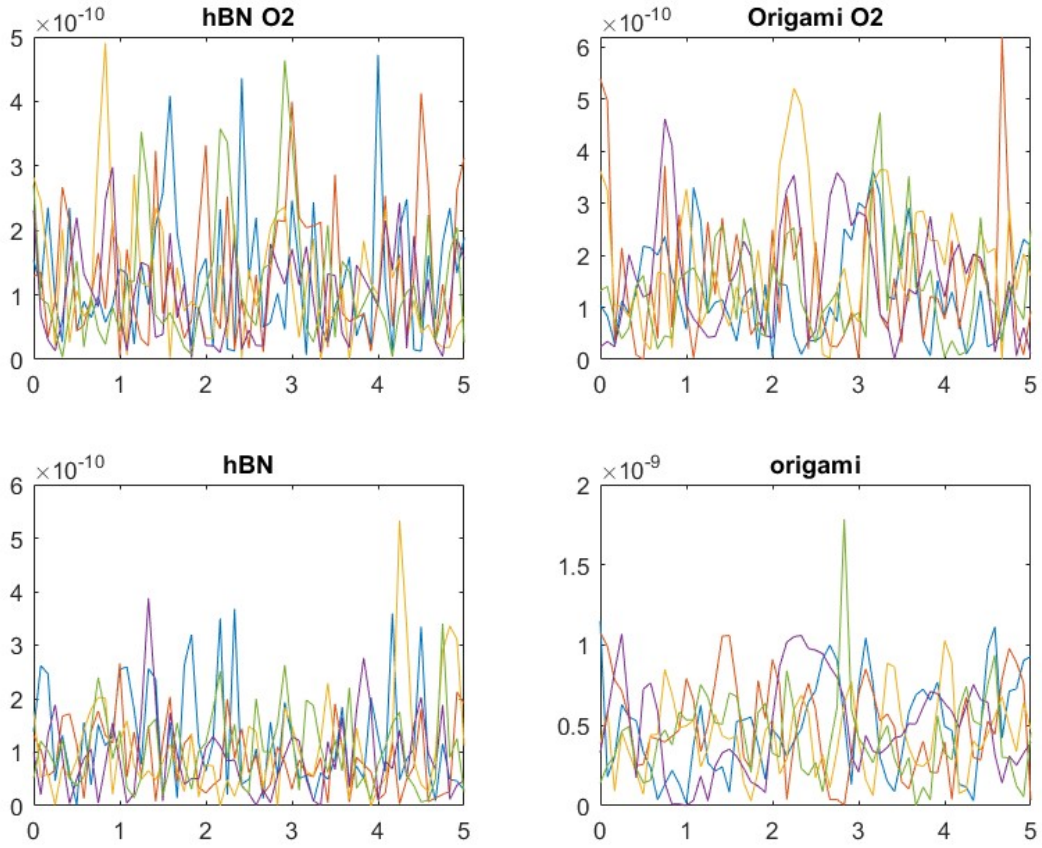

Figure 57: Roughness graphs of different samples.

7.5 Height analysis origamis

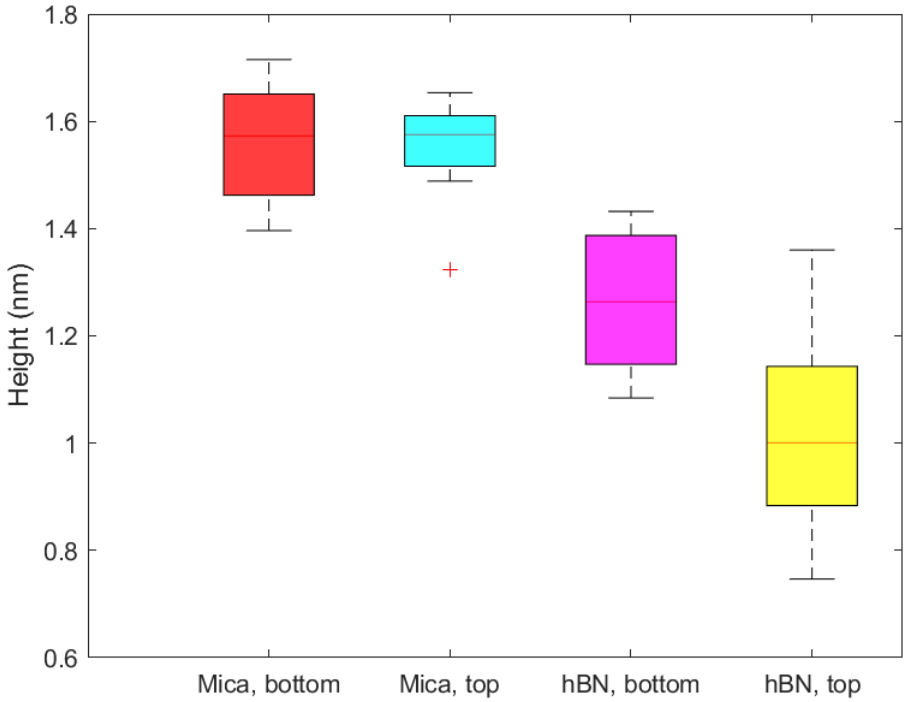

Figure 58: Height analysis origamis on mica and hBN, making a distinction between the orientation(top and bottom).

To gain more insight into the effect of the orientation of the origami structures on different surfaces, several measurements were done. The height of origamis with docking staples were analyzed on mica and hBN, while making a distinction between their orientation(top and bottom). This measurement maintains the hypothesis that the smaller and thicker origamis have their docking staples pointing towards the surface. Figure 58 shows the results. This indicates that the height does not vary when origamis are placed on mica, but does when positioned on hBN. The origamis with docking staples pointing towards the surface are on average 0.24 nm thicker than origamis oriented the other way. These results substantiate the different interaction mechanisms between origamis with and without docking staples.

7.6 Fluorescent images

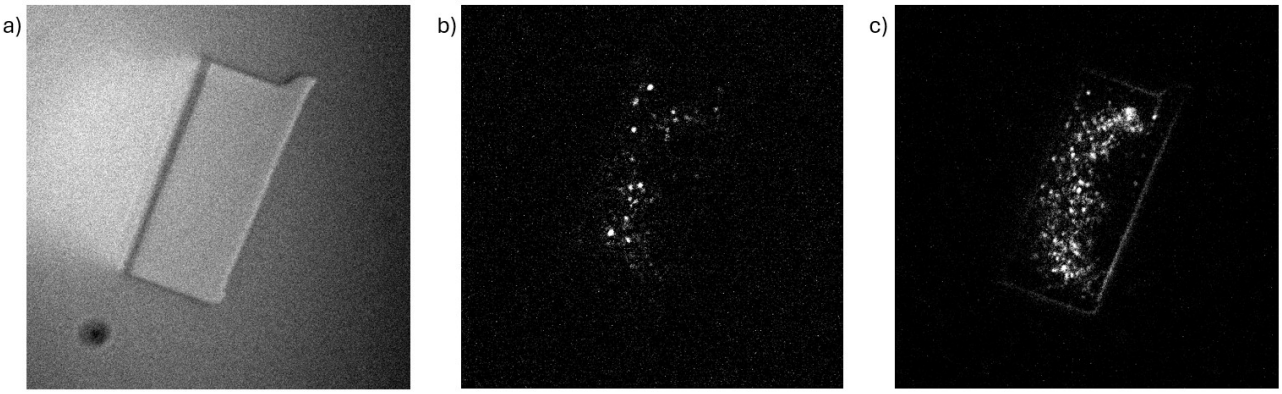

Figure 59: Fluorescent images. a) White light, b) Red, 25 mW laser power with 100 ms exposure time, c) Green, 125 mW laser power with 100 ms exposure time.

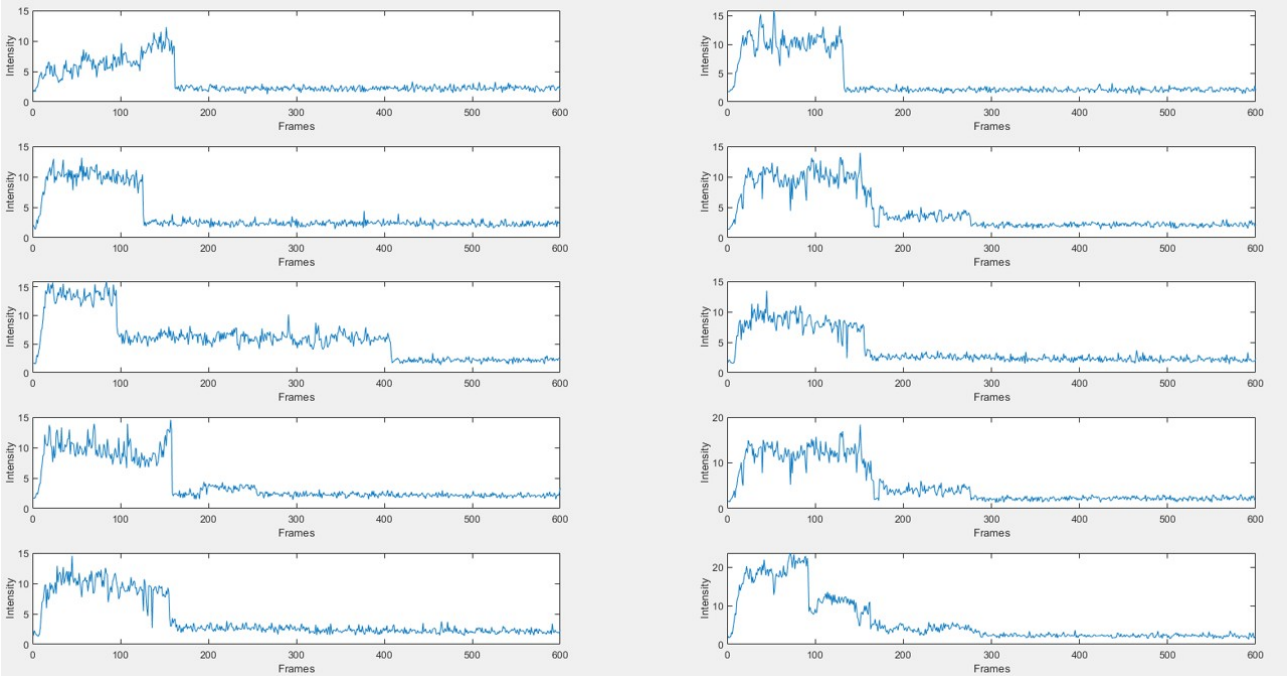

Figure 60: All intensity profiles as a function of time, ATTO647N sample.

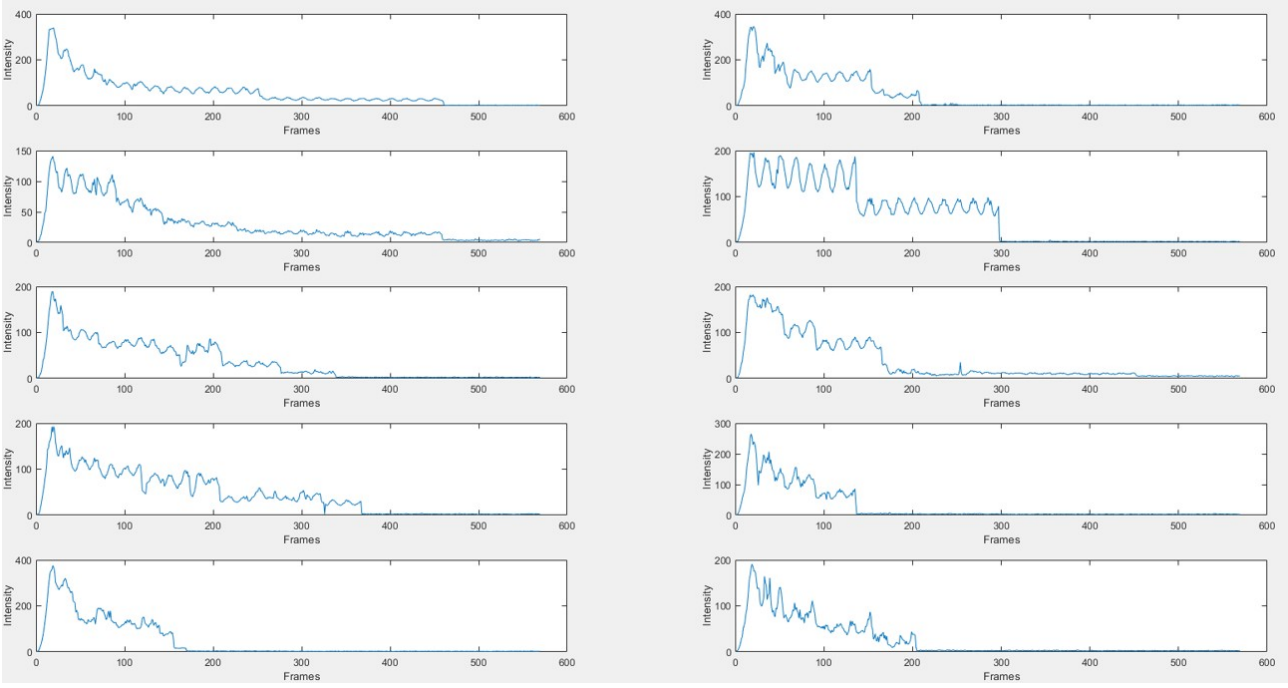

Figure 61: All intensity profiles as a function of time, array sample.

7.7 Staple codes

Code sequences left side:

1. CGAATGATGCGATTTTAAGAACCATTGTGAATTACCTTAAGGAA
2. GTTTGTAAACCAAAATAGCGAGTACCAGACGACGATAATCCCCC
3. AAAAGTAATCAAAAATCAGGTCAACGAGAATGACCATAAATTTG

4. AGAGCCGCGTTTTAATTCGAGCAAAGACTTCAAATATCAGGCGG
5. AGCTATCAGGATTAGAGAGTACGCAAACTCCAACAGGTATACTA
6. ATTAACCATTCCATATAACAGTCGGTGTCTGGAAGTTTGAATAC
7. GAGACGGGCAAAGAATTAGCAATAAATCATACAGGCAAGACGTT
8. GGGTTAACCCTGTAATACTTTTTACCAAAAACATTATGGGTGAG
9. GGCAGCTAATGCCGGAGAGGGTGTTCTAGCTGATAAATGCAGGA
10. GCGCATACAAGAGAATCGATGATGAGAGTCTGGAGCAATATGGC
11. TGTACAGGAACGCCATCAAAAACATTTTTTAACCAATATTAGAT
12. TCGGTGACAACCCGTCGGATTCTAAATGTGAGCGAGTACAGCTC
13. CACTGAGCACTCCAGCCAGCTTCGGCCTCAGGAAGATCCTGTAG
14. CTCACTGGTGCGGGCCTCTTCGGTTGGGAAGGGCGATCAAATCA
15. AAACAGCAGGGTTTTCCCAGTCTTAAGTTGGGTAACGCAAGTGC
16. AAGCCTACGGCCAGTGCCAAGCACGACGTTGTAAAACGAATCGA
17. CGGAAGCATAAAGTGTCACACAACATACGAGCAACATA

Code sequences right side:

1. CATTCG TAAAACGAAAGAGGCAAAAGACCGAACTGACCAACTTTGAAA TTCCTT
2. ACAAAC CGAGGTGAATTTCTTAAACAGGCCACTACGAAGGCACCAACC GGGGGA
3. ACTTTT CCACCCTCATTTTCAGGGATAATCGGTTTATCAGCTTGCTTT CAAATT
4. GGCTCT AAGCCAGAATGGAAAGCGCAGGAACCGCCACCCTCAGAGCCA CCGCCT
5. ATAGCT GCAAGCAAATCAGATATAGAACAAACAAATAAATCCTCATTA TTAGTAT
6. GTTAAT TCATTCCAAGAACGGGTATTAGAATCATTACCGCGCCCAATA GTATTC
7. CGTCTC TCCTAATTTACGAGCATGTAGATAATCGGCTGTCTTTCCTTA AACGTC
8. TAACCC GCGCCTGTTTATCAACAATAGAACAAGAAAAATAATATCCCA CTCACC
9. GCTGCC ACAATAAACAACATGTCAAAGCTGAATCAGCTAATGCAGAAC TCCTGC
10. ATGCGC TAAGAGAATATAAAGTACCGAAGTAATTCTGTCCAGACGACG GCCATA
11. TGTACAG AGGGCTTAATTGAGAATCGCCGAGGCATTTTCGAGCCAGTAA ATCTAA
12. CACCGA GGTCTGAGAGACTACCTTTTTATAAAGCCAACGCTCAACAGT GAGCTG
13. TCAGTG TTTACATCGGGAGAAACAATAAGTGAATTTATCAAAATCATA CTACAG
14. AGTGAG ATTAGAGCCGTCAATAGATAAGAATATACAGTAACAGTACCT TGATTT
15. CTGTTT ATTCACCAGTCACACGACCAGAGGAGCACTAACAACTAATAG GCACTT
16. AGGCTT TTAAAGGGATTTTAGACAGGAATGGATTATTTACATTGGCAG TCGATT
17. TATGGTTGCTTTGACGAGCACGGGAGCTAAACAGGAGGCCGA TATGTT

Code sequences mini side:

1. GCGCGGGGAGAGGCGGCGAGTAAAA
2. TTGCCCTTCACCGCCTGGCCC
3. TAAAAA TGAGAGAGTTGCAGCAAGCGGTCCACGCTGGT
4. GCCCGAGATAGGGTTGAGTGTTGTTCCAGTTT CCTGAA
5. GGAACAAGAGTCCACTAAGCGAAAGGAGCGGGAGAAAGGAAGG
6. TTTTTA TCCAACGTCAAAGGGCATTAAAGAACGTGGAC TTCAGG

Code sequences for fluorescence.

1. TATAGCCAATAAGTTTTAACGGGCGCCACCAGAACCACCTTTCATA
2. GCCGTTTTAGGGAAATCCCCACCAAGGCTATCAAAATCTTAGCGTTTGCCATCTGAAGC
CTTAAATCAAGACTTGCGGG
3. GCCGTTTTAGGGAAATCCCCACCAAGGCT AAGGCGTTACTCCTTATTACGCAG
4. TGATGAAACAACCTTGCTTCTGTAAAACTTTTTCAAATATATTGATAAAT

Code sequences hBN attachers:

1. GAGGACAGATGAACGGTGTACAGAC (30x A)
2. ACGCTGGCTGACCTTCATCAAGAGTAATCTTGACACCATGTTACT

3. CAGGCGCATAGGGTCAATCATAAGGGAAATAC (30x A)
4. AACATCTTTGACCCCCAGCGAACGAGGCGCAG (30x A)
5. ACTAAAACACTCGGGTAAAATACGTAATCTTG (30x A)
6. AAAGCGCCGACAATGACAAGAAGTTTCCATTA (30x A)
7. ATACCGATAGTTAGGAGCCTTTAATTGTGCAAGCCCAATAGGAAAGAAC
8. ACCCTCCCCATGTACCGTAACAAAAAAAAAGGCTCC (30x A)
9. TTCTTCTGAGAAGTGTTTTTAAATACCTACAT
10. ATCGTCTGAAACGGTACGCCAGAATCTCGTTAGAATCAGAGCGTAT (30x A)
11. CGATTCACCAGTGAGACGGCAGGGTGGTTT
12. AACGTGCTTTCCAAATCCTGTTTGATGGATCG (30x A)
13. GCAATAAATCAAAAGAATATTGCCCCAGCAGG (30x A)
14. GCAAAATCCCTTAGTGTAGCGGTCACGCGAGC (30x A)
15. TTTGCCGGCGAACGTGGCGCGCTAGGGCGCTG (30x A)
16. TTGACGGGGAAATTGGGGTCGAGGTGCCGTAAAGCACTAAATCGGAACC
17. GAAGAGAAAAACCGTCTATCAACCCAAATCAAGT (30x A)